Nonlinear Microwave Optomechanics

Shevchuk, Olga

DOI
10.4233/uuid:c4468f57-6f08-4262-9790-16ea981c8e68

Publication date
2017

Document Version
Final published version

Citation (APA)
Shevchuk, O. (2017). *Nonlinear Microwave Optomechanics*. [Dissertation (TU Delft), Delft University of Technology]. https://doi.org/10.4233/uuid:c4468f57-6f08-4262-9790-16ea981c8e68

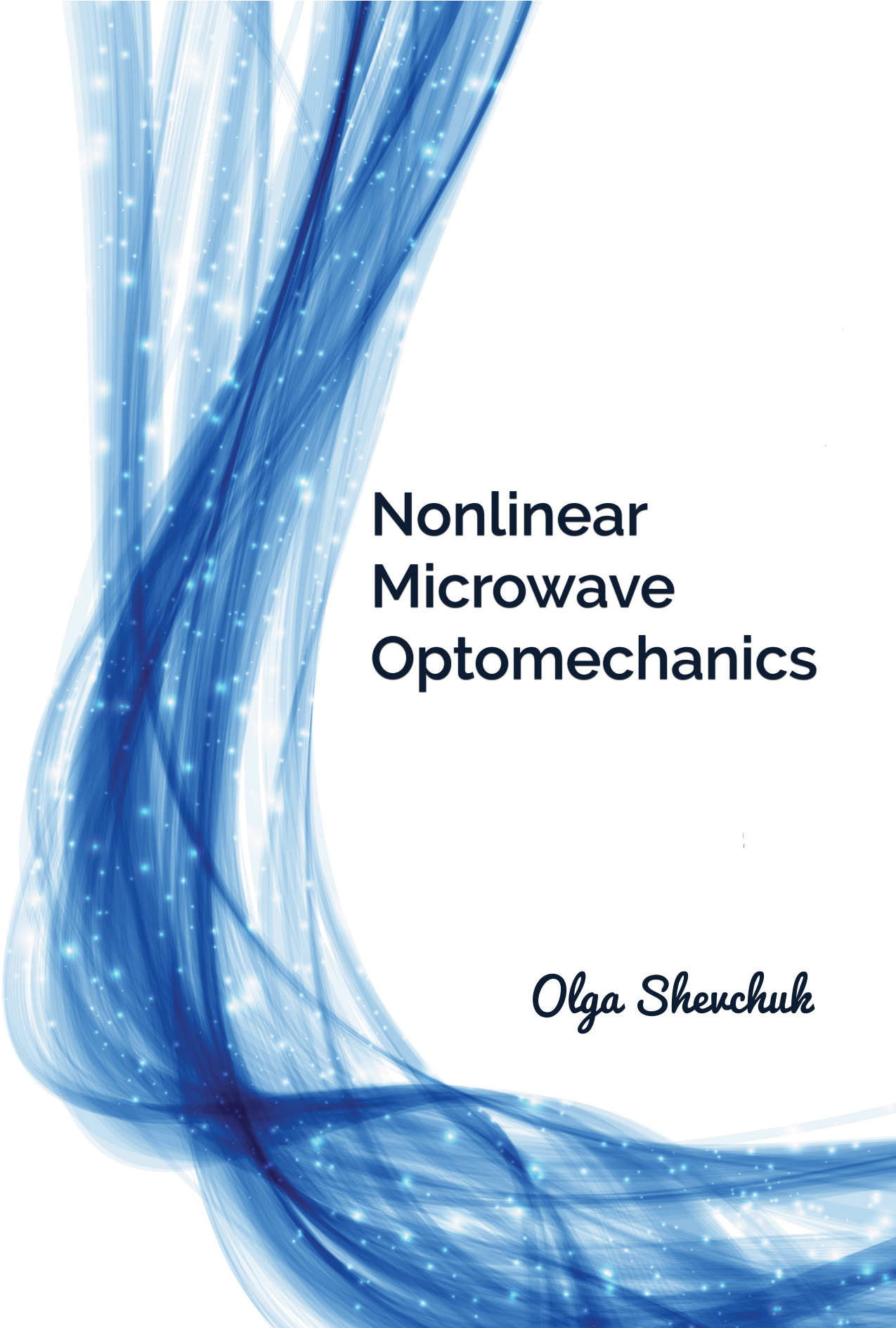

Nonlinear Microwave Optomechanics

Olga Shevchuk

NONLINEAR MICROWAVE OPTOMECHANICS

NONLINEAR MICROWAVE OPTOMECHANICS

Proefschrift

ter verkrijging van de graad van doctor
aan de Technische Universiteit Delft,
op gezag van de Rector Magnificus prof. ir. K. C. A. M. Luyben,
voorzitter van het College voor Promoties,
in het openbaar te verdedigen op maandag 6 maart 2017 om 10:00 uur

door

Olga SHEVCHUK

Master of Science in Theoretical Physics
van Universiteit van Amsterdam, Nederland,
geboren te Kiev, Oekraïne.

Dit proefschrift is goedgekeurd door de
promotor: Prof. dr. Ya. M. Blanter

Samenstelling promotiecommissie:

Rector Magnificus,	voorzitter
Prof. dr. Ya. M. Blanter,	Technische Universiteit Delft, promotor

Onafhankelijke leden:

Prof. dr. I. Wilson-Rae,	University of York
Dr. G. A. Steele,	Technische Universiteit Delft
Prof. dr. ir. T. H. Oosterkamp,	Universiteit Leiden
Prof. dr. ir. L. M. K. Vandersypen,	Technische Universiteit Delft
Prof. dr. Yu. V. Nazarov,	Technische Universiteit Delft
Prof. dr. ir. T. M. Klapwijk,	Technische Universiteit Delft

Printed by: Gildeprint

Front & Back: D. Chiu and O. Shevchuk, using and adapting "abstract waves" by Samarets, https://www.vectorstock.com/royalty-free-vector/abstract-waves-background-vector-8818330. Licence at https://www.vectorstock.com/faq/members/standard-license.

Casimir PhD Series, Delft-Leiden 2017-05

ISBN 978-90-8593-290-1

An electronic version of this dissertation is available at
http://repository.tudelft.nl/.

To those who were *there* during the times of morning glory and the times of night bloom water lily

PREFACE

The time flies and in the blink of an eye I am finishing my PhD with this thesis. These almost 4.5 years have been quite a journey in my life. Ready for the new start and looking back I am grateful that I got an opportunity to do my PhD in Delft. I could not thank enough my supervisor Yaroslav, my friends, my grandmother, my husband and his family for always being there.

I should mention the person from whom I got the passion for Physics. I still remember it was time before Christmas in 2002 when my Physics teacher Vladimir Bezruchko asked me whether I would like to participate in the Physics Olympiad. He spend his time during winter break to prepare me for it. Later I continued on the same path during my Bachelor in Taiwan with Dr. Chung-Hou Chung. That's where I learned that the theoretical results can be implemented in the experiment and further in industry in nearby Science Park. Then, during my Master in Amsterdam I was fortunate to do something more theoretical and abstract project with Prof. dr. Jean-Sébastien Caux.

The previous experience made me realize that during a doctorate I would like to do something more applied and analytic. I send out couple of e-mails asking for the PhD position and one of them was to Delft to Mrs. Miriam Blaauboer. She replied that, unfortunately, she did not have anything for the moment, but Prof. Yaroslav Blanter has an open position. After that I have received an invitation to the interview and presented my work. I was extremely nervous that time. I was looking at the faces to get a clue whether it was clear. After the talk I had a chance to speak to Ciprian and he was very encouraging. So finally, albeit my worries in October I have started to work on my first PhD project.

During my interview Yaroslav has stated clear that he expect a PhD student to be an independent researcher and have 4 papers by the end of the PhD. I am very thankful that from very beginning I had a lot of flexibility but you still helped me to keep up with time schedule and not only in the scientific perspective but also in the moral support and calm approach. In some sense, I've acquired a second father. Your diplomatic way of speaking made me think over without being discouraged. I always appreciate your light push toward the collaboration with other people and have learned the power of it. You taught me that we can look at complicated things in much simpler and general way. Sometimes I am so focused on the specific problem that I forget to build bridges and I will try to improve this aspect of my personality.

When I entered the theory group I felt very welcomed. Many people were at the last stage of their PhD. Their experience and wisdom helped me a lot later on. That time we had 5 girls in the group including me. I was in the room together with Fatemeh M., she has a very kind and soft personality. Every day we chat about our life and research, which made the atmosphere in the office very comfortable. Fateme J. was always passing my room and stop by with the smile, which also made me smile. She has a very strong personal opinion and a positive view on life. I am always enjoying our coffee time. From her I am happy to meet Andy. Alina has more artistic personality despite our scientific

environment. The long discussions about the vegans (the first time I've heard this word during the coffee break in Delft), the pollution and wearing leather were raised by Mireia. Of course, the girls diluted mostly male group. I had couple of research talks with Ciprian and his view on living life was always surprising and at the same time interesting. If I needed any advise Marcin was always available to provide it. I admire his perfectionism, home parties and realistic as well as handy approach. He often brought a cake for the coffee break without any reason. That's how I met Cecile offline through her amazing cooking skills. Talking with Yanting always remind me of the warm time in Taiwan and my fun bachelor time. While not knowing Marnix that long he is very friendly and never declined to help with moving. Akash organized very nice parties and is a great dancer with enormous energy. Always relax Paul even though seldom being in Delft finds time for the coffee breaks. I would always remember your amazing ideas such as making your own coating of the pan and an one house for the friends' families in order to still have social life. We had a lot of fun teaching Statistical Physics together with energetic and talkative Orkide. To Chris V., Chris D., Gio, Yunshan, Frans, and Rodrigo, thank you for having occasional talks. Every time I meet Chris V. in the train or outside in den Haag is such a happy coincidence. I know Maryna since our high school time, you know what you want to do with realistic and straightforward thinking. It was fun to meet again and spend time during your Master.

After many girls graduated, Erika was always there to deal with any administrative issue and for more girly chats. She somehow manages to get things done in a short time and I am very grateful for her moral support. Yuli always asks peculiar questions during the group talks, but actually always to the point, and has great coffee break jokes. Miriam was always very kind and enthusiastic during my evaluation meetings with a lot of positive energy. Jos is a very good teacher and it was a pleasure to be his teacher assistant. Michael and Anton are great addition to the existing faculty members and the group has been grown quite much thanks to them.

To Adriaan for such a great help with my Ducth translations. Tomo was my officemate for two years, with whom we shared the great cakes, very warm discussions about marriage and research, day trips, and tasty Japanese food. João has joined Yaroslav's team and since then we have amazing coffee breaks and chats about our progress, research and personal life. He is always digging to the end and drawing very interesting characters. To Vincent for his open personality, cute French accent and sharing small breaks with me. I was not that social with the new group after the birth of my son and a new pregnancy, but I always enjoy the group coffee breaks and some lunches with Jose, Albert, Sebastian, Rafael, Bas, Xiaoli, Evgeny, Vigdis, and Sanchar. To Doru and Michal thanks for always asking me how am I doing and have a small talks.

During my PhD I had a great pleasure to join weekly Gary's group meetings. I learned a lot about experimental implementations and about looking at the problem from the experimental point of view. While working on the project with Vibhor we had some great scientific discussions. Although it was hard to convince you at times, I am happy about our final result and learned a lot in the process. With Minyun we had similar "happy situation" and could share our experiences and support. To Shun for our discussions about the SQUID. To Daniel, Sal, and Martijn for our short talks either during the conference or simply in the corridor.

I also would like to thank Saro for an amazing hosting during one month I was in Pisa. You asked me great questions and gave me important scientific input for my projects. For making my stay fun and spending some evenings with me, I thank Antonella and Davide. Simone, Stefano, Matteo, and Francesco, thank you for teaching me Italian and great lunch and dinner discussions.

Special thanks to Nastya. You have always supported me, understood and spent the time in the university and outside of the work environment. To all my friends who are outside of the work circle. To Yulya, you and Sasha with Margarita are such a fun people to hang around. To Misha, you have always tried to understand what I am doing and to Gloria, who is optimistic and so relax. To Dima and Emily, for great evenings out. To Kathy, who is so far away but always checking with me. To Yulya, who lives in Ukraine, I am always grateful for all the help and full support you provide. To Pasha for sharing the same fate but being always positive about it and supportive. To Vincent despite knowing you so short, but living close by and have history of being in Taiwan, you are close to me by default.

To Dave, for your patience, support and all the happy moments we had together. To the Chiu family, for treating me as a family member, having amazing trips, supporting and helping us with our son despite living so far. And to my grandmother, thank you that you are always thinking about me, your support and kind heart.

Olga Shevchuk
February 2017

CONTENTS

Preface **vii**

1 Introduction **1**
1.1 Optomechanics . . . 2
1.1.1 Basic Theory . . . 3
1.2 Superconducting microwave cavity . . . 4
1.3 Josephson effect . . . 6
1.3.1 dc SQUID . . . 9
1.4 Optomechanically induced transparency . . . 10
1.5 Outline of this thesis . . . 14
References . . . 14

2 Multistability of a Josephson parametric amplifier **17**
2.1 Introduction . . . 18
2.2 The Model . . . 19
2.3 Equations of motion . . . 21
2.4 Backaction . . . 25
2.5 Conclusions . . . 27
References . . . 28

3 Flux-mediated optomechanics **31**
3.1 Introduction . . . 32
3.2 Current of the asymmetric SQUID . . . 33
3.3 Quantization . . . 35
3.3.1 Dispersive regime . . . 35
3.3.2 Resonant frequencies . . . 39
3.4 Discussion . . . 42
3.5 Conclusions . . . 43
References . . . 44

4 Quantum analysis of the nonlinear cavity with a mechanical resonator **47**
4.1 Self-consistent harmonic approximation . . . 48
4.2 Kerr nonlinearity . . . 48
4.3 Dissipationless action . . . 49
4.4 Action with dissipation . . . 51
References . . . 55

5 Optomechanical response of a nonlinear mechanical resonator **57**
5.1 Introduction . . . 58
5.2 Model of a driven nonlinear cavity . . . 59
5.2.1 Red sideband . . . 62
5.2.2 Blue sideband . . . 63
5.2.3 Reflection coefficient . . . 63
5.3 OMIA detuning . . . 65
5.4 Nonlinear response map . . . 67
5.5 Beyond Duffing . . . 68
5.6 Conclusions . . . 69
References . . . 70

6 Negative nonlinear damping in the graphene resonator **73**
6.1 Introduction . . . 74
6.2 Device . . . 74
6.3 Experiment vs theory . . . 75
6.3.1 Extra instabilities . . . 77
6.3.2 Fifth order nonlinearity . . . 78
6.4 Conclusions . . . 79
References . . . 79

Summary **83**

Samenvatting **85**

Curriculum Vitæ **87**

List of Publications **89**

1

INTRODUCTION

1

1.1. OPTOMECHANICS

In my childhood I liked to play with light. By catching a light in the mirror and observing a light spot moving around on the wall I didn't realize that the reflection of light gives rise to the momentum transfer referred to as radiation pressure force. This force is used extensively in the current technology and studied carefully by many scientists. At first the concept of the radiation pressure of light was predicted by Kepler and then in 1901 experimentally observed [1, 2]. In the 1970s it was Ashkin [3], who first demonstrated that dielectric particles can be accelerated and trapped using radiation pressure force from the focused laser beams. Then two groups [4, 5] of Hänsch and Schawlow as well as Wineland and Dehmelt showed that the resonant light scattering provided essential enhancement for the laser cooling of neutral atoms and ions, which also led to many advances such as atomic Bose-Einstein condensates.

The nature of the radiation pressure force guided a development of the cavity optomechanical systems, where an optical or microwave cavity contains a movable element. An example of such system, known as an Fabry-Perot interferometer, is an optical cavity with two mirrors and one of the end mirror oscillating just as it is attached to the spring. This concept was used in the early gravitational wave antennas in the 1960s, but mostly in the 1970s and 1980s. Braginsky analyzed an effect of the radiation pressure on the suspended end mirror of the cavity, which either absorbs or reflects radiation and results in the either damping or antidamping of mechanical motion. He demonstrated it in the first experiments using a microwave cavity[6, 7]. In the optical regime, the first observation was in 1983 of the radiation pressure induced optical bistability in the transmission of Fabry-Perot interferometer [8]. Braginsky, Cave and others further analyzed the consequences of the quantum fluctuations of radiation pressure and establish the standard quantum limit for mechanical detection, which is crucial for the gravitational wave detectors such as in Laser Interferometer Gravitational-Wave Observatory (LIGO).

While many concepts of optomechanics can be traced back to the study of gravitational wave detectors, the idea of measurement and manipulation of the macroscopic object at quantum limit motivated researchers from different fields of solid-state physics, quantum information and computation to exploit the possibility of studying quantum behavior of mechanical objects in their in comparison small labs. The availability of the micromechanical and nanomechanical devices capable of probing extremely tiny forces at the atomic scale and detailed understanding of the mechanical effects of light made realization of macroscopic mechanical systems in the quantum regime achievable with no significant thermal effects [9–13]. Coupling optical or microwave cavities with mechanical resonators enables control of mechanical motion or mechanical control of optical or microwave fields. Optomechanical systems hold promise in the creating nonclassical states of light and mechanical motion. All these provides the basis for the applications in the quantum information processing, building hybrid quantum devices and testing fundamentals of quantum mechanics. On another hand, optomechanical systems provide highly sensitive detection of tiny forces, displacements and masses.

Starting from the 1990s there has been theoretical studies of the quantum optomechanical systems. The first steps in the direction of quantum optomechanics were the quantum nondemolition measurement and squeezing of light. The experimental realizations of simple optomechanical systems followed showing optical feedback cooling,

optical spring effect, self-induced oscillations, and so on. Then, different optomechanical systems were proposed in order to achieve non-dissipative radiation pressure force. Experiments with optical cavity involved membranes, suspended micromirrors, microtoroids, photonic crystals and many others[14].

Optomechanics can be also demonstrated with microwave radiation rather than visible light. Experiments with microwave cavity had its own independent development and based on the measuring and controling mechanical resonator using electrical or other nonoptical way. These include a superconducting transmission line with embedded nanomechanical beam, a drum resonator which is integrated into the superconducting resonant circuit or coupling mechanical resonator to a superconducting flux qubit [15–17]. The idea behind them is to couple mechanical resonator capacitively to the microwave cavity. Such devices have a great chance to be sensitive detectors and possibly in realizing quantum hybrid systems by direct interaction with two-level systems. This thesis mostly focuses on the latter branch of the optomechanics involving microwave cavity.

1.1.1. BASIC THEORY

To describe the basic theory behind cavity optomechanics we again refer to the simple driven Fabry-Perot cavity. Earlier, we described the effect of the radiation pressure on the suspended mirror. However, the displacement of this mechanical resonator is also changing the cavity length and, therefore, shifting the cavity resonance frequency ω_c:

$$\omega_c(x) = \omega_c + x\frac{\partial\omega_c(x)}{\partial x}|_{x=0} + \dots \tag{1.1}$$

The cavity frequency shift per displacement $G = \partial\omega_c(x)/\partial x|_{x=0}$ is often referred as optomechanical coupling constant. Here we consider out of many cavity modes only the one, which is closest to the drive frequency. Furthermore, we consider one mechanical mode with mechanical frequency ω_m. Then the uncoupled Hamiltonian of the cavity and mechanical modes is given by two quantum harmonic oscillators with annihilation ($\hat{a}$, $\hat{b}$) and creation ($\hat{a}^\dagger$, $\hat{b}^\dagger$) operators, which is usually a good approximation to the experimental results. The mechanical resonator is quantized using position operator $\hat{x} = x_{\mathrm{XPF}}(\hat{b} + \hat{b}^\dagger)$ with zero-point fluctuations of the mechanical resonator $x_{\mathrm{XPF}} = \sqrt{\hbar/2m\omega_m}$ and effective mass of the mechanical resonator m. This results in the following uncoupled Hamiltonian

$$\hat{H}_0 = \hbar\omega_c\hat{a}^\dagger\hat{a} + \hbar\omega_m\hat{b}^\dagger\hat{b}. \tag{1.2}$$

In order to obtain the Hamiltonian of the optomechanical interaction we should take into account the cavity dependence on the displacement

$$\hbar\omega_c(x)\hat{a}^\dagger\hat{a} = \hbar(\omega_c + G\hat{x})\hat{a}^\dagger\hat{a} \Rightarrow \hat{H}_{int} = \hbar g_0\hat{a}^\dagger\hat{a}(\hat{b} + \hat{b}^\dagger) \tag{1.3}$$

with the single-photon optomechanical coupling strength $g_0 = Gx_{\mathrm{XPF}}$, which has the dimension of the frequency. By taking a derivative with respect to the displacement of the interaction Hamiltonian we can find the expression for the radiation pressure force

$$\hat{F} = -\hbar G\hat{a}^\dagger\hat{a}. \tag{1.4}$$

If driving is added to the system then we include also driving Hamiltonian

$$\hat{H}_d = \hbar\varepsilon(\hat{a}^\dagger e^{-i\omega_d t} + \hat{a}e^{+i\omega_d t}) \tag{1.5}$$

with driving frequency ω_d and strength ε. Then, full Hamiltonian becomes time-dependent. To suppress time dependence we can apply unitary transformation $\hat{U} = e^{i\omega_d \hat{a}^\dagger \hat{a} t}$ and switch to the rotating frame of the drive frequency

$$\bar{H} = \hat{U}(H_0 + H_{int} + H_d)\hat{U}^\dagger - i\hbar\hat{U}\frac{\partial \hat{U}^\dagger}{\partial t} = -\hbar\Delta\hat{a}^\dagger\hat{a} + \hbar\omega_m\hat{b}^\dagger\hat{b} + \hbar g_0\hat{a}^\dagger\hat{a}(\hat{b} + \hat{b}^\dagger) + \hbar\varepsilon(\hat{a}^\dagger + \hat{a}). \tag{1.6}$$

where $\Delta = \omega_d - \omega_c$ is the drive detuning with respect to the cavity mode.

We did not include into the Hamiltonian the effects of the cavity decay, mechanical damping and fluctuations. The dissipation can only be included via adding the bath Hamiltonian and coupling to the bath, which is very well studied. Although, one can take a shortcut by including dissipation directly to the equations of motion and input-output theory [18]. We use this formalism to describe the phenomenon of the optomechanically induced transparency later in this chapter.

Hamiltonian that has been derived so far has nonlinear interaction due to the radiation pressure and in order to simplify it Hamiltonian is often linearized. In many recent experiments the number of photons in the cavity is large and this technique can be performed. Then, we can split cavity field into an average coherent cavity amplitude $\bar{a}$ and fluctuating part $\delta\hat{a}$ ($\hat{a} = \bar{a} + \delta\hat{a}$). Then the interaction Hamiltonian is given by

$$\hat{H}_{int} = \hbar g_0\bar{a}^2(\hat{b} + \hat{b}^\dagger) + \hbar g_0\bar{a}(\delta\hat{a}^\dagger + \delta\hat{a})(\hat{b} + \hat{b}^\dagger). \tag{1.7}$$

Here we disregarded the term $\hbar g_0\delta\hat{a}^\dagger\delta\hat{a}(\hat{b} + \hat{b}^\dagger)$ because this term is much smaller than the first term. However, the first term identifies the presence of average radiation pressure force $\bar{F} = \hbar G\bar{a}^2$ and can be omitted after shifting the average displacement origin $\bar{x}$ by $\delta\bar{x} = \bar{F}/m\omega_m^2$, which in turn shifts the detuning $\overline{\Delta} = \Delta + G\delta\bar{x}$. Also we assume $\bar{a}$ to be real and positive from what follows that $\bar{a} = \sqrt{n_d}$, where n_d is the number of drive photons inside the cavity. Thus, leaving the interaction Hamiltonian with linear interaction between cavity and mechanical modes and the coupling strength $g = g_0\bar{a}$ being many-photons optomechanical coupling strength.

However, to observe nonlinear quantum effects it is highly desirable to have strong coupling regime when g_0 exceeds cavity decay rate or even ultrastrong regime when g_0 also exceeds mechanical frequency. In this case, one cannot linearize Hamiltonian and has to solve the nonlinear problem.

1.2. SUPERCONDUCTING MICROWAVE CAVITY

A superconducting microwave cavity coupled mechanically resonator is described by the same optomechanical Hamiltonian as a Fabry-Perot cavity with an oscillating mirror. When we talk about microwave cavity we mean a resonant electric circuit. It is not literally cavity and the term "cavity" is used to strengthen the connection to the cavity optomechanics and resolve confusion with the words resonator or oscillator, since those can be used referring to both electrical and mechanical degrees of freedom. Whereas cavity is known to be referred to the electrical degree of freedom.

The idea of using superconducting circuits in optomechanics came about when experiments demonstrated the quantum nature of microwave light [19]. They achieved the coherent coupling between a qubit and a single microwave photon suggesting that it could be possible to couple a microwave cavity and a mechanical resonator. Even earlier there has been theoretical proposals for the quantum nanomechanical systems based on superconducting circuits [20]. The property of the superconductivity is that metal below a certain critical temperature T_c behaves as a perfect conductor without dissipation when an electric current passes through the metal. Meaning the experiments with superconducting circuits require cryogenic temperatures and for GHz cavity frequencies, the temperatures below 1 K are sufficient. Moreover, low temperature provides an advantage over optical cavity by eliminating difficulties with aligning and stabilizing. The microwave cavity is quite stable and rigid except for the involved mechanical resonator itself. There is also a draw back in comparison with optical cavity in terms of the lower frequency and as a consequence lower momentum transfer of the photons. Nevertheless, the single-photon optomechanical coupling strength can be of the order or even larger than in the optical setups.

Another challenge is photon detectors, which are essentially used in optical schemes but are not available in microwave optics. Indeed, whereas the detection of light is quantum limited, microwave amplifies are not shot-noise limited and add noise to the system. This problem is tackled by either using a nearly shot-noise-limited microwave interferometer or using the backaction-evading techniques [17, 21]. All advances of technology made it possible to probe a superconducting qubit with a mechanical resonator and to prepare a mechanical resonator coupled to a qubit in the quantum ground state with phonon occupation number less than one [16, 22].

The working mechanism of microwave cavity optomechanical systems based on the use of transmission line or lumped element circuit with an inductance and capacitance per unit length where radiation propagates. Then, in most cases the microwave cavity can be modeled as parallel LC circuit. The displacement of the mechanical resonator couples to the cavity capacitance C, see Fig.1.1, and shifts the cavity frequency defining optomechanical coupling constant $G = \partial\omega_c(x)/\partial x \propto \partial C(x)/\partial x$, which can be extracted from transmission or reflectivity measurement. This results in the nonlinear interaction Hamiltonian proportional to $a^\dagger a\hat{x}$ as discussed in previous section and often referred as the radiation pressure interaction. To be precise this is not always actual "pressure" in the textbook sense as a force per unit area and such interaction without linearization is rather dispersive optomechanical interaction in general sense. However, since it has the same origin in this thesis we refer to the interactions of the form $a^\dagger a\hat{x}$ as the radiation pressure interactions, which can be linearized to the beam-splitter interaction. For example, the mechanical resonator can be coupled via dielectric gradient forces to the microwave cavity or inductively coupled as shown in Chapter 3 of this thesis. In addition the mechanical resonators can be coupled to the non-superconducting microwave cavities. Sideband cooling from room temperature to 100 K has been shown for non-superconducting cavities, which usually have low quality factors [23].

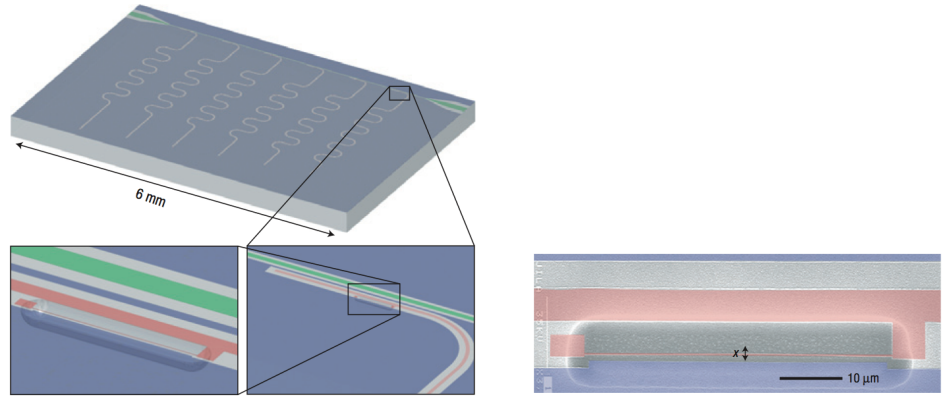

(a) (b)

Figure 1.1: (a) Chip with 6 stripline resonators (pink) and the straight feedline (green).The bottom panels are zooms into a capacitive elbow coupler and a mechanical resonator. (b) Scanning electron microscope image of an embedded mechanical resonator with displacement x.(Fig. from Ref. [15])

1.3. JOSEPHSON EFFECT

We start from describing theory of superconductivity, which leads to the Josephson effect. The concept of a superconductivity as a quantum phenomenon on a macroscopic scale was first proposed by London [24] and the microscopic theory of superconductivity was derived by Bardeen, Cooper and Schrieffer [25]. They showed that some of the free electrons become paired together. These electrons attraction producing this pairs, so-called Cooper pairs, arises from electron-phonon interaction, which should be larger than the Coulomb repulsion between electrons making metal superconducting. In order for pairs to benefit most from the attractive interaction, all of the phases of pairs must be the same. Thus, if the phase is fixed at any point of the superconductor, the relative phase of all other points adjust accordingly. This phase coherence is responsible for the dissipationless current flow and flux quantization, which shows that the flux contained in a closed superconducting loop is quantized in units of the flux quantum $\Phi_0 = h/2e$ (h is Planck's constant and e is the electronic charge). The superconducting state with paired electrons is lower in energy and, hence, more favourable than the normal state of the metal. Then the pairs are in condensate state which may be described by the macroscopic wave function introduced by Ginzburg and Landau [26] before BCS theory

$$\Psi(x,t) = \sqrt{\rho(x,t)}e^{i\chi(x,t)}, \tag{1.8}$$

which is a complex-valued order parameter in the superconducting phase. The density of pairs in the superconductor is given by $\rho(x,t) = |\Psi(x,t)|^2$. In the absence of applied fields or currents, the phase $\chi(x,t)$ takes the same value throughout the superconductor.

In 1962 Josephson made a prediction that a supercurrent should flow between two superconducting electrodes separated by a thin insulating barrier even in the absence of voltage [27]. If there are two superconductors isolated from each other, the phase of each superconductor can change independently. As long as superconductors are moved close

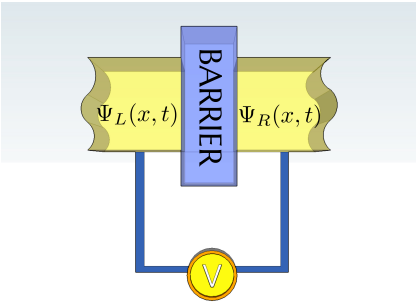

Figure 1.2: A schematic diagram of the Josephson junction connected to the voltage V. The wavefunction of the left electrode is Ψ_L and of the right Ψ_R and the phase difference across the junction is $\Delta\phi = \chi_R - \chi_L$.

together and separated by "weak link" it is often interpreted as coherence of electrons at two sides of the barrier. A weak link can be an insulating layer, as Josephson originally proposed, or a normal metal layer made weakly superconducting by a proximity effect, or a constriction in almost continuous superconducting material. These three cases of Josephson junction are often referred as $S-I-S$, $S-N-S$, or $S-c-S$ junctions, where the S, I, N, and c denote superconductor, insulator, normal metal, and constriction, respectively [28]. Eventhough there is a weak link the phase correlation occurs between two superconductors then the whole system behaves to some extent as a single superconductor.

To describe theory of the Josephson effect, we follow very simple derivation of Feynman [29], which is based on a two-level system picture. We consider a tunneling structure superconductor-barrier-superconductor as Fig. 1.2 shows. The pair wave function Ψ_L (Ψ_R) for the right (left) superconducting electrode is defined in eq.(1.8). If we consider a d.c. potential difference V across the junction and a zero voltage in the halfway of the barrier then the time evolution of the system is described by the Schrödinger equation for each electrode:

$$\begin{aligned} i\hbar\frac{\partial\Psi_L}{\partial t} &= eV\Psi_L + K\Psi_R, \\ i\hbar\frac{\partial\Psi_R}{\partial t} &= -eV\Psi_R + K\Psi_L, \end{aligned} \tag{1.9}$$

where K is the coupling amplitude, which gives a measure of the coupling interaction between the two superconductors and depends on specific junction structure. Next, we separate real and imaginary parts and get equations for the phase difference $\Delta\phi = \chi_R - \chi_L$ and the density of the left and right superconductor

$$\frac{\partial\rho_L}{\partial t} = \frac{2}{\hbar}K\sqrt{\rho_R\rho_L}\sin\Delta\phi, \tag{1.10}$$

$$\frac{\partial\rho_R}{\partial t} = -\frac{2}{\hbar}K\sqrt{\rho_R\rho_L}\sin\Delta\phi, \tag{1.11}$$

$$\frac{\partial\Delta\phi}{\partial t} = \frac{2eV}{\hbar}. \tag{1.12}$$

The current density is defined as $J \equiv \frac{\partial \rho_L}{\partial t} = -\frac{\partial \rho_R}{\partial t}$ and from eq.(1.10) and (1.11) it follows

$$J = \frac{2K}{\hbar}\sqrt{\rho_R \rho_L}\sin\Delta\phi. \tag{1.13}$$

This also can be written in terms of supercurrent between two superconducting electrodes and is known as the *first Josephson relation*

$$I = I_c \sin\Delta\phi \tag{1.14}$$

with the critical current I_c, which is the maximum supercurrent that the junction can support. The *second Josephson relation* described by eq.(1.12) says that if a voltage difference were maintained across the junction the phase difference would evolve accordingly.

Gauge-invariant phase

For simplicity we derived Josephson relation in term of the phase difference, which can be used at zero magnetic field. Generally, $\Delta\phi$ is not gauge-invariant quantity and, thus, cannot describe current I at a finite magnetic field. This can be resolved by replacing $\Delta\phi$ with gauge-invariant phase difference ϕ defined as

$$\phi \equiv \Delta\phi - \frac{2\pi}{\Phi_0}\int \mathbf{A}\cdot d\mathbf{s}, \tag{1.15}$$

where the integration is from the left electrode of the weak link to the right one and $\mathbf{A}$ is a vector potential.

RCSJ model

For the practical applications, the Josephson junction is usually modeled as a resistively and capacitively shunted junction (RCSJ) model. In this model, the Josephson junction has a critical current I_0 and in parallel there are a capacitance C and a resistance R of the junction. Using Kirchhoff's law the current through the junction can be written as

$$I_0\sin(\phi) + \frac{V}{R} + C\dot{V} = I_B. \tag{1.16}$$

V is eliminated using the second Josephson relation and the time can be changed to the dimensionless time $\tau = \omega_{pl}t$, where $\omega_{pl} = \sqrt{2\pi I_0/(C\Phi_0)}$ is plasma frequency of the junction. We also define a quality factor of the junction $Q = \omega_p RC$. The dynamics of the phase ϕ can be viewed as the equation of motion of a point mass in a field of force

$$\frac{d^2\phi}{d\tau^2} + \frac{1}{Q}\frac{d\phi}{d\tau} = \frac{I_B}{I_0} - \sin(\phi) = -\frac{2\pi}{\Phi_0 I_0}\frac{\partial U}{\partial \phi}, \tag{1.17}$$

where we defined *tilted washboard potential* $U(\phi)$ of the Josephson junction with the amplitude of the potential given by the Josephson energy $E_J = I_0\Phi_0/2\pi$

$$U(\phi) = E_J\left(1 - \cos\phi - \frac{I_B}{I_0}\phi\right). \tag{1.18}$$

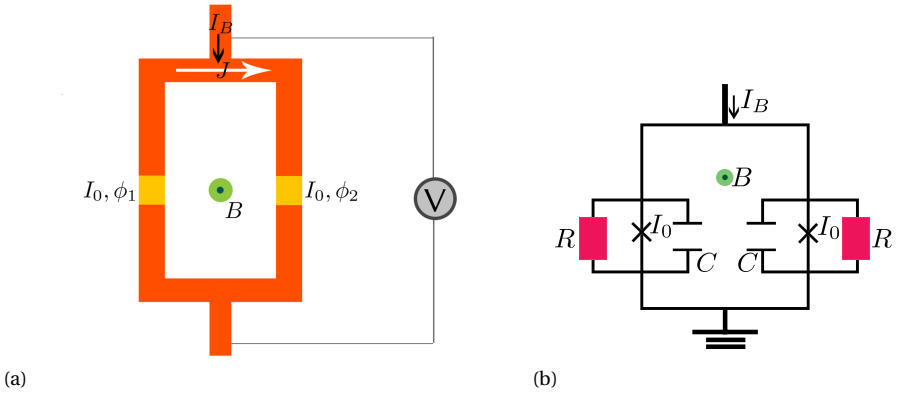

Figure 1.3: (a) Schematic drawing of the dc SQUID. It consists of two Josephson junctions in parallel. The loop is biased by a current I_B and the voltage drop V. (b) Equivalent circuit of the SQUID using RCSJ model.

1.3.1. DC SQUID

The dc SQUID (superconducting quantum interference device) consists of two Josephson junctions connected in parallel on a superconducting loop (see Fig. 2.1(a)). The first experiment performed by Jaklevic *et al* demonstrated quantum interference between two thin-film Josephson junctions [30]. The authors observed the rapid oscillations, which are due to quantum interference, analogous to two-slit interference in optics, and their period is given by the field required to generate one flux quantum in the SQUID loop. The advantage of the SQUID is very sensitive detection of the magnetic flux. SQUIDs are capable of measuring any quantity which can be converted to magnetic flux, for example, magnetic field, magnetic susceptibility, current, voltage, and mechanical displacement.

To proceed, we relate the magnetic flux through the SQUID with the gauge-invariant phase difference. We ignore the effect of the magnetic field on the electrodes and focus on its effect on the gauge-invariant difference. We can write a flux Φ threading through the loop via $\mathbf{A}$ taking into account that $\mathbf{A} = \Phi_0/2\pi\nabla\chi$ in the electrodes

$$\Phi = \oint \mathbf{A}\cdot d\mathbf{s} = \frac{\Phi_0}{2\pi}\int_{\text{electrodes}} \nabla\chi\cdot d\mathbf{s} + \int_{\text{barriers}} \mathbf{A}\cdot d\mathbf{s}. \tag{1.19}$$

The phase χ of electrodes must be single-valued meaning that the first term plus the sum of the finite phase differences of each junction across the links $\frac{\Phi_0}{2\pi}\Delta\phi_1$ and $-\frac{\Phi_0}{2\pi}\Delta\phi_2$ must be zero (mod 2π). Combining this with integral over links and using eq.(1.15), one can arrive at the condition for the phase difference of two junctions

$$\phi_1 - \phi_2 = \frac{2\pi\Phi}{\Phi_0} + 2\pi n, \tag{1.20}$$

where n is an integer.

In most dc SQUID setups each junction has a resistive shunt to suppress hysteresis on $I-V$ characteristic and can be modeled with the RCSJ model [31] as in Fig. 2.1(b). Each Josephson junction has a critical current I_0 assuming SQUID is symmetric. We

introduce the bias current I_B and the circulating current in the loop J to the SQUID then the dynamics of each phase is describes by the differential equations

$$\begin{cases} \frac{d^2\phi_1}{d\tau^2} + \frac{1}{Q}\frac{d\phi_1}{d\tau} = \frac{I_B}{2I_0} - \frac{J}{I_0} - \sin(\phi_1), \\ \frac{d^2\phi_2}{d\tau^2} + \frac{1}{Q}\frac{d\phi_2}{d\tau} = \frac{I_B}{2I_0} + \frac{J}{I_0} - \sin(\phi_2). \end{cases} \tag{1.21}$$

Since the phase difference of two junctions $\varphi_- = (\phi_1 - \phi_2)/2$ is fixed by the flux, the dynamics of the SQUID governs the overall phase $\varphi_+ = (\phi_1 + \phi_2)/2$

$$\frac{d^2\varphi_+}{d\tau^2} + \frac{1}{Q}\frac{d\varphi_+}{d\tau} = \frac{I_B}{2I_0} - \sin(\varphi_+)\cos(\varphi_-) = -\frac{2\pi}{\Phi_0 I_0}\frac{\partial U}{\partial \varphi_+}, \tag{1.22}$$

where we defined the potential $U(\varphi_+)$ of the SQUID

$$U = -E_J\left(\cos(\varphi_+)\cos(\varphi_-) + \frac{I_B}{2I_0}\varphi_+\right). \tag{1.23}$$

SQUID can be also views as a LC circuit. Then, we can define an effective Josephson inductance $V = L_J \partial I/\partial t$ of the SQUID

$$L_J = \frac{\Phi_0}{4\pi I_0 \cos(\varphi_-)}. \tag{1.24}$$

The Josephson inductance depends on the phase difference and subsequently on the flux. If we incorporate the mechanical resonator into the loop, then the total flux will change when the resonator with the length l and displacement $x(t)$ oscillates : $\Phi = \Phi_b + Blx$, where Φ_b is the flux through the SQUID area. Hence the cavity frequency will be modulated by the mechanical resonator

$$\omega_c(x) = \sqrt{\frac{1}{L_J C}} = \sqrt{\frac{4\pi I_0 \cos\left(\frac{2\pi(\Phi_b + Blx)}{\Phi_0}\right)}{\Phi_0 C}}. \tag{1.25}$$

1.4. OPTOMECHANICALLY INDUCED TRANSPARENCY

One of the important phenomenon in optomechanics is optomechanical induced transparency(OMIT). It takes its roots from electromagnetically induced transparency(EIT), which occurs in the multilevel atoms by coherent interaction of the laser with the atomic states leading to the quantum interference in the excitation pathways [32]. In this way the absorption and refraction can be eliminated at the resonant frequency of a transmission for the weak probe field. In the optical response this effect observed as a narrow spectral transparency window induced by a drive laser. The benefit of EIT lies in its potential great applications for the nonlinear optics and quantum information processing because in this way slowing, advancing and switching light is possible and even a complete stop of light enables optical pulse storage.

OMIT is equivalent to EIT but instead in the cavity optomechanical systems and resolved sideband regime, where cavity decay rate is much weaker than mechanical frequency. Theoretical predictions of OMIT followed by experimental observations starting

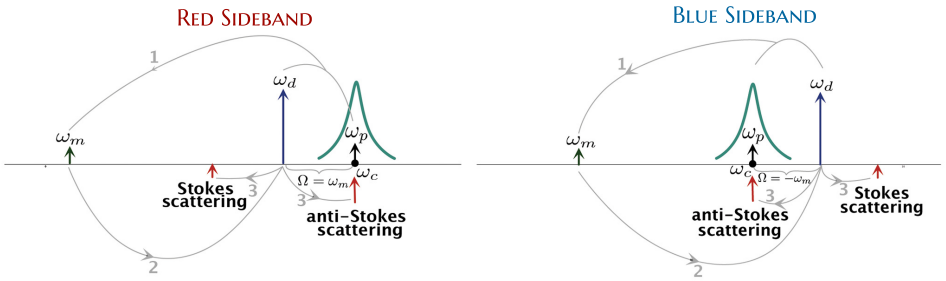

Figure 1.4: The schematics, which illustrates the process of the interference between photons scattered from the drive field due to the modulation of mechanical resonator and photons of the probe field.

as of 2010 [33]. Since in this thesis we are focused on the microwave rather than optical cavity, we discuss OMIT phenomenon in the microwave context.

In an OMIT setup, two microwave fields are injected inside the cavity. A strong drive field $S_d e^{-i\omega_d t}$ with drive frequency ω_d at lower (red-detuned) or upper (blue-detuned) mechanical sideband frequency $\omega_d = \omega_c - \omega_m$ or $\omega_d = \omega_c + \omega_m$, respectively, and a weak probe field $S_p e^{-i\omega_p t}$ with probe frequency ω_p measures the cavity response by sweeping the probe tone in the vicinity of ω_c. The presence of both fields creates a radiation pressure force oscillating at the detunning between the probe and drive fields $\Omega = \omega_p - \omega_d$. If the detunning matches mechanical frequency for the red sideband or negative mechanical frequency for the blue sideband then mechanical resonator is driven resonantly. Mechanical resonator in turn modulates the drive field and results in the Stokes- and anti-Stokes scattering of microwave photons from the drive field. When the system is in resolved sideband regime, the Stokes scattering with frequency $\omega_d - \Omega$ is far off cavity resonance and can be ignored. The anti-Stokes scattering has frequency $\omega_d + \Omega$, which is exactly the frequency of the probe field. Furthermore, this process is also phase coherent with the probe leading to an interference with the original probe field measuring the cavity response. The schematic picture of this process for red and blue sidebands is shown on Fig.1.4.If the interference is destructive then the probe and drive field suppress the intracavity field and lead to OMIT effect. However, for the single-port cavity we can only measure the reflection and, hence, this effect is called optomechanically induced reflection (OMIR). If the interference is constructive then these two fields amplify the intracavity field and we observe optomechanically induced absorption (OMIA), which is equivalent to the electromagnetically induced absorption (EIA) in the atomic physics.

Now understanding the physical picture of the phenomenon, we can solve the mathematical equations describing OMIT captured by the Langevin equations of motion for the cavity modes in terms of the creation and annihilation operators ($\hat{a}^\dagger$, $\hat{a}$) and mechanical modes in terms of the displacement operator ($\hat{x}$)

$$\frac{d}{dt}\hat{a}(t) = \left(i\Delta - \frac{\kappa}{2}\right)\hat{a}(t) - iG\hat{x}(t)\hat{a}(t) + \sqrt{\eta\kappa}(S_d + S_p e^{i\Omega t}), \tag{1.26}$$

$$m\left(\frac{d^2}{dt^2}\hat{x}(t) + \Gamma_m \frac{d}{dt}\hat{x}(t) + \omega_m^2 \hat{x}(t)\right) = -\hbar G\hat{a}^\dagger(t)\hat{a}(t) \tag{1.27}$$

with the difference of the cavity and drive frequencies $\Delta = \omega_d - \omega_c$, which is set by red or blue sidebands and Γ_m being the mechanical damping rate of the resonator. The cavity coupling parameter is given by $\eta = \kappa_e/(\kappa_0 + \kappa_e) = \kappa_e$ with κ_0, κ_e and κ denote the intrinsic, the external, and the total dissipation rates, respectively.

Since the probe field is much weaker than the drive we can separately treat them and linearize optomechanical dynamics for the cavity field $\hat{a}(t) = \bar{a} + \delta\hat{a}(t)$ and mechanical displacement $\delta\hat{x}(t) = \bar{x} + \delta\hat{x}(t)$ around the steady-state mean values. The mean values can be easily found by disregarding the probe field and setting all time dependent derivative to zero

$$\bar{a}^2 = \frac{\eta\kappa}{\overline{\Delta}^2 + \kappa^2/4} S_d^2, \tag{1.28}$$

$$\bar{x} = -\frac{\hbar G \bar{a}^2}{m\omega_m^2}, \tag{1.29}$$

where $\overline{\Delta} = \Delta - G\bar{x}$ is an effective cavity detuning including the frequency shift due the static mechanical displacement. We also learned that there is only anti-Stokes scattering that matters meaning $\delta\hat{a}(t) = Ae^{-i\Omega t}$. Then the mechanical resonator oscillates with the same frequency Ω and one can write a solution $\delta\hat{x}(t) = Xe^{-i\Omega t} + X^* e^{i\Omega t}$. The solutions to these complex amplitudes of the cavity and mechanical modes can be evaluated using the Langevin equations for the red sideband and Ω close to the mechanical frequency

$$X = -igx_{\mathrm{ZPF}}\chi_m A, \tag{1.30}$$

$$A = \frac{\sqrt{\eta\kappa}\chi_c}{1 + g^2\chi_m\chi_c} S_p, \tag{1.31}$$

where $\chi_m(\Omega) = 1/(-i(\Omega - \omega_m) + \Gamma_m/2)$ is the susceptibility of the mechanical resonator, $\chi_c(\Omega) = 1/(-i(\Omega + \overline{\Delta}) + \kappa/2)$ is the susceptibility of the cavity. For the blue sideband and Ω close to the negative mechanical frequency the solutions has the same form but the mechanical susceptibility is taken with the minus sign ($-\chi_m(\Omega)$).

The transmission or as in the case of single-port cavity the reflection coefficient is defined as the ratio of the output and input fields at the probe frequency [33]. Experiment observing OMIT measures this coefficient at different probe frequencies and his mathematically expressed as following

$$t_r = 1 - \sqrt{\eta\kappa}\frac{A}{S_p}. \tag{1.32}$$

To analyze the reflection coefficient solutions we choose an overcoupled cavity ($\eta > 0.5$) and a realistic set of parameters for the cavity and the mechanical resonator. Fig.1.5 shows OMIA and OMIR for the blue and red sideband. For the red sideband the weak drive power results in the OMIA effect and while the drive power is increased an absorption feature becomes a reflection. This happens due to the increase in the intrinsic dissipation rate $\kappa_0 + 4g^2/\Gamma_m$ when the many-photon optomechanical coupling is increased, which results in the total intrinsic dissipation rate higher than the external dissipation rate. Similar situation occurs for the mechanical damping $\Gamma_m + 4g^2/\kappa$ and then it leads

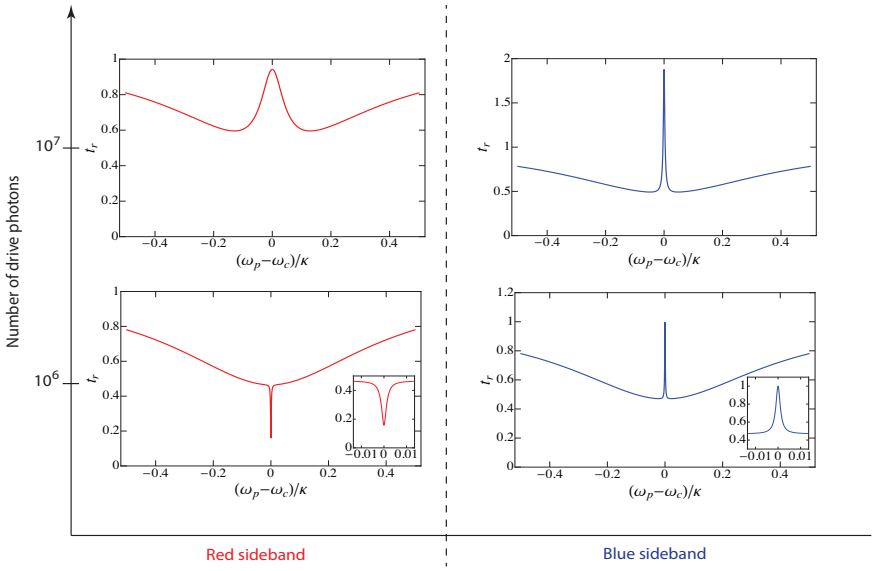

Figure 1.5: OMIA and OMIR effects for the red and blue sidebands and two different drive powers. For weak drive power the zoomin into the transparency window is shown inside the main plot. The shape of the peak/dip has Lorentzian shape. The set of parameters is used to visualize t_r coefficient: $\kappa = 2\pi 150$ kHz, $\kappa_e = 2\pi 110$ kHz, $g/\bar{a} = 2\pi 0.65$ Hz, $\omega_m = 2\pi 50$ MHz, $m = 0.3$ pg, and $\Gamma_m = 2\pi 400$ Hz.

to the obvious broadening of the transparency window. For the blue sideband and overcoupled cavity for the weak and strong drive power there is only OMIR. However, for the stronger drive power the OMIR peak has increased in height, which suggests that more probe photons are on the output than were on the input leading to an amplification of the signal. The amplification can be understood by increased g so that $4g^2/\Gamma_m$ becomes larger than intrinsic cavity dissipation κ_0 and then total intrinsic dissipation cavity rate becomes negative. The same picture of the OMIA and OMIR is observed in the experiment between a superconducting microwave cavity and a graphene mechanical resonator [34]. For the undercoupled cavity the panels are switched between red and blue sidebands so that for the red sideband there is only OMIR and for the blue sideband there is OMIR and OMIA for different drive powers.

For OMIA and OMIR, we can quantify the features of the peak using the optomechanical cooperativity, defined as $C = \frac{4g_0^2 n_d}{\Gamma_m \kappa}$. The minimum value of the reflection coefficient for OMIA is given by much simplified expression $\left|\frac{2\eta}{1+C} - 1\right|$, which is the maximum value of reflection coefficient for OMIR in the transparency window. In the limit of no optomechanical coupling ($C = 0$), we recover $|2\eta - 1|$ expression for the minimum for a single-port reflection cavity, which sets the base line of OMIA/OMIR feature. The linewidth of OMIA/OMIR feature is given by $(1 + C)\Gamma_m$, where the additional term $C\Gamma_m$ originates from the backaction effects and can be tuned by n_d. Furthermore, amplitude of the mechanical resonator can also be cast into a convenient form, $X = x_{\mathrm{ZPF}} \left(\frac{C}{1+C}\right) \left(\frac{\kappa_e}{g}\right) \sqrt{n_p}$ with n_p being a number of probe photons. It is instructive to see that for low cooperativity

($C < 1$), the mechanical amplitude can be tuned by both the probe and drive tone as $X \propto \sqrt{n_d n_p}$. On the other hand, in the limit $C > 1$, the mechanical amplitude is proportional to $\sqrt{n_p/n_d}$, suggesting that an increase in drive field leads to optomechanical damping and hence a reduction in the mechanical amplitude. Although the depth of the OMIA dip in the reflection coefficient does not depend on the probe power, the mechanical force of the resonator does: increasing the probe power for a fixed drive power will exert a larger oscillating force on the resonator, and can drive it into the nonlinear regime [35]. In the limit $\kappa \gg 2g \gg \Gamma_m$, the measurement of the OMIA/OMIR allows to directly probe the responsivity of the mechanical resonator giving its amplitude and dissipation rate, thus making it a sensitive technique.

1.5. OUTLINE OF THIS THESIS

In this thesis we theoretically study the effects of the nonlinearity of the cavity or mechanical resonator in microwave optomechanics. The first part of the thesis is focused on the dc SQUID cavity, which is intrinsically nonlinear, and embedded harmonic mechanical resonator. We start with classical investigation of the nonlinear cavity effect on the dynamics of the SQUID coupled to the mechanical resonator in Chapter 2. In Chapter 3, we take the next step and quantize this system as well as taking into account the SQUID asymmetry of two Josephson junctions in critical currents. We obtain the couplings of this system and discuss possibility of reaching ultrastrong coupling regime. In Chapter 4, the Kerr nonlinearity of the SQUID affects the cavity frequency and dissipation. These shifts are derived using variational theorem for path integrals.

The second part of this thesis studies optomechanical response of the cavity and nonlinear mechanical resonator. By driving optical or microwave cavity hard enough the system can be taken to the Duffing regime. In Chapter 5, the OMIA and OMIR features of the nonlinear response are analyzed in the details including drive frequency detuning from the red or blue sidebands, considering overcoupled and undercoupled cavity, and going beyond Duffing mechanical resonator. Chapter 6 presents the fittings to the experiment with a graphene mechanical resonator coupled to the microwave cavity based on the theory developed in chapter 5. Moreover, the obtained effect of the negative nonlinear damping of the mechanical resonator is also addressed.

REFERENCES

[1] P. Lebedew, Ann. Phys. (Leipzig) **6**, 433 (1901).

[2] E. F. Nichols and G. F. Hull, Phys. Rev. **13**, 307 (1901).

[3] A. Ashkin, Phys. Rev. Lett. **24**, 156 (1970).

[4] T. W. Hänsch and A. L. Schawlow, Opt. Commun. **13**, 68 (1975).

[5] D. J. Wineland and H. Dehmelt, Bulletin of the American Physical Society **20**, 637 (1975).

[6] V. B. Braginsky and A. B. Manukin, Sov. Phys. JETP **25**, 653 (1967).

[7] V. B. Braginsky, A. B. Manukin and M. Y. Tikhonov, Sov. Phys. JETP **31**, 829 (1970).

[8] A. Dorsel, J. D. McCullen, P. Meystre, E. Vignes, and H. Walther, Phys. Rev. Lett. **51**, 1550 (1983).

[9] T. J. Kippenberg and K. J. Vahala, Science **321**, 172 (2008).

[10] F. Marquardt and S. M. Girvin, Physics **2**, 40 (2009).

[11] P. Meystre, Ann. Phys. (Berlin) **525**, 215 (2013).

[12] M. Aspelmeyer, P. Meystre, and K. Schwab, Physics Today **65**, 29 (2012).

[13] M. Aspelmeyer, T. J. Kippenberg, and F. Marquardt, Rev. Mod. Phys. **86**, 1391 (2014).

[14] M. Poot and H. S. J. van der Zant,, Phys. Rep. **511**, 273 (2012).

[15] C. A. Regal, J. D. Teufel, and K. W. Lehnert, Nature Phys. **4**, 555 (2008).

[16] A.D. O'Connell, M. Hofheinz, M. Ansmann, R.C. Bialczak, M. Lenander, E. Lucero, M. Neeley, D. Sank, H. Wang, M. Weides, J. Wenner, J. M. Martinis, and A. N. Cleland, Nature **464**, 697 (2010).

[17] J. D. Teufel, T. Donner, D. Li, J. W. Harlow, M. S. Allman, K. Cicak, A. J. Sirois, J. D. Whittaker, K. W. Lehnert, R. W. Simmonds, Nature **475**, 359 (2011).

[18] C. W. Gardiner and P. Zoller,*Q*uantum Noise (Springer Series in Synergetics), (2004)

[19] A. Wallraff, D. Schuster, A. Blais, L. Frunzio, R.S. Huang, J. Majer, S. Kumar, S.M. Girvin, R.J. Schoelkopf, Nature **431**, 162 (2004).

[20] A. D. Armour, M .P. Blencowe, and K. C. Schwab, Phys. Rev. Lett. **88**, 148301 (2002).

[21] J. B. Hertzberg, T. Rocheleau, T. Ndukum, M. Savva, A. A. Clerk, K. C. Schwab,Nat. Phys **6**, 213 (2010).

[22] M. D. LaHaye, J. Suh, P. M. Echternach, K. C. Schwab, M. L. Roukes, Nature **459**, 960 (2009).

[23] L. Hao, J. C. Gallop, D. Cox, Appl. Phys. Lett. **95**, 113501 (2009).

[24] F. London, Proc. Roy. Soc. (London) A **152**, 24 (1935); Phys. Rev. **74**, 562(1948).

[25] J. Bardeen, L. N. Cooper, and J. R. Schrieffer, Phys. Rev. **108**, 1175 (1957).

[26] V. L. Ginzburg and L. D. Landau, Zh. Eksp. Teor. Fiz. **20**, 1064 (1950).

[27] B. D. Josephson, Phys. Lett. **1**, 251 (1962); Adv. Phys. **14**, 419 (1965).

[28] M. Tinkham, *Introduction to superconductivity*, Mc-Graw Hill (1996).

[29] R. P. Feynman, R. B. Leighton, and M. Sands, *The Schrödinger equation in a classical context: A seminar on superconductivity. In The Feynman Lectures on Physics.*, vol. 3, Addison-Wesley (1965).

[30] R. C. Jaklevic, J. Lambe, A. H. Silver, and J. E. Mercereau, Phys. Rev. Lett. **12**, 159–160 (1964).

[31] J. Clarke and A. I. Braginski, *The SQUID Handbook. Vol I. Fundamentals and Technology of SQUIDs and SQUID Systems*, Wiley (2004).

[32] M. Fleischhauer, A. Imamoglu, and J. P. Marangos, Rev. Mod. Phys. **77**, 633 (2005).

[33] S. Weis, R. Rivire, S. Delglise, E. Gavartin, O. Arcizet, A. Schliesser, and T. J. Kippenberg, Science **330**, 1520 (2010).

[34] V. Singh, S. J. Bosman, B. H. Schneider, Y. M. Blanter, A. Castellanos-Gomez, G. A. Steele, Nature Nanotech. **9**, 820 (2014).

[35] V. Singh, O. Shevchuk, Ya. M. Blanter, and G. A. Steele, Phys. Rev. B **93**, 245407 (2016).

2

MULTISTABILITY OF A JOSEPHSON PARAMETRIC AMPLIFIER

O. Shevchuk, R. Fazio and Ya. M. Blanter

We study the dynamics of Josephson parametric amplifier (JPA) coupled to a mechanical oscillator, as realized with a dc Superconducting Quantum Interference Device (SQUID) with an embedded movable arm. We analyze this system in the regime when the frequency of the mechanical oscillator is comparable in magnitude to the plasma oscillation of the SQUID. When the nanomechanical resonator is driven, it strongly affects the dynamics of the JPA. We show that this coupling can considerably modify the dynamics of the JPA and induce its multistability rather than common bistability. This analysis is relevant if one considers a JPA for detection of mechanical motion.

This chapter has been published in Phys. Rev. B **90**, 205411 (2014).

2.1. INTRODUCTION

Recently, there has been considerable interest in coupling mechanical resonators to optical and microwave radiation, as well as to electric conduction [1–3]. Resulting devices, nanoelectromechanical and optomechanical systems, combine excellent mechanical and electrical/optical properties, such as low dissipation both in the cavity and in the mechanical resonator. These systems have already displayed a rich variety of interesting physical phenomena. At the same time, they have found applications, *e.g.*, as sensors and transducers. Most of the experiments so far have been carried out in the regime of classical mechanical motion, though recently the quantum regime has been demonstrated as well [4–8].

An important problem in this field is to find efficient schemes to detect the mechanical motion. To this end, one should find systems whose properties are significantly affected by the mechanical resonator, consequently carrying a distinct signature of this coupling. On the other side, the coupling to the detector has sizable consequences on the resonator too. Backaction, understood as an effect of the detector (for example, an optical or a microwave cavity) on the properties of the mechanical resonator, is one of the fundamental issues in the fields of nano- and optomechanics [2]. Even though backaction is not always wanted in the experiment and can be suppressed with backaction-evasion techniques [9], one can nevertheless use it as an advantage in order to manipulate, for example, to cool [10] and to heat, the resonator. In optomechanics, backaction is provided by radiation pressure and its properties are very well established, both theoretically and experimentally [3]. More recently, backaction in nanomechanical devices, caused by electrostatic interactions [11, 12] and by Lorentz force [13, 14], both in the classical regime, has been demonstrated experimentally. It is important that in all of these examples, the mechanical resonators were in the linear regime. The backaction effect consisted of the modification of the frequency (optical spring) and the quality factor, as well as the induced nonlinearity of the mechanical resonator.

Within the area of superconducting nanomechanical systems, superconducting quantum interference device (SQUID)-based circuits have been intensively investigated. A dc SQUID and its integration with the mechanical resonator has been theoretically proposed [15–19] and experimentally demonstrated [13, 14, 20]. The detection of the mechanical oscillations was possible through an analysis of the dynamics of the electrical response of the superconducting circuit. A SQUID is a nonlinear cavity. Nonlinear effects in opto- and nanomechanical systems recently drew a lot of attention (see Ref. [3]). They originate from different sources — nonlinear coupling between the resonator and the cavity, mechanical nonlinearities of resonators made of carbon nanotubes and graphene, and also from the cavity itself. Our aim is to study the role of nonlinearity in the dynamics of a SQUID coupled to a mechanical resonator. Our interest is two-fold. On one hand, we would like to explore further the impact of mechanical oscillation on the stability of the SQUID dynamics, thinking to eventually use this information as a detection mean. On the other hand, backaction in the presence of strong nonlinearities requires a closer inspection. Due to the complexity of dynamic behavior of nonlinear systems, one can expect that even a small effect of backaction can considerably alter the properties of a nonlinear oscillator.

In this chapter, we make the first step in this direction. We consider a dc SQUID cou-

pled to a driven harmonic mechanical resonator. Whereas formally this system is similar to the one studied experimentally in Ref. [20], to explore the regime where the backaction is the strongest, we consider the situation when the mechanical and the cavity frequencies are of the same order. This is the regime when the dc SQUID acts as a Josephson parametric amplifier (JPA) [21, 22] and displays a multistable behavior: the amplitude of the oscillations of a driven JPA can assume two values in a wide frequency range; such behavior was seen in the response of the nonlinear oscillators to the parametric forcing [23–25]. This feature of the JPA can be used to readout the state of the qubit, since different amplitudes correspond to different states of the qubit. We consider the situation when both the field of the cavity (the phase of the Josephson junctions) and the coordinate of the mechanical motion are classical variables. In our chosen setup, the JPA is parametrically driven. Assuming a weak coupling between the JPA and the mechanical oscillator, we demonstrate that the backaction can considerably modify the dynamics of the JPA and lead to multistability rather than bistability. We obtain this result analytically, approximating the JPA by the Duffing oscillator, and also confirm it numerically, relaxing this approximation. The results of this chapter demonstrate that backaction can indeed essentially modify the behavior of a nonlinear oscillator. The present analysis is therefore relevant when considering the JPA as a detector for mechanical motion. In comparison with the qubit detection, where the hysteretic regime permits a readout, the mechanical motion detection uses the whole finite amplitude regime. Therefore, here the JPA acts as a threshold detector. Moreover, the multistability results in the extra hysteretic region, which enhances the sensitivity and range of the detector.

This chapter is organized as follows. In Sec. 2.2, we describe the device and set up the model to describe it. In Sec. 2.3, we consider the case of negligible coupling (no backaction of the SQUID on the mechanical oscillator) and solve the corresponding equations. In Sec. 2.4, the corrections to the amplitude due to backaction are found by considering the coupling term in the equations of motion. The conclusions of this work are summarized in Sec. 2.5.

2.2. THE MODEL

We consider a dc SQUID with two (nearly) identical Josephson junctions coupled to a mechanical resonator. The resonator is formed by a suspended segment of superconductor. We only consider one mode of the mechanical resonator. It can be externally driven, which is experimentally realized by fabricating the suspended part of the setup close to a piezoelectric element. The schematic overview of the system is shown in Fig.2.1. The coupling between the SQUID and the mechanical resonator is based on the fact that the critical current of the SQUID periodically depends on the magnetic flux, making it a very sensitive magnetic flux detector. The oscillations of the resonator induce a variation of the area thus affecting the flux. When the mechanical resonator is driven, the flux modulation leads to a parametric driving for the SQUID [15, 16].

The mechanical resonator is modeled as a harmonic oscillator driven by external periodic force $F_d \cos(\omega_d t)$ with driving frequency ω_d. The magnetic flux passing through the SQUID loop is dependent on the position of the resonator, $\Phi = \Phi_{ext} + \beta_0 B l x$, where $\Phi_{ext} = \alpha_0 B A$ represents the flux through the area A when the resonator is at rest, B is the magnetic field, and y is the displacement from the equilibrium position of the resonator.

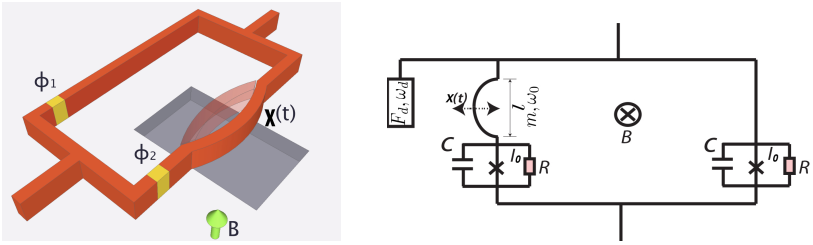

(a) (b)

Figure 2.1: (a) The picture of the system: the rectangular-shaped dc SQUID with the suspended beam. The magnetic field is orthogonal to the SQUID. The oscillation of the beam is in the loop plane. Therefore, the displacement x generates change in the magnetic flux passing through the loop. (b) The schematic overview of the setup. The system is driven with force F_d. Josephson junctions are modeled as resistively and capacitively shunted junctions(RCSJ).

The geometric factors of α_0 and β_0 (both of the order of unity) depend on the direction of the magnetic field. Finally, the inductance of the SQUID is assumed to be negligibly small.

To analyze the dynamics of this system one can look at the sum and difference of gauge-invariant phases across each Josephson junction, respectively, $\varphi_\pm = (\phi_1 \pm \phi_2)/2$. The condition that the superconductor order parameter is single valued leads to the relation between the phase difference and total flux bias,

$$\varphi_- = \pi \frac{\Phi}{\Phi_0} = \phi_b + \xi x + 2\pi n. \tag{2.1}$$

Here, n is an integer, $\Phi_0 = \pi\hbar c/e$ is a superconducting flux quantum, and the geometric constants of the system are

$$\phi_b = \frac{\pi\alpha_0 BA}{\Phi_0} \quad \text{and} \quad \xi = \frac{\pi\beta_0 Bl}{\Phi_0}. \tag{2.2}$$

The Hamiltonian $H = H_x + H_\varphi + U$ of the SQUID with the movable arm is thus

$$H_x = \frac{p^2}{2m_r} + \frac{m_r\omega_m^2 x^2}{2} - F_d x \sin(\omega_d t), \tag{2.3}$$

$$H_\varphi = \frac{p_\varphi^2}{2m_\varphi}, \tag{2.4}$$

$$U = -2E_J \cos(\varphi_-)\cos(\varphi_+), \tag{2.5}$$

where $E_J = I_0\Phi_0/(2\pi)$ is the Josephson energy, p, m_r, and ω_m are the momentum, the mass, and the frequency of the mechanical resonator, respectively, and p_φ and m_φ are the momentum and the mass of the SQUID phase. The effective Hamiltonian is composed of the contribution from the resonator H_x, the kinetic energy of the SQUID H_φ, and the potential energy of the SQUID U. Since the potential energy U depends on the phase difference it provides the coupling between the SQUID and the oscillator through

Eq. (2.1). From our system it follows that the momentum of the mechanical oscillator is $p = m_r \dot{x}$. The phase momentum of the SQUID is given by $p_\varphi = m_\varphi \dot{\varphi}_+ = E_J \dot{\varphi}_+^2 / \omega_{pl}$, where $m_\varphi = 2E_J/\omega_{pl}$ is the mass of the phase, $\omega_{pl} = \sqrt{2\pi I_0/(C\Phi_0)}$ is the plasma frequency, and I_0 and C are the critical current and the capacitance of each Josephson junction.

Clearly, the potential energy of the SQUID is a nonlinear function in φ_- and φ_+. Since we are interested in the two dynamical variables x and φ_+, the dependence on the phase difference should be changed to the dependence on the oscillator displacement. In the current experiments, the ratio ξx is very small which enables us to expand the potential energy so that

$$U = -2E_J \left[\cos(\phi_b) - \sin(\phi_b)\xi x\right] \cos(\varphi_+). \tag{2.6}$$

2.3. EQUATIONS OF MOTION

The dynamics of the system is governed by the following equations of motion,

$$\ddot{x} + \Gamma_m \dot{x} + \omega_m^2 x = \frac{F_d}{m_r} \cos(\omega_d t) - \frac{2E_J \xi \sin(\phi_b)}{m_r} \cos(\varphi_+), \tag{2.7}$$

$$\frac{\ddot{\varphi}_+}{\omega_{pl}^2} + \frac{\delta}{\omega_{pl}} \dot{\varphi}_+ + \big(\cos(\phi_b) - \sin(\phi_b)\xi x\big) \sin(\varphi_+) = 0. \tag{2.8}$$

where $\Gamma_m = \omega_m/Q_y$ and $\delta = 1/Q_\varphi$ are the dissipation rates for the resonator and the SQUID, with Q_y and Q_φ being the respective quality factors.

The two equations are coupled by the last term in Eq. (2.7), which expresses the backaction of the SQUID on the mechanical resonator, and by the term proportional to ξx in Eq. (2.8), which provides the effect of the resonator on the SQUID. Note that both couplings are proportional to ξ. For $\xi = 0$, the equations are decoupled: The SQUID is not driven, $\varphi_+ = 0$, whereas the driven mechanical resonator shows the usual response,

$$x(t) = A(\omega_d) \cos(\omega_d t) + D(\omega_d) \sin(\omega_d t) \tag{2.9}$$

with

$$A(\omega_d) = \frac{F_d}{m_r} \frac{(\omega_m^2 - \omega_d^2)}{(\omega_m^2 - \omega_d^2)^2 + \Gamma_m^2 \omega_d^2}, \tag{2.10}$$

$$D(\omega_d) = \frac{F_d}{m_r} \frac{\Gamma_m \omega_d}{(\omega_m^2 - \omega_d^2)^2 + \Gamma_m^2 \omega_d^2}. \tag{2.11}$$

In the following, we will analyze the consequences of the coupling on the classical nonlinear dynamics of the SQUID. We first disregard the backaction of the SQUID [dropping the last term on the right-hand size of Eq. (2.7)], but still consider the effect of the mechanical resonator on the SQUID. In this case, the SQUID is parametrically driven. There is always a trivial (zero) solution for the overall phase drop φ_+; the non-trivial one is found by substituting $y(t)$ from Eq. (2.9). For convenience, we introduce the parameters

$$\begin{cases} \omega = \frac{\omega_d}{2\omega_{pl}}, \quad \omega_\phi^2 = \cos(\phi_b), \quad \tau = \omega_{pl} t, \\ \gamma = \xi \sin(\phi_b) A(\omega), \quad \beta = \xi \sin(\phi_b) D(\omega), \end{cases} \tag{2.12}$$

and choose the regime where $\cos(\phi_b) > 0$, so that Eq. (2.8) is rewritten as

$$\ddot{\varphi}_+ + \omega^2\varphi_+ = -\delta\dot{\varphi}_+ + \omega^2\varphi_+ - \omega_\phi^2 \sin(\varphi_+) + \left[\gamma\cos(2\omega\tau) + \beta\sin(2\omega\tau)\right]\sin(\varphi_+). \tag{2.13}$$

Under realistic experimental conditions , the coefficients in front of the phase-dependent functions on the right-hand side of the equation are usually small. Setting them to zero gives the unforced and undamped linear oscillator. Therefore, we can employ widely used analytical techniques for solving the Duffing oscillator [26], based on a perturbation around a solution to the linear oscillator. One of the methods to obtain the perturbative correction is based on the van der Pol transformation,

$$u = \varphi_+\cos(\omega\tau) - \frac{\dot{\varphi}_+}{\omega}\sin(\omega\tau), \tag{2.14}$$

$$v = -\varphi_+\sin(\omega\tau) - \frac{\dot{\varphi}_+}{\omega}\cos(\omega\tau), \tag{2.15}$$

where u and v are slowly varying quantities. The transformation turns the second-order differential equation into a system of two first-order differential equations,

$$\begin{aligned}\omega\dot{u} = &-\sin(\omega\tau)\left[\omega\delta(u\sin(\omega\tau) + v\cos(\omega\tau)) + \omega^2\left(u\cos(\omega\tau) - v\sin(\omega\tau)\right)\right.\\ &-\omega_\phi^2\sin((u\cos(\omega\tau) - v\sin(\omega\tau))) + \gamma\cos(2\omega\tau)\sin\left(u\cos(\omega\tau) - v\sin(\omega\tau)\right)\\ &\left.+\beta\sin(2\omega\tau)\sin\left(u\cos(\omega\tau) - v\sin(\omega\tau)\right)\right],\end{aligned} \tag{2.16}$$

$$\begin{aligned}\omega\dot{v} = &-\cos(\omega\tau)\left[\omega\delta(u\sin(\omega\tau) + v\cos(\omega\tau)) + \omega^2\left(u\cos(\omega\tau) - v\sin(\omega\tau)\right)\right.\\ &-\omega_\phi^2\sin((u\cos(\omega\tau) - v\sin(\omega\tau))) + \gamma\cos(2\omega\tau)\sin\left(u\cos(\omega\tau) - v\sin(\omega\tau)\right.\\ &\left.+\beta\sin(2\omega\tau)\sin\left(u\cos(\omega\tau) - v\sin(\omega\tau)\right)\right].\end{aligned} \tag{2.17}$$

In order to solve such system, the method of averaging over the period $T = 2\pi/\omega$ is used. The idea is to approximate the equation in the form $\dot{y} = f(y,t)$ by averaging out fast oscillatory dynamics, obtaining $\dot{y'} = 1/T\int_0^T f(y',t)dt \equiv \bar{f}(y')$. For that, slowly varying quantities are written in polar coordinates, i.e., $u = r\cos(\theta)$ and $v = r\sin(\theta)$. Then, the integrals of nonlinear functions can be found from the properties of the Bessel functions [27],

$$\int_{-\pi}^{\pi} e^{i(u\cos(\tau)+v\sin(\tau))} \qquad \cos(k\tau)d\tau = 2\pi i^k\cos(k\theta)J_k(r), \tag{2.18}$$

$$\int_{-\pi}^{\pi} e^{i(u\cos(\tau)+v\sin(\tau))} \qquad \sin(k\tau)d\tau = 2\pi i^k\sin(k\theta)J_k(r), \tag{2.19}$$

where k is an integer and $J_k(r)$ is the Bessel function of the first kind. On proceeding this way, we are left with two equations in terms of the amplitude r and the phase θ,

$$\begin{aligned}\omega\dot{r} &= -\left(\delta\omega\frac{r}{2} + \frac{1}{2}(\gamma\sin(2\theta) + \beta\cos(2\theta))\left(J_1(r) + J_3(r)\right)\right),\\ r\omega\dot{\theta} &= -\left(-\omega_\phi^2 J_1(r) + \omega^2\frac{r}{2} + \frac{1}{2}(\gamma\cos(2\theta) - \beta\sin(2\theta))\left(J_1(r) - J_3(r)\right)\right).\end{aligned} \tag{2.20}$$

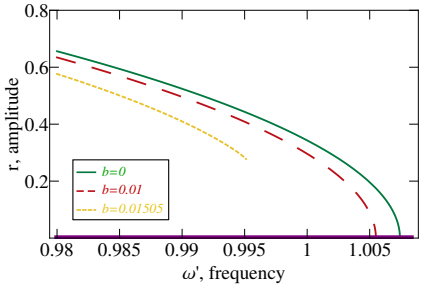

Figure 2.2: Frequency response of the SQUID for dimensionless driving force $c = 0.03$ and different values of SQUID dissipation b. The purple horizontal line represents the zero solution. Here, only stable equilibria are shown.

The equilibrium points of the slow flow are determined by setting $\dot{r}$ and $\dot{\theta}$ to zero, giving

$$\gamma \sin(2\theta) + \beta \cos(2\theta) = -\frac{\delta \omega r}{J_1(r) + J_3(r)}, \tag{2.21}$$

$$\gamma \cos(2\theta) - \beta \sin(2\theta) = -\frac{\omega^2 r - 2\omega_\phi^2 J_1(r)}{J_1(r) - J_3(r)}. \tag{2.22}$$

By taking the square and then summing Eqs. (2.21) and (2.22) one gets the algebraic equation for the amplitude only,

$$\frac{(r\omega'^2 - 2J_1(r))^2}{(J_1(r) - J_3(r))^2} + \frac{\left(br\omega'\right)^2}{(J_1(r) + J_3(r))^2} = \frac{(\gamma^2 + \beta^2)}{4\omega_\phi^4}, \tag{2.23}$$

where $\omega' = \omega/\omega_\phi$ and $b = \delta/\omega_\phi$.

We are interested in stable solutions of Eq. (2.23) and, therefore, we need to perform the stability analysis [28]. It is done by varying the amplitude and the phase of the out-of-equilibrium solution (r_0, θ_0) obtained from Eqs. (2.21) and (2.22),

$$r = r_0 + \Delta r \quad \text{and} \quad \theta = \theta_0 + \Delta\theta, \tag{2.24}$$

where Δr and $\Delta\theta$ are small deviations. Substituting (2.24) into (2.20) and linearizing in Δr and $\Delta\theta$, we obtain the constant coefficient system,

$$\begin{pmatrix} \Delta\dot{r} \\ \Delta\dot{\theta} \end{pmatrix} = \begin{pmatrix} e(r_0) & f(r_0) \\ g(r_0) & h(r_0) \end{pmatrix} \begin{pmatrix} \Delta r \\ \Delta\theta \end{pmatrix} = \mathbf{M} \begin{pmatrix} \Delta r \\ \Delta\theta \end{pmatrix}. \tag{2.25}$$

We seek the following solutions to the linear system: $\Delta r = Ae^{\lambda t}$ and $\Delta\theta = De^{\lambda t}$. The solutions should be bound as t goes to infinity, meaning the eigenvalues λ of $\mathbf{M}$ should be negative. We impose the conditions on the trace of the associated matrix $\mathbf{M}$, $tr = e(r_0) + h(r_0) \leq 0$, and on its determinant, $det = e(r_0)h(r_0) - f(r_0)g(r_0) > 0$. From these conditions the stability testing of the solutions is straightforward.

Equation (2.23) is the equation for the amplitude r if the backaction is not taken into account. The equation is valid for any values of r. Analytical solutions can be obtained,

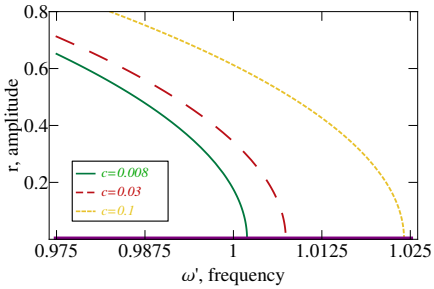

Figure 2.3: The dependence of the amplitude on the frequency for fixed dissipation $b = 0.001$ and driving forces $c = 0.008, 0.03, 0.1$.

however, only for small values of r. The denominators on the left-hand side of Eq. (2.23) can be safely ignored because the dissipation and quantity $\omega'^2 - 1$ are small as long as the backaction is not included. Their inclusion does not change the result (they will be taken into account in the next section for evaluating the effect of backaction). The Bessel function in the numerator of Eq. (2.23) is instead approximated up to the third order in the amplitude, $J_1(r) \approx \frac{r}{2} - \frac{r^3}{16}$. We focus on the special case when the mechanical oscillator is in the resonance $\omega_d \sim \omega_m$. Then, introducing the dimensionless driving force, $c = (\xi \tan(\phi_b) F_d)/(2m_r \omega_\phi \omega_{pl} \Gamma_m)$, and since $\gamma = 0$, we obtain the amplitudes of the two stable solutions,

$$r_0 = 2\sqrt{2 - 2\omega'^2 + \frac{\sqrt{c^2 - 4b^2\omega'^4}}{\omega'}} \quad \text{and} \quad r_0 = 0. \tag{2.26}$$

The amplitude for different values of dissipation is shown in Fig. 2.2. Note first that at negligible dissipation and driving there is a bifurcation point $\omega_d = 2\omega_c$, which depends on the cavity frequency $\omega_c = \omega_{pl}\sqrt{\cos(\phi_b)}$. Above this point, $r = 0$ is the only stable solution; below this point, a non-trivial solution emerges. This behavior is typical and has been experimentally observed for the parametrically driven oscillator [25]. The bistability below the bifurcation points must result in the hysteretic behavior. If the frequency is slowly increasing, the amplitude remains zero, then "jumps up" to the upper branch and follows it down. If the frequency is sweeping backward, the amplitude follows the upper branch to some point and then drops to the lower branch. To complete the picture, we also plot the amplitude for different values of the driving/coupling (as parametrized by the parameter c). This is shown in Fig. 2.3.

Both the finite dissipation and the finite driving push the bifurcation point to higher frequencies. However, when the dissipation is too strong, $\omega' > \sqrt{c/(2b)}$, the non-trivial solution does not appear. This condition is frequency dependent, and therefore at the finite dissipation and weak driving, the non-trivial solution does not exist close to the bifurcation point but reappears at lower frequencies. Note that our analytical analysis is restricted to $r \ll 1$; therefore, for strong enough dissipation, the non-trivial solution does not appear at any frequency.

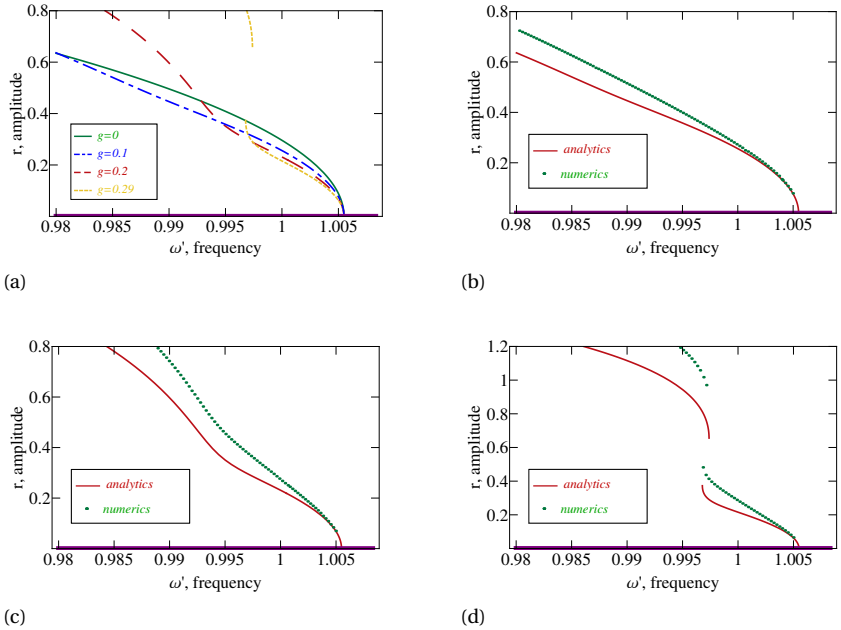

Figure 2.4: (a) The dimensionless amplitude r of the dc SQUID overall phase is plotted *vs.* the frequency ratio ω' for different coupling strength g, which induces backaction. The values of dissipation are set to $b = 0.01$ and the renormalized force is $c = 0.03$. (b)–(d) Analytical amplitude results (solid line) compared with numerical simulations (dotted line) for corresponding backaction strength (b) $g = 0.1$, (c) $g = 0.2$, and (d) $g = 0.29$. Purple line shows the zero-amplitude solution.

2.4. BACKACTION

In Sec. 2.3, we investigated the situation when backaction of the SQUID on the resonator is negligible. In this section, we take this backaction perturbatively into account and demonstrate that it leads to further multistability of the SQUID. One can take into account the second term of Eq. (2.7) by inserting solutions from Sec. 2.3

$$\varphi_+ = r\cos(\theta)\cos(\omega_d t/2) - r\sin(\theta)\sin(\omega_d t/2). \tag{2.27}$$

In this way, we perturbatively study the effect of backaction on the amplitude of the SQUID.

We can eliminate the phase dependence using Eqs. (2.21) by $\cos(2\theta) = -b\omega'^2 r/c(J_1 + J_3)$ and then expanding $\cos(\varphi_+)$ in term of the Bessel functions using the identities

$$\cos\left(p\cos(\frac{\omega_d t}{2})\right)\cos\left(m\sin(\frac{\omega_d t}{2})\right) =$$
$$2\sum_{i=0}^{\infty}(-1)^i\left[J_{2i}(p)J_{2i+2}(m) - J_{2i+2}(p)J_{2i}(m)\right]\cos(\omega_d t)$$

and

$$\sin\left(p\cos(\frac{\omega_d t}{2})\right)\sin\left(m\sin(\frac{\omega_d t}{2})\right) = 2\sum_{i=0}^{\infty}(-1)^i\left[J_{2i+1}(p)J_{2i+3}(m) - J_{2i+3}(p)J_{2i+1}(m)\right]\sin(\omega_d t) + 2J_1(p)J_1(m)\sin(\omega_d t), \tag{2.28}$$

where $p = r\cos(\theta)$ and $m = r\sin(\theta)$. Other harmonics of the overall phase which have the frequencies $\omega = n\omega_d/(2\omega_{pl})$, where n is an integer, are disregarded in the expansions. They generate the Bessel functions of higher orders, which are small for the amplitudes of our interest, $r \ll 1$.

To provide an analytical solution, we again look at small amplitudes. In this case, the two cosines of Eq. (2.28) can be approximated by $(m^2 - p^2)\cos(\omega_d t)/4$, and the two sines give $pm\sin(\omega_d t)/2$. Then, we see that the driving force is shifted due to the backaction

$$F_d \to F' = F_d - \frac{E_J\xi\sin(\phi_b)}{c}\frac{b\omega'^2}{1-\frac{r^2}{12}}r^2\,, \tag{2.29}$$

and the additional sinusoidal force is generated

$$G = -\frac{E_J\xi\sin(\phi_b)r^2}{c}\sqrt{\frac{1}{4}c^2 - \frac{b^2\omega'^4}{(1-\frac{r^2}{12})^2}}. \tag{2.30}$$

Hence, the equation for the resonator becomes

$$\ddot{x} + \Gamma_m\dot{x} + \omega_m^2 x = \frac{F'}{m_r}\cos(\omega_d t) + \frac{G}{m_r}\sin(\omega_d t). \tag{2.31}$$

This equation has the same solutions as the driven harmonic oscillator given in Eq. (2.9) with the modified amplitudes,

$$A \to A' = -\frac{G}{m_r\Gamma_m\omega_d} \quad \text{and} \quad D \to D' = \frac{F'}{m_r\Gamma_m\omega_d}. \tag{2.32}$$

The shift in the oscillator's amplitudes affects the quantities γ and β in the equation of motion for the SQUID. It follows that the backaction is included for the amplitude of the SQUID through the quantity

$$\frac{\gamma^2+\beta^2}{\omega_\phi^4} = \left(\frac{\xi\tan(\phi_b)}{2m_r\Gamma_m\omega_\phi\omega_{pl}\omega'}\right)^2\left(F'^2+G^2\right). \tag{2.33}$$

The equation for the amplitude becomes

$$\frac{(\omega'^2 - 1 + \frac{r^2}{8})^2}{\left(\frac{1}{2}-\frac{r^2}{12}\right)^2} + \frac{\left(b\omega'\right)^2}{\left(\frac{1}{2}-\frac{r^2}{24}\right)^2} = \frac{c^2+g^2r^4}{\omega'^2} - \frac{4gbr^2}{1-\frac{r^2}{12}} \tag{2.34}$$

where $g = E_J\xi^2 \tan(\phi_b)\sin(\phi_b)/(4m_r\omega_\phi\omega_{pl}\Gamma_m)$ is the strength of the backaction. Note that this is still an algebraic equation though more sophisticated than the expansion of Eq. (2.23).

Figure 2.4(a) displays the stable non-trivial solution for the phase oscillation amplitude r to Eq. (2.34) as a function of the frequency ω' for different values g of backaction and for the finite dissipation $b = 0.01$. One can see that there is still a bifurcation point, and its position is not affected by the backaction. The effect of the backaction is to suppress the amplitude close to the bifurcation point. However, further from this point, the amplitude r enhances. As the backaction gets stronger, it changes the monotonous behavior of the amplitude. In the certain range of frequencies, the non-trivial solution becomes multi-stable: at the same frequency, there might be two stable non-trivial solutions in addition to the trivial solution $r = 0$.

Note, however, that our analytical treatment, based on the quartic expansion of the cosine potential (the Duffing model), is only valid for $r \ll 1$. The non-trivial features that we observe appear at $r \sim 0.5$ and are, strictly speaking, outside the range of applicability of our approximation. To check whether they really exist, we perform the numerical analysis of the full Hamiltonian of the system, still assuming weak backaction ($g \ll 1$), but without expanding the cosine. We solve numerically the system of Eqs. (2.9) and (2.8). The solution is valid for any values of the amplitude r. The results are presented in Figs. 2.4(b)–2.4(d). We take the initial conditions for solving the differential equations to be our analytical solutions. The time evolved from 0 to 20000 and, after it reached the steady-state, we measured the amplitude. For small enough amplitudes, the analytical results coincide with the numerical ones. For higher amplitudes, there is certain deviation; however, the pattern stays the same. In particular, the numerical solution confirms the multistability.

2.5. CONCLUSIONS

In this chapter, we considered a SQUID coupled to a driven linear mechanical resonator. We found that above the bifurcation point, the phase of the SQUID does not respond to the parametric driving. The bifurcation point is located at the frequency slightly above the point where the condition $\omega_d = 2\omega_c$ is met. The precise location of the bifurcation point depends on the dissipation and the driving force, but not on the backaction strength. Below the bifurcation point, a non-trivial solution for the amplitude of the SQUID oscillation arises. We found that the dissipation suppresses this non-trivial solution whereas the driving strength enhances it. Furthermore, we discover that at strong enough backaction, the non-trivial solution may become multistable, and thus the physics of the systems goes beyond the Duffing oscillator. We have obtained the multistability by analytical calculations within the Duffing oscillator approximation and also by numerical solution of the full model.

One can experimentally control the strength of the backaction by changing the geometry of the resonator or parameters of the SQUID. In our model, the magnetic field was applied perpendicular to the SQUID loop; instead one can use parallel orientation of the magnetic field and tune flux Φ_{ext} using, *e.g.*, a stripline, which also changes the backaction strength.

Currently, the most stringent condition in our theory which hinders the experimen-

tal verification is that the frequencies of the SQUID and the mechanical resonator are of the same order. In the existing experiments [13, 14, 20], the plasma frequency of the SQUID was several orders of magnitude higher than the mechanical frequency. However, currently there is an interest to the fabrication of superconducting junctions with suspended carbon nanotubes [29] and graphene sheet integrated into the microwave cavities [30]. Whereas the frequency of mechanical motion in the existing devices is still lower than the cavity frequency, the regime $\omega_d \sim 2\omega_c$ can be achieved. Another limitation is that we assumed the two Josephson junctions to be identical. We do not expect, however, that the asymmetry of the SQUID would qualitatively affect our results.

Finally, we emphasize that we have only made the first step towards exploring nonlinear cavity properties in cavity electrodynamics. We certainly expect more rich and interesting physics in the situations which lie outside the scope of this chapter — strong backaction (beyond the perturbation theory), dispersive coupling between the SQUID and the resonator, as well as quantum effects in both the phase of the SQUID and the mechanical motion of the resonator.

REFERENCES

[1] A. N. Cleland,*Foundantions of Nanomechanics* (Springer-Verlag, New York, 2003).

[2] M. Poot and H. S. J. van der Zant, Phys. Rep. **511**(5), 273 (2012).

[3] M. Aspelmeyer, T. J. Kippenberg, and F. Marquardt, Rev. Mod. Phys **86**, 1391 (2014).

[4] A. D. O'Connell, M. Hofheinz, M. Ansmann, R. C. Bialczak, M. Lenander, E. Lucero, M. Neeley, D. Sank, H. Wang, M. Weides, J. Wenner, J. M. Martinis, and A. N. Cleland, Nature (London) **464**, 697 (2010).

[5] J. D. Teufel, T. Donner, Dale Li, J. W. Harlow, M. S. Allman, K. Cicak, A. J. Sirois, J. D. Whittaker, K. W. Lehnert, and R. W. Simmonds, Nature (London) **475**, 359 (2011).

[6] J. Chan, T. P. Mayer Alegre, A. H. Safavi-Naeini, J. T. Hill, A. Krause, S. Gröblacher, M. Aspelmeyer, and O. Painter, Nature (London) **478**, 89 (2011).

[7] A. H. Safavi-Naeini, J. Chan, J. T. Hill, Thiago P. Mayer Alegre, A. Krause, and O. Painter, Phys. Rev. Lett. **108**, 033602 (2012).

[8] T. A. Palomaki, J. D. Teufel, R. W. Simmonds, K. W. Lehnert, Science **342**, 710 (2013).

[9] D. Rugar and P. Grütter , Phys. Rev. Lett. **67**, 699 (1991).

[10] C. H. Metzger and K. Karrai , Nature (London) **432**, 1002 (2004).

[11] H. B. Meerwaldt, G. Labadze, B. H. Schneider, A. Taspinar, Ya. M. Blanter, H. S. J. van der Zant, and G. A. Steele, Phys. Rev. B **86**, 115454 (2012).

[12] D. R. Koenig and E. M. Weig, Appl. Phys. Lett. **101**, 213111 (2012).

[13] M. Poot, S. Etaki, I. Mahboob, K. Onomitsu, H. Yamaguchi, Ya. M. Blanter, and H. S. J. van der Zant, Phys. Rev. Lett. **105**, 207203 (2010).

[14] S. Etaki, F. Konschelle, Ya. M. Blanter, H. Yamaguchi, and H. S. J. van der Zant, Nat. Commun. **4**, 1803 (2013).

[15] X. Zhou and A. Mizel, Phys. Rev. Lett. **97**, 267201 (2006).

[16] E. Buks and M. P. Blencowe, Phys. Rev. B **74**, 174504 (2006).

[17] F. Xue, Y.-X. Liu, C. P. Sun and F. Nori, Phys. Rev. B **76**, 064305 (2007).

[18] S. Pugnetti, Y. M. Blanter and R. Fazio, Europhys. Lett. **90**, 48007 (2010).

[19] G. Z. Cohen and M. Di Ventra, Phys. Rev. B **87**, 014513 (2013).

[20] S. Etaki, M. Poot, I. Mahboob, K. Onomitsu, H. Yamaguchi and H. S. J. van der Zant, Nat. Phys. **4**, 785 (2008).

[21] R. Vijay, M. H. Devoret, and I. Siddiqi, Rev. Sci. Instrum **80**, 111101 (2009).

[22] M. Muck and R. McDermott, Supercond. Sci. Technol. **23**, 093001 (2010).

[23] R. Lifshitz and M. C. Cross, Phys. Rev. B **67**, 134302 (2003).

[24] G. Litak, G. Spuz-Szpos, K. Szabelski, and J. Warminski, Int. J. Bifurcation and Chaos **9**, 493 (1999).

[25] M.-F. Yu, G. J. Wagner, R. S. Ruoff, and M. J. Dyer, Phys. Rev. B **66**, 073406 (2002).

[26] P. J. Holmes and D. A. Rand, J. Sound Vibration **44**, 237 (1976).

[27] G. N. Watson, *A Treatise on the Theory of Bessel Functions*, (Cambridge University Press, Cambridge, 1922).

[28] M. W. Hirsch, S. Smale and R.L. Devaney, *Differential Equations, Dynamical Systems and an Introduction to Chaos*, (Elsevier, New York, 2004).

[29] B. H. Schneider, S. Etaki, H. S. J. van der Zant and G. A. Steele, Sci. Rep. **2**, 599 (2012).

[30] V. Singh, S. J. Bosman, B. H. Schneider, Y. M. Blanter, A. Castellanos-Gomez, and G. A. Steele, Nat. Nanotech. **9**, 820 (2014).

3

FLUX-MEDIATED OPTOMECHANICS

O. Shevchuk, G. A. Steele, and Ya. M. Blanter

We investigate superconducting interference device (SQUID) with two asymmetric Josephson junctions coupled to a mechanical resonator embedded in the loop of the SQUID. We quantize this system in the case when the frequency of the mechanical resonator is much lower than the cavity frequency of the SQUID and in the case when they are comparable. In the first case, the radiation pressure and cross-Kerr type interactions arise and are modified by asymmetry. Cross-Kerr type coupling is the leading term at the extremum points where radiation pressure is zero. In the second case, the main interaction is single-photon beam splitter, which exists only at finite asymmetry. Another interaction in this regime is of cross-Kerr type, which exists at all asymmetries, but generally much weaker than the beam splitter interaction. Increasing magnetic field can substantially enhance optomechanical couplings strength with the potential for the radiation pressure coupling to reach the single-photon strong coupling regime, even the ultrastrong coupling regime, in which the single-photon coupling rate exceeds the mechanical frequency.

3.1. INTRODUCTION

The progress in optomechanical systems, where an optical or microwave cavity is coupled to a mechanical resonator, was impressive in recent years [1]. The accomplishments in optomechanics include cooling mechanical resonator to its quantum ground state[2, 3], prediction [4] and observation [5] of the optomechanically-induced transparency, squeezing of the cavity[6, 7], and mechanical [8–10] modes, and coherent state transfer [11, 12]. Many of these experiments have been realized using superconducting circuits, which enables to consider microwave cavities coupled to mechanical motion as possible building blocks for quantum information processing [13].

The coupling between cavity and mechanical resonator plays a central role in optomechanics. In the published experiments, intrinsically weak radiation pressure coupling was amplified by increasing drive power of the cavity, which linearizes the effective optomechanical interaction of the system. Such linear interaction, for example, turns Gaussian states of the cavity and mechanical resonator into Gaussian states. In order to create more general states for quantum information applications and to achieve, for instance, negative Wigner function one needs to use either single-photon sources and photodetectors [14] or non-linear effects, of which non-linear optomechanical interaction is the most common one. Therefore, having strong single-photon radiation pressure coupling of the order or larger than the cavity decay rate is desirable as well as having strong coupling of the cavity to the position squared of the mechanical resonator [15]. If the single-photon radiation pressure coupling can be made of the order of the mechanical frequency and larger than the cavity decay rate, the the system is in the ultra-strong coupling regime and photon blockade can be observed [16].

Along with the ultracold atoms [17], superconducting circuits are promising candidates to reach ultrastrong coupling. Recently, the idea of using Josephson effect to enhance optomechanical couplings has been researched theoretically [18–20] and experimentally [21]. Many of those proposals involve using superconducting quantum interference device (SQUID) with two Josephson junctions, which makes cavity intrinsically nonlinear due to the Josephson effect. SQUID is either embedded into the resonator itself or SQUID with embedded mechanical resonator is incorporated into a microwave cavity.

In this Chapter, we consider a SQUID with two symmetric or asymmetric Josephson junctions and an embedded mechanical resonator and show that it by itself can produce ultrastrong optomechanical coupling. Originally, a dc SQUID with embedded mechanical oscillator was studied as a sensitive displacement detector [22–26], however, the asymmetry of the junsctions so far was not at the focus of attention, and theoretical proposals are routinely assuming that two junctions of the SQUID are almost identical. A certain asymmetry is always present in the experiment, and we show that it affects the coupling strength. In addition, we express the couplings in such SQUID devices in the language of optomechanics, perform numerical simulations of the coupling rates for realistic experimental geometries. Doing so we find that this platform has the potential to reach both the single-photon strong coupling, a regime of strong quadratic coupling of the motion to the cavity, and potentially the ultrastrong coupling regime where the single-photon coupling rate exceeds the mechanical frequency.

In the first part of this Chapter, we investigate in details the effect of asymmetry in

the SQUID with two junctions and embedded mechanical resonator. As a first step we look at the most common experimental case of the mechanical frequency being much smaller than the cavity frequency [27]. We quantize the asymmetric system to get radiation pressure interaction and cross-Kerr type interaction, where the cavity is coupled to the position squared of the mechanical resonator. We show that for experimentally feasible parameters radiation pressure coupling can reach single-photon strong coupling regime and for stronger magnetic fields the ultrastrong coupling regime. The cross-Kerr coupling is usually smaller than radiation pressure coupling but it is the leading coupling at the extremum points of the flux where the radiation pressure is zero. Such strong coupling would enable a quantum non-demolition measurement of a phonon number in the mechanical resonator [28] or the cavity's photon number.

As a second step, we study the case when the mechanical and cavity frequencies are of the same order. Since the SQUID cavity frequency is measuring in GHz, the same order would be required for the mechanical oscillator. Currently, carbon nanotube (CNT) resonator can reach GHz frequency [29] and, hence, the realizations of the SQUID with suspended CNT junctions [30, 31] could reach this regime. In this case, there are two leading interactions: cross-Kerr and single-photon beam splitter. The single-photon beam splitter exists only at the finite asymmetry. The radiation pressure term is oscillating too fast and is, therefore, disregarded. The beam splitter is used in many exrimental setups, and Hamiltonian with the beam splitter interaction is easily diagonalized and solved. When single-photon beam splitter is in the range of the strong coupling, one can observe *e.g.* optomechanical normal-mode splitting [1].

The remainder of the Chapter is organized as follows. In Sec. 3.2 we find current and cavity frequency of the SQUID with asymmetric Josephson junctions and an embedded mechanical resonator. In Sec. 3.3 we derive the effective Hamiltonian of this system for two cases. In the first case, the cavity frequency of the SQUID is taken to be much larger than the mechanical frequency, which results in the radiation pressure and cross-Kerr interactions. In the second case, the cavity frequency is considered to be of the order of the mechanical frequency providing single-photon beam splitter and cross-Kerr interactions. In Sec. 3.4 we draw the potential map and discuss optomechanical couplings. Finally, we conclude our results in Sec. 3.5.

3.2. CURRENT OF THE ASYMMETRIC SQUID

In this Section, we follow the standard textbook treatment of the current through an asymmetric SQUID. We consider two Josephson junctions with different values of critical current I_1^0 and I_2^0 connected in a loop together with an embedded mechanical resonator, as shown in Fig. 3.1(a). The energy scales for such SQUID are described by average Josephson energy $E_J = \hbar(I_1^0 + I_2^0)/4e$ and charging energy $E_c = (2e)^2/2C \ll E_J$ with the shunting capacitance of each junction C. The SQUID has a loop area A with the suspended arm of the length l. Oscillations of the mechanical resonator modulate the total flux of the SQUID loop. Then, the SQUID with the embedded mechanical resonator can be viewed as an LC circuit, in which the Josephson inductance of the SQUID L_J, which for symmetric junctions $I_1^0 = I_2^0 = I_0$ is well-known to be $\Phi_0/(4\pi I_0 \cos(\pi\Phi/\Phi_0))$, changes with the total flux Φ threading though the loop and, consequently, the mechanical resonator couples inductively to the SQUID, see Fig. 3.1(b). For simplicity, we assume that

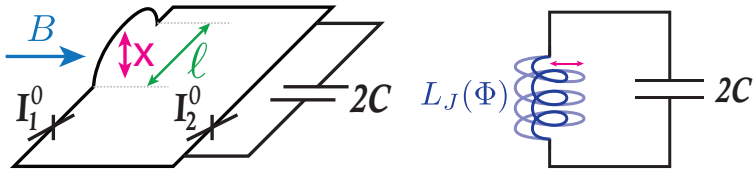

(a) (b)

Figure 3.1: (a) A schematic overview of the SQUID, which contains two Josephson junctions with different critical currents. The mechanical resonator is embedded into the SQUID loop. The magnetic field B is applied under certain angle to the loop, and the displacement of the mechanical resonator is x. (b) The mechanical resonator inductively couples to the SQUID via the total flux Φ.

mechanical resonator moves in its single mode. The dynamics of the mechanical resonator is described by the displacement x from the equilibrium position. The dynamics of the SQUID itself is described by the sum of the gauge-invariant phases across each junction (ϕ_1 and ϕ_2), $\varphi_+ = (\phi_1 + \phi_2)/2$, which is referred as the overall phase of the SQUID. Moreover, the difference of the phases is bound by the total flux threading the loop,

$$\varphi_- = (\phi_1 - \phi_2)/2 = \pi\Phi/\Phi_0 + \pi n\,, \tag{3.1}$$

where n is an integer and $\Phi_0 = h/2e$ is the flux quantum.

Assuming the magnetic field is applied under certain angle to the SQUID loop the total flux can be separated to two contributions. The first contribution is a bias flux Φ_b, which is added to the SQUID loop. The second contribution comes from a flux threading through the area described by the oscillations of mechanical resonator. Since it is more convenient to work with the phase difference rather than the flux itself we define renormalized bias flux $\phi_b = \pi\Phi_b/\Phi_0$ and renormalized flux shift provided by the resonator $\xi x = \pi\beta_0 B l x/\Phi_0$ with the average geometric constant β_0, which takes into account the direction of the magnetic field and the geometry of the mechanical resonator. Then, the phase difference is given by

$$\varphi_- = \phi_b + \xi x + \pi n. \tag{3.2}$$

Here, we study the situation when the circuit has a negligible self-inductance.

Now we write the total current going through the asymmetric SQUID. For this purpose we introdice the average critical current $I_0 = (I_1^0 + I_2^0)/2$. The critical currents of the first and the second junctions are defined as $I_1^0 = I_0(1-\alpha_I)$ and $I_1^0 = I_0(1+\alpha_I)$, respectively, with the asymmetry parameter α_I. Therefore, the total current I through both junctions is separated to two terms: one is the same as in the case of equal critical currents and another term, which is responsible for the influence of asymmetry,

$$I = I_1^0\sin(\phi_1) + I_2^0\sin(\phi_2) = 2I_0\cos(\varphi_-)\sin(\varphi_+) - 2I_0\alpha_I\cos(\varphi_+)\sin(\varphi_-). \tag{3.3}$$

In order to find a critical current of the asymmetric SQUID, we shift the position of the overall phase of the SQUID by the phase φ_0 which satisfies the relation: $\tan(\varphi_0) =$

$\alpha_I \tan(\varphi_-)$. Then, the total current is simplified to the following

$$I = 2I_0 S(\varphi_-) \sin(\varphi_+ - \varphi_0), \tag{3.4}$$

where $S(\varphi_-) = \sqrt{\cos^2(\varphi_-) + \alpha_I^2 \sin^2(\varphi_-)}$ is a flux dependent function, which turns to cosine at zero asymmetry, and the total current becomes the well-known current of the symmetric SQUID. Then, when mechanical resonator is at rest, we can define the maximum current and, hence, the critical current of the asymmetric SQUID as well as the cavity frequency

$$I(x=0) = I_c = 2I_0 S(0) \quad \text{and} \quad \omega_c(0) = \sqrt{\frac{2\pi I_c}{C\Phi_0}}. \tag{3.5}$$

Here we use $S(0)$, which is the function of ϕ_b instead of φ_- at zero displacement.

In Fig. 3.2(a) we show the behavior of the critical current for symmetric and 50% asymmetry cases. For the identical junctions the current changes from 0 to $2I_0$, but in the presence of the asymmetry the current never reaches zero value. Even at half flux quantum when the critical current for the symmetric case is zero, the critical current of the asymmetric SQUID is at minimum $I_c(\phi_b = \pi/2) = 2I_0\alpha_I$. Nevertheless, the maximum, which happens at the odd integer flux quantum, is not affected by the asymmetry. The cavity frequency is proportional to $\sqrt{I_c}$ and portrays the same behavior of the critical current as shown in Fig. 3.2(b). For parameters of the critical current of the Josephson junction I_0 = 500 nA and capacitance C = 30 pF the maximum cavity frequency is 10 GHz. At half flux quantum and 50% asymmetry, the cavity frequency reaches its minimum of 4.5 GHz.

3.3. QUANTIZATION

In the following, we quantize the system by starting with the classical Hamiltonian, which consists of the simple harmonic oscillator, kinetic energy and the potential energy of the SQUID,

$$H = \frac{m_r \dot{x}^2}{2} + \frac{m_r \omega_m^2 x^2}{2} + \frac{C\Phi_0^2}{2(2\pi)^2}\dot{\varphi}_+^2 + E(\varphi_+, x), \tag{3.6}$$

where m_r and ω_m are the mass and frequency of the mechanical resonator. The potential energy of the SQUID E is derived from the total current $\Phi_0 I/2\pi = \partial E/\partial\varphi_+$ found in Sec. 3.2,

$$E(\varphi_+, x) = -2E_J S(\varphi_-) \cos\left[\varphi_+ - \arctan(\alpha_I |\tan\varphi_-|)\right]. \tag{3.7}$$

The minimum of the potential is shifted by the flux dependent parameter, which also depends on the displacement of the mechanical resonator. Depending on the difference between the cavity frequency and the mechanical frequency one can assume quasi-static regime or has to take into account the displacement dependent shift.

3.3.1. DISPERSIVE REGIME

In the typical case when the mechanical frequency is much smaller than cavity frequency, the shift by the flux can be assumed static on the timescales related to the SQUID. Then,

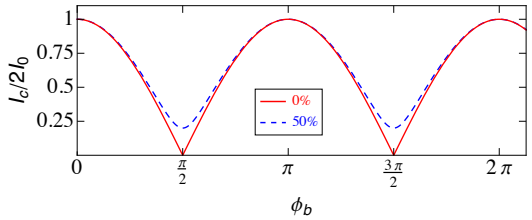

(a)

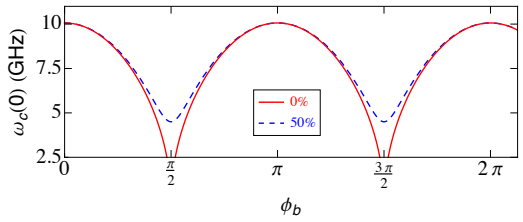

(b)

Figure 3.2: (a) The critical current and (b) cavity frequency are plotted as a function of renormalized bias flux of the symmetric and asymmetric SQUID. The cavity frequency of the symmetric SQUID is cut at realistic value of 2.5 GHz.

we can write potential energy in terms of the shifted phase, $\varphi = \varphi_+ - \arctan(\alpha_I |\tan(\phi_b)|)$. The kinetic energy of the SQUID is not affected by the constant shift, and thus the phase φ_+ can be replaced by φ.

In order to quantize the phase and the position, the potential energy is expanded in terms of the phase up to the second order. This means that we consider SQUID as a linear harmonic oscillator with the single-photon Kerr shift smaller than the linewidth of the cavity and the cavity frequency. The term, which is independent of the phase, shifts the equilibrium position of the mechanical resonator and modifies the mechanical frequency

$$\omega_m' = \sqrt{\omega_m^2 + \frac{4E_J\xi^2(1-\alpha_I^2)(\cos^4(\phi_b) - \alpha_I^2\sin^4(\phi_b))}{m_r S(0)^3}}. \tag{3.8}$$

For the phase dependent terms we introduce creation and annihilation operators

$$\begin{pmatrix} a^\dagger \\ a \end{pmatrix} = \frac{1}{\sqrt{2\hbar m_\varphi \omega_c}} \left(m_\varphi \omega_c \varphi \mp i p_\varphi\right). \tag{3.9}$$

with the momentum coordinate $p_\varphi = C\Phi_0^2/(2\pi)^2\dot{\varphi} \equiv m_\varphi\dot{\varphi}$, where m_φ is the mass of the phase, and the displacement dependent cavity frequency is

$$\omega_c(\varphi_-) = \sqrt{\frac{4\pi I_0 S(\varphi_-)}{C\Phi_0}}. \tag{3.10}$$

This expression can also be retrieved from Eq. (3.5) for the mechanical resonator at rest by changing ϕ_b to φ_-. Therefore, the displacement dependent cavity frequency as a function of φ_- has the same behavior as shown in Fig. 3.2(c).

Now our Hamiltonian has a similar form to that of the Hamiltonian with symmetric Josephson junctions except for the modified cavity frequency,

$$H = \frac{m_r \dot{x}^2}{2} + \frac{m_r \omega_m^2 x^2}{2} + \hbar\omega_c(\varphi_-)\, a^\dagger a. \tag{3.11}$$

The position of the mechanical resonator is quantized by introducing the position operator, which is $x = x_{\mathrm{ZPF}}(b^\dagger + b)$, where b and $b^\dagger$ are creation and annihilation operators and $x_{\mathrm{ZPF}} = \sqrt{\hbar/2m_r\omega_m}$ is the amplitude of zero point fluctuations of the displacement x. Then, the uncoupled Hamiltonian of the mechanical resonator is $\hbar\omega_m b^\dagger b$.

The interaction terms are obtained by expanding the displacement dependent cavity frequency to the second order in displacement. Then, the interaction Hamiltonian after applying the rotation-wave approximation becomes

$$H_{int} = \hbar g_{RP}^1 a^\dagger a(b^\dagger + b) + \hbar g_Q^2 a^\dagger a b^\dagger b, \tag{3.12}$$

where the radiation pressure coupling and cross-Kerr coupling between cavity and mechanical resonator are, respectively,

$$g_{RP}^1 = x_{ZPF}\frac{\partial\omega_c}{\partial x}\Big|_{x=0} = x_{ZPF}\xi\frac{\partial\omega_c}{\partial\varphi_-}\Big|_{x=0} = x_{ZPF}\frac{(1-\alpha_I^2)\xi\sin(2\phi_b)\omega_c(0)}{4S(0)^2}, \tag{3.13}$$

$$g_Q^2 = x_{ZPF}^2\frac{\partial^2\omega_c}{\partial x^2}\Big|_{x=0} = x_{ZPF}^2\xi^2\frac{\partial^2\omega_c}{\partial\varphi_-^2}\Big|_{x=0} = 2x_{ZPF}\xi g_{RP}^1\cot(2\phi_b) - \frac{3(g_{RP}^1)^2}{\omega_c(0)}. \tag{3.14}$$

Note even when $g_{RP}^1 = 0$, the first term in Eq. (3.14) stays finite because $\sin(2\phi_b)$ in the radiation pressure coupling is multiplied with the infinite factor $\cot(2\phi_b)$.

In order to visualize the resulting couplings, to the chosen capacitance C and critical current I_0 we add following set of parameters: $\omega_m' = 10$ MHz, $A = 200\ \mu\mathrm{m} \times 150\ \mu\mathrm{m}$, $l = 150\ \mu$m, and $m_r = 200$ pg. The flux bias varies from $\phi_b = 2\pi n$ to $\phi_b = 2\pi n + \pi$, where $n = 72534$ corresponds to chosen value of magnetic field.

In Fig. 3.3(a), we plot the radiation pressure coupling. For the perfectly symmetric Josephson junctions, the absolute value of the radiation pressure infinitely increases while getting closer to the half-integer flux quantum. It suggests that if in the experiment one can tune bias flux very close to half flux quantum the radiation pressure will be maximum. However, because of the asymmetry of the SQUID the maximum of the radiation pressure coupling shifts to the value of the flux given be

$$\tan(\phi_b) = \pm\sqrt{1-\alpha_I^2 + \sqrt{1+14\alpha_I^2+\alpha_I^4}}/2\alpha_I. \tag{3.15}$$

Behind this value, the radiation pressure monotonically decreases to zero at the half-integer flux quantum. The maximum of the radiation pressure even at 50% asymmetry and magnetic field of 10 mT can reach single-photon strong coupling regime, considering a typical cavity decay rate of 80 kHz.

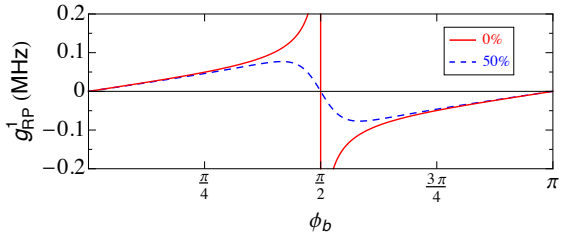

(a)

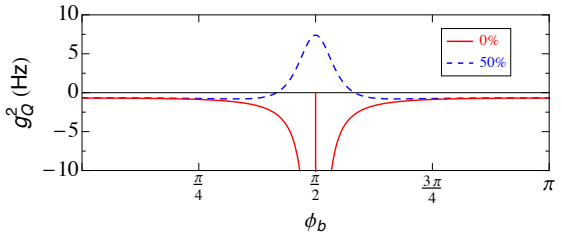

(b)

Figure 3.3: Light-matter couplings of symmetric and asymmetric SQUID for magnetic field B = 10 mT: (a) radiation pressure, (b) cross-Kerr coupling. The maximum of radiation pressure for 50% asymmetry is $g^1_{RP} = 77$ kHz.The flux bias is shifted by $\pi BA/\Phi_0 = 2\pi 72534$.

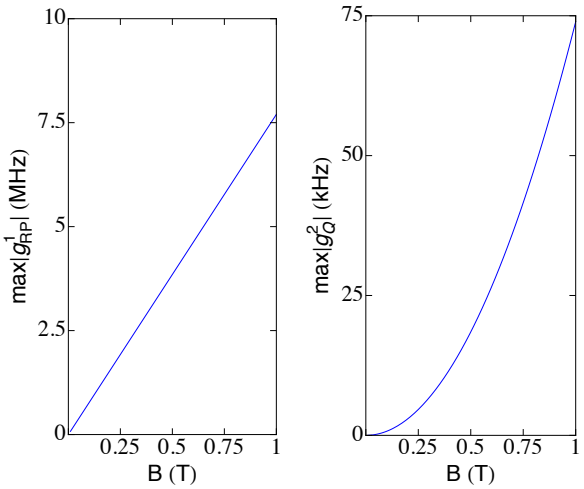

(a) (b)

Figure 3.4: The maximum of the (a) radiation pressure and (b) cross-Kerr coupling as a function of the magnetic field at 50% asymmetry. The flux bias is fixed and corresponds to the sweat spot of each coupling.

Since the radiation pressure can also be written in terms of the cavity frequency derivative, we can analyze this coupling looking at Fig. 3.2(a) by changing ϕ_b to φ_- as mentioned above. For the asymmetric case the slope of the frequency increases and then decreases while changing flux from 0 to $\pi/2$. After crossing $\pi/2$ to π it changes sign of the slope, which leads to the negative radiation pressure. Also, for the asymmetric junctions the slope at integer and half integer flux quantum is zero.

The cross-Kerr coupling is shown in Fig. 3.3(b). The coupling g_Q^2 is overall much weaker than radiation pressure except for the odd integer flux quantum, where g_{RP}^1 is zero and g_Q^2 is the leading term. For the symmetric case the coupling is infinitely strong approaching half-integer flux quantum, which is the same behavior found for the radiation pressure, but in contrast to the latter it does not change the sign while crossing $\pi/2$. Looking at the Fig. 3.2(b) we expect that for the asymmetric SQUID the cross-Kerr coupling, which is the second derivative of frequency, changes the sign between 0 to $\pi/2$ and then from $\pi/2$ to π and this is indeed the result observed here. The maximum of the coupling for the asymmetric case is achieved at the half-integer flux quantum. We can also notice that even at integer flux quantum the value of the cross-Kerr coupling (for the chosen parameters) is 0.66 Hz. In the experiment with the membrane inside the cavity [15] the value of the second derivative of the cavity frequency was $\omega_c''(x)/2\pi = 108$ kHz nm^{-2}. Then in order to improve this value multiple modes of the cavity were coupled to the single mode of the mechanical resonator [32] to get $\omega_c''(x)/2\pi = 8.7$ MHz nm^{-2}, which is still smaller than our calculated value at integer flux quantum, which is $\omega_c''(x)/2\pi = 4$ GHz nm^{-2}.

The maximum of the asymmetric couplings increases with magnetic field, which is captured in Fig. 3.4. Increasing magnetic field to 1 T is experimentally feasible [31] and increases chances of getting higher couplings. The radiation pressure coupling is linearly dependent on B and the cross-Kerr coupling is quadratically dependent on B. At 50% asymmetry and magnetic field of 1 T the radiation pressure can reach an ulrastrong coupling regime ($g_{RP}^1 \sim \omega_m$), which also mean that at lower asymmetry the value on the sweat spot can even be greater. The cross-Kerr coupling can reach values of 80kHz. It can be stronger for the lower asymmetry, but the window to catch sweat spot becomes more narrow for the lower asymmetry.

3.3.2. RESONANT FREQUENCIES

In the case of the resonant cavity frequency and mechanical frequency, the minimum of the potential is shifted by the position dependent parameter. However, the displacement is now one of the dynamical variables of the system, separate from the overall phase. If we shift the phase by the displacement dependent parameter then the kinetic energy acquires the shifted phase as well as extra terms in the form of $\dot{\varphi}_+ \dot{x}$ with the original phase. Therefore, it is simpler to expand the arctangent in the potential energy to the first order in x, which is sufficient since the amplitude of the mechanical resonator is usually small in such devices. The expanded potential energy depends on both the displacement

and the phase φ, which do not combine in a single variable,

$$E(\varphi,x) = -2E_J S(\varphi_-)\cos\left(\frac{\alpha_I\xi}{S(0)^2}x\right) - 2E_J S(\varphi_-)\sin\left(\frac{\alpha_I\xi}{S(0)^2}x\right)\varphi + E_J S(\varphi_-)\cos\left(\frac{\alpha_I\xi}{S(0)^2}x\right)\varphi^2. \tag{3.16}$$

Similarly to the previous case, the first term shifts the equilibrium position of the mechanical resonator and the mechanical frequency,

$$\omega_m' = \sqrt{\omega_m^2 + \frac{2E_J\xi^2\sqrt{2(1+\alpha_I^2+(1-\alpha_I^2)\cos(2\phi_b))}}{m_r}}. \tag{3.17}$$

Next, we quantize the phase introducing the operators $a^\dagger$, a. The momentum variable $p_\varphi = m_\varphi\dot{\varphi}$ stays the same as in the previous case and the displacement dependent cavity frequency is different from Eq.(3.10),

$$\omega_c(x) = \sqrt{\frac{4\pi I_0 S(\varphi_-)\cos\left(\frac{\alpha_I\xi}{S(0)^2}x\right)}{C\Phi_0}}. \tag{3.18}$$

Then, the Hamiltonian in terms of the cavity operators has the following form

$$H = \frac{m_r\dot{x}^2}{2} + \frac{m_r{\omega_m'}^2x^2}{2} + \hbar\omega_c(x)a^\dagger a - \frac{2\hbar I_0 S(\varphi_-)}{\sqrt{2\hbar C\omega_c(x)}}\sin\left(\frac{\alpha_I\xi}{S(0)^2}x\right)(a^\dagger + a). \tag{3.19}$$

We expand the full Hamiltonian to the second order in the displacement and use the creation and annihilation operators $b^\dagger$, b of the mechanical resonator. It leads to the uncoupled cavity Hamiltonian $\hbar\omega_c(0)a^\dagger a$ and the uncoupled mechanical resonator Hamiltonian $\hbar\omega_m' b^\dagger b$. Applying the rotating-wave approximation results in the interaction Hamiltonian of the following form

$$H_{int} = \hbar g_Q^{2r} a^\dagger a b^\dagger b - \hbar g_{BS}^{1r}(a^\dagger b + b^\dagger a), \tag{3.20}$$

where the cross-Kerr and the single-photon beam splitter couplings, respectively, are

$$g_Q^{2r} = x_{ZPF}^2\frac{\partial^2\omega_c^r}{\partial x^2}\Big|_{x=0} = g_Q^2 - \frac{\alpha_I^2\xi^2}{2S(0)^4}\omega_c(0), \tag{3.21}$$

$$g_{BS}^{1r} = x_{ZPF}\frac{\alpha_I\xi\sqrt{\omega_c(0)E_J}}{S(0)\sqrt{\hbar S(0)}}. \tag{3.22}$$

To plot these couplings, we use set of parameters for the nanoSQUID with CNT junctions [30]: $I_0 = 15$ nA, $C = 90$pF, $A = 800$ nm $\times$ 800 nm, $l = 200$ nm, and $m_r = 5$ ag. The cavity frequency for this values is 1 GHz. The mechanical frequency is taken to be $\omega_m' = 1$ GHz, which is possible to reach with a suspended CNT. The flux bias varies from $\phi_b = 2\pi n$ to $\phi_b = 2\pi n + \pi$, where $n = 18$.

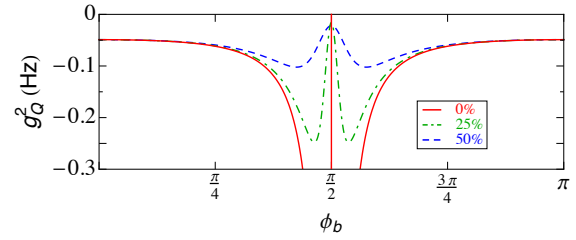

(a)

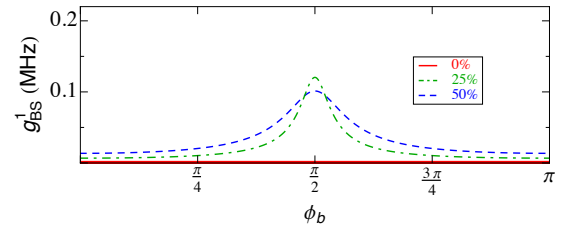

(b)

Figure 3.5: Interaction couplings for symmetric and asymmetric SQUID in the case of $\omega_c(0) \sim \omega_m'$ and magnetic field $B = 10$ mT: (a) cross-Kerr coupling, (b) single-photon beam splitter coupling. The flux bias is shifted by $12\pi BA/\Phi_0 = 2\pi 18$.

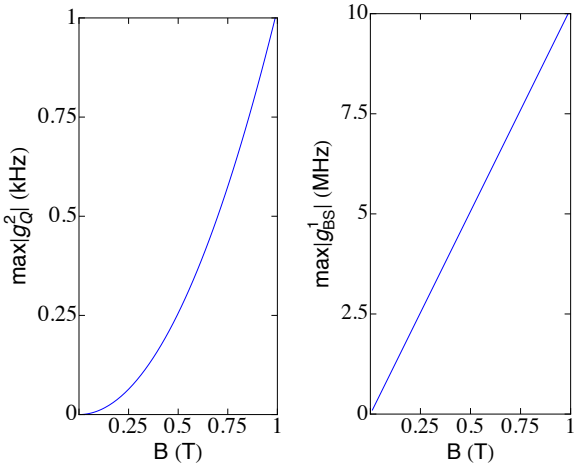

(a) (b)

Figure 3.6: The maximum of (a) the cross-Kerr coupling and (b) the single-photon beam splitter coupling at 50% asymmetry, as a function of the magnetic field corresponding to Fig. 3.5. The flux bias is fixed to the sweet spot of each coupling.

In Fig. 3.5(a), we plot the cross-Kerr coupling. The coupling g_Q^2 is overall weaker than the one we found in Fig. 3.3(b). For the symmetric case, the behaviour is the same as we have seen in the dispersive regime. However, for finite asymmetry the behavior is qualitatively different since the coupling is negative and does not change the sign from negative to positive. Also, there is a peak of the coupling close to $\pi/2$ and at exactly half flux quantum there is a minimum. This happens because of the second term in Eq.(3.21), which arise due to the modified cavity frequency. For lower asymmetry the minimum is getting closer to zero while the maximum is increasing.

Fig. 3.5(b) shows the single-photon beam splitter coupling. For $\omega_c(0) \gg \omega_m'$ this coupling is negligible, because the corresponding term in the Hamiltonian is a quickly oscillating function of time. It only exists at a finite asymmetry. The single-photon beam splitter coupling is slowly increasing while flux rises from 0 to $\pi/2$ and reaches its maximum at the half flux quantum and then passing this point decreases again. For lower asymmetry the peak is higher, but the window to reach higher value is narrower, since the higher asymmetry corresponds to a higher value of the coupling except for close to half-integer flux quantum.

In Fig. 3.6 we show the maximum of both couplings at the 50% asymmetry while increasing magnetic field to 1 T. The cross-Kerr coupling reaches 1 kHz. The single-photon beam splitter coupling has the value up to 10 MHz. In comparison with the mechanical frequency it is not in the ultrastrong coupling regime, but depending on the cavity decay rate it can be in the strong-coupling regime. While often radiation pressure is linearized to produce the beam splitter term to solve specific systems and phenomenon, g_{BS}^{2r} has intrinsically a beam splitter character even at the single-photon level. At very small asymmetry and strong magnetic fields the cross-Kerr coupling can be larger than beam-splitter interaction.

3.4. DISCUSSION

To gain the intuition about the couplings and to better understand the asymmetric system we plot the potential energy as a function of flux (φ_-) and phase (φ_+) in Fig. 3.7. For the symmetric junctions the potential is symmetric along dashed line. At the bottom of the potential radiation pressure is zero and cross-Kerr coupling is finite. For the asymmetric case the potential has an elliptical form and is asymmetric. One can further study the figures on the bottom corresponding to the cross-section of the energy map for different flux. The cross-sections are chosen by moving the horisontal dashed line up. In the symmetric case the minimum of the potential energy stays at the same position. In contrast, for the asymmetric junctions the position of the minimum shifts, which is also described by Eq.(3.7). In the case of dispersive frequencies, this shift it constant and the minimum is redefined at each bias flux, which represents the same physics as for the symmetric case. However, elliptical form alters the radiation pressure and cross-Kerr couplings and changes its behavior as previously appeared in Fig. 3.3 around half-integer flux quantum where there is a merge between elliptical forms.

For the case of resonant frequencies and asymmetric SQUID, the minimum of the potential energy is shifted by the displacement dependent flux. The oscillations of the mechanical resonator correspond to the motion from one curve to another one. The force that triggers the motion between the minima is just like the Lorentz force, which

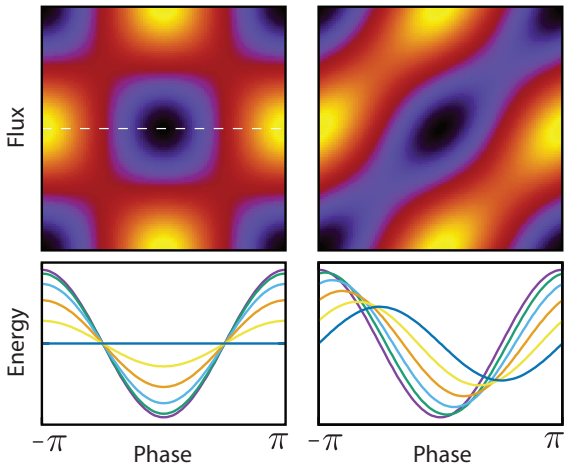

Figure 3.7: Potential energy as a function of the phase and flux at 0% (on the left) and 50% asymmetry(on the right). The minimum is shown in black and maximum in yellow. The corresponding cross section of energy map for the different flux is displayed on the bottom.

explains the appearance of the single-photon beam splitter and the extra term picked up by cross-Kerr coupling as compared to the dispersive regime.

We now discuss the mechanical frequency shifts due to the Josephson term in Eqs.(3.8) and (3.17). In the parameter regime we have chosen this shift can be disregarded. However, for higher Josephson energy, which could depend on the magnetic field itself, or larger parameters of the mechanical resonator increasing magnetic field to 1 T can create a large shift, which should be taken into account. The mechanical zero-point fluctuation in such situation becomes smaller, subsequently the values of the couplings decrease, but we do not expect the change in the overall behavior of the optomechanical couplings.

Generally, the SQUID is an intrinsically nonlinear cavity and close to the half integer flux quantum an extra nonlinear Kerr-type term $\Lambda a^\dagger a a a^\dagger$ appears in the Hamiltonian of Eqs. (3.11) and (3.19), where the Kerr nonlinearity is $\Lambda = \hbar\pi^2/(4C\Phi_0^2)$. This term results from the expansion of the potential energy to the forth order in the overall phase φ. Thus, a cavity can be considered linear as long as Λ is less than the cavity linewidth and $\omega_c(0) \gg \Lambda$, which gives a finite condition for the flux bias close to the half integer flux quantum. Close to the half flux quantum the Kerr-type term and the cross-Kerr term are always present in this system. From the fourth order expansion of the potential energy there are also other nonlinear interaction terms such as $a^\dagger a^\dagger a a b^\dagger b$ in the dispersive case or $a^\dagger a^\dagger a b$ in the resonant case, which are always small.

3.5. CONCLUSIONS

We provided a quantum analysis of the SQUID with asymmetric Josephson junctions and embedded mechanical resonator for two cases of the dispersive and resonant cav-

ity and mechanical frequencies. Our findings are significant for the experimental setup where asymmetry cannot be avoided. We found that the radiation pressure for the resonant frequencies has a sweet spot, which is located at an asymmetry dependent flux point. Shifting this point towards the half-integer flux quantum results in a weaker coupling. Even at 50% asymmetry and weak magnetic field the radiation pressure coupling can be in the strong coupling regime. For high magnetic fields, the ultrastrong coupling regime of the radiation pressure can be achieved. The cross-Kerr coupling is finite at the odd integer flux quantum, in contrast to the radiation pressure coupling. For the symmetric case, it is always negative and infinitely strong very close to the half-integer flux quantum. For the dispersive asymmetric case, the cross-Kerr coupling has maximum at half-integer flux quantum and changes sign from negative to positive while reaching maximum. For the resonant asymmetric case, the minimum sits at the half-integer flux quantum and maximum is at the flux dependent point close to $\pi/2$. For the resonant case, the radiation pressure is too weak since it oscillates at higher frequency and instead single-photon beam splitter interaction is the main term in the Hamiltonian. It is always finite and has its maximum at the half-integer flux quantum.

We explained the origin of different couplings using the potential energy map as well as compared the maps for the symmetric and asymmetric cases. The biggest challenge to experimentally work with single-photon beam splitter coupling is the condition on the mechanical frequency, which should be comparable to the cavity frequency. Experiments involved such setup previously [25–27] had mechanical frequency smaller than cavity frequency. However, using carbon nanotubes as a mechanical resonator coupled to the Josephson circuit can potentially solve the high mechanical frequency issue.

REFERENCES

[1] M. Aspelmeyer, T. J. Kippenberg, and F. Marquardt, Rev. Mod. Phys. **86**, 1391 (2014).

[2] J. Chan, T. P. M. Alegre, A. H. Safavi-Naeini, J. T. Hill, A. Krause, S. Grö blacher, M. Aspelmeyer, and O. Painter, Nature (London) **478**, 89 (2011).

[3] J. D. Teufel, T. Donner, D. Li, J. W. Harlow, M. S. Allman, K. Cicak, A. J. Sirois, J. D. Whittaker, K. W. Lehnert, and R. W. Simmonds, Nature (London) **475**, 359 (2011).

[4] G. S. Agarwal and S. Huang, Phys. Rev. A **81**, 041803 (2010).

[5] S. Weis, R. Rivire, S. Delglise, E. Gavartin, O. Arcizet, A. Schliesser, and T. J. Kippenberg, Science **330**, 1520 (2010).

[6] A. H. Safavi-Naeini, S. Gröblacher, J. T. Hill, J. Chan, M. Aspelmeyer, and O. Painter, Nature (London) **500**, 185 (2013).

[7] T. P. Purdy, P.-L. Yu, R. W. Peterson, N. S. Kampel, and C. A. Regal, Phys. Rev. X **3**, 031012 (2013).

[8] E. E. Wollman, C. Lei, A. Weinstein, J. Suh, A. Kronwald, F. Marquardt, A. Clerk, and K. Schwab, Science **349**, 952 (2015).

[9] F. Lecocq, J. B. Clark, R. W. Simmonds, J. Aumentado, and J. D. Teufel, Phys. Rev. X **5**, 041037 (2015).

[10] J.-M. Pirkkalainen, E. Damskägg, M. Brandt, F. Massel, and M. A. Sillanpää, Phys. Rev. Lett. **115**, 243601 (2015).

[11] V. Fiore, Y. Yang, M. C. Kuzyk, R. Barbour, L. Tian, and H. Wang, Phys. Rev. Lett. **107**, 133601 (2011).

[12] T. A. Palomaki, J. W. Harlow, J. D. Teufel, R. W. Simmonds, and K. W. Lehnert, Nature (London) **495**, 210 (2013).

[13] M. Wallquist, K. Hammerer, P. Rabl, M. Lukin ,and P. Zoller, Phys. Scr. **T137**, 014001 (2009).

[14] E. Knill, R. Laflamme, and G. J. Milburn, Nature (London) **409**, 46 (2001).

[15] C. H. Bui, J. Zheng, S. W. Hoch, L. Y. T. Lee, J. G. E. Harris, and C. W. Wong, App. Phys. Lett. **100**, 021110 (2012).

[16] P. Rabl, Phys. Rev. Lett. **107**, 063601 (2011).

[17] S. Gupta, K. L. Moore, K. W. Murch, and D. M. Stamper-Kurn, Phys. Rev. Lett. **99**, 213601 (2007).

[18] J. R. Johansson, G. Johansson, and F. Nori, Phys. Rev. A **90**, 053833 (2014).

[19] T. T. Heikkilä, F. Massel, J. Tuorila, R. Khan, and M. A. Sillanpää, Phys. Rev. Lett. **112**, 203603 (2014).

[20] P. D. Nation, J. Suh, and M. P. Blencowe, Phys. Rev. A **93**, 022510 (2016).

[21] J.-M. Pirkkalainen, S. U. Cho, F. Massel, J. Tuorila, T. T. Heikkilä, P. J. Hakonen, and M. A. Sillanpää, Nature Communications **6**, 6981 (2015).

[22] X. Zhou and A. Mizel, Phys. Rev. Lett. **97**, 267201 (2006).

[23] E. Buks and M. P. Blencowe, Phys. Rev. B **74**, 174504 (2006).

[24] S. Pugnetti, Y. M. Blanter and R. Fazio, Europhys. Lett. **90**, 48007 (2010).

[25] S. Etaki, M. Poot, I. Mahboob, K. Onomitsu, H. Yamaguchi and H. S. J. van der Zant, Nature Physics **4**, 785 (2008).

[26] S. Etaki, F. Konschelle, Ya. M. Blanter, H. Yamaguchi, and H. S. J. van der Zant, Nature Communications **4**, 1803 (2013).

[27] M. Poot, S. Etaki, I. Mahboob, K. Onomitsu, H. Yamaguchi, Ya. M. Blanter, and H. S. J. van der Zant, Phys. Rev. Lett. **105**, 207203 (2010).

[28] D. H. Santamore, A. C. Doherty, and M. C. Cross, Phys. Rev. B **70**, 144301 (2004).

[29] E. A. Laird, F. Pei, W. Tang, G. A. Steele, and L. P. Kouwenhoven, Nano Lett. **12**, 193 (2012).

[30] J.-P. Cleuziou, W. Wernsdorfer, V. Bouchiat, T. Ondarcuhu, and M. Monthioux, Nature Nanotech. **1**, 53 (2006).

[31] B. H. Schneider, S. Etaki, H. S. J. van der Zant, and G. A. Steele, Scientific Reports **2**, 599 (2012).

[32] D. Lee, M. Underwood, D. Mason, A. B. Shkarin, S. W. Hoch, and J. G. E. Harris, Nature Com. **6**, 6232 (2015).

4

QUANTUM ANALYSIS OF THE NONLINEAR CAVITY WITH A MECHANICAL RESONATOR

O. Shevchuk, R. Fazio, and Ya. M. Blanter

We investigate the effects of the nonlinearity on the cavity frequency and the dissipation in the superconducting quantum interference device (SQUID) coupled to an embedded mechanical resonator. The effective cavity frequency and dissipation are found using the self-consistent harmonic approximation (SCHA).For the dissipationless case, the cavity frequency shift is found for the high temperature limit and zero temperature. The case including the dissipation is studied for low temperature and we obtained the shifts of the dissipation and the cavity frequency.

4.1. SELF-CONSISTENT HARMONIC APPROXIMATION

Feynman was the first who introduced the idea of effective potential, which meant to reduce quantum mechanical calculations to the classical equations but still portray the quantum effects [1]. To find the effective potential, the so-called trial action is used in a variational theorem for the path-integral expression of the partition function also known as self-consistent harmonic approximation (SCHA) [2]. It states that the free energy obeys inequality $F \leq F_0 + \frac{1}{\hbar\beta}\langle S - S_0\rangle_{S_0}$, where S and F are the full action and the free energy of the system under investigation, respectively. At the same time, S_0 and F_0 are any action and, corresponding to it, free energy. Using this approach one can take into account the quantum dissipation in the effective potential formalism. By using the SCHA method in this chapter, we find the effects of the nonlinearity on the cavity frequency and dissipation for the discussed in Chapter 2 and 3 the nonlinear SQUID cavity with an embedded mechanical resonator. We start with writing the full Hamiltonian for the nonlinear SQUID with idential junctions in Sec. 4.2. Then in Sec.4.3 we focus on the dissipationless case for the two regimes of the high temperature and zero temperature and find the effective frequency. In the last Sec. 4.4, we look at the low temperature limit and obtain effective dissipation and frequency.

4.2. KERR NONLINEARITY

The system we consider is the same as in previous two chapters. In Chapter 2, we focused on the classical backaction effects and here we perform quantum analysis of this system. In Chapter 3, we did not address in full the intrinsic nonlinearity of the SQUID and focused on the quantum details of the linear cavity and asymmetry of the Josephson junctions while here the Josephson junctions are assumed to be almost identical. Moreover, the frequency of the mechanical resonator is considered to be much lower than the cavity frequency and the dissipation is lower than the mechanical frequency. The full Hamiltonian of the system is given by eq.(3.6) with $\alpha_I = 0$ and we expand potential energy E of the SQUID up to the fourth order in the dynamical variables resulting in the full Hamiltonian

$$H = \frac{m_r\dot{x}^2}{2} + \frac{m_r\omega_m^2 x^2}{2} + \frac{C\Phi_0^2}{2(2\pi)^2}\dot{\varphi}_+^2 + E_J\cos(\phi_b)\left(\varphi_+^2 - \frac{\varphi_+^4}{12}\right) - E_J\sin(\phi_b)\xi x\varphi_+^2. \tag{4.1}$$

Following the previous chapter, the quantization can be performed by introducing creation and annihilation operators for the mechanical ($b^{\dagger}$) and cavity ($a^{\dagger}$) modes with the flux dependent and, hence, the displacement dependent cavity frequency

$$\omega_c(x) = \sqrt{\frac{4\pi I_0\cos(\phi_b + \xi x)}{C\Phi_0}}. \tag{4.2}$$

so that

$$b^{\dagger} = \frac{1}{\sqrt{2m_r\hbar\omega_m}}\left(m_r\omega_m x \mp ip\right). \tag{4.3}$$

$$a^{\dagger} = \frac{1}{\sqrt{2\hbar m_\varphi\omega_c(\varphi_-)}}\left(m_\varphi\omega_c(\varphi_-)\varphi_+ \mp ip_\varphi\right), \tag{4.4}$$

After applying the rotation-wave approximation and eliminating all terms oscillating at high frequency the Hamiltonian of the system is

$$H = \hbar\omega_m b^\dagger b + \hbar\omega_c a^\dagger a - \hbar\Lambda a^\dagger a a a^\dagger - \hbar g_0 a^\dagger a(b^\dagger + b). \tag{4.5}$$

The single-photon radiation pressure coupling for the identical junctions case and the Kerr-type nonlinearity, which in the classical physics is referred to as the Duffing nonlineairy is given by the identities

$$g_0 = \xi x_{ZPF} \tan(\phi_b)\frac{\omega_c(0)}{2}, \quad \Lambda = \frac{\hbar}{16 m_\varphi} = \frac{\hbar\pi^2}{4C\Phi_0}. \tag{4.6}$$

This demonstrates that the Kerr nonlinearity is determined by the capacitance of the SQUID. The further findings in this chapter can be represented in terms of the radiation pressure coupling and the Kerr nonlinearity constant.

4.3. DISSIPATIONLESS ACTION

We consider Hamiltonian derived in the previous section and proceed with writing an euclidean action of the system in order to use SCHA

$$S_{x\varphi_+} = \int_0^{\hbar\beta} d\tau \left[\frac{m_r \dot{x}^2}{2} + \frac{m_r \omega_m^2 x^2}{2} + \frac{m_\varphi \dot{\varphi}_+^2}{2} + E(\varphi_+, x) \right], \tag{4.7}$$

where $\beta = 1/(k_B T)$ with the temperature T and the Boltzmann constant k_B. Since the focus of this chapter is on the Kerr nonlinearity as well as effect of optomechanical coupling on the cavity quantities we eliminate phonons by integrating them out of the path integral

$$\begin{aligned} Z = \quad & \oint\!\!\!\!\!\!\int \exp\left[-\frac{1}{\hbar}\int_0^{\hbar\beta} d\tau \left(\frac{m_\varphi \dot{\varphi}_+^2}{2} + \frac{m_\varphi \omega_c^2 \varphi_+^2}{2} - \frac{m_\varphi \omega_c^2 \varphi_+^4}{24} \right) \right] \times \\ & \exp\left[-\frac{1}{\hbar}\int_0^{\hbar\beta} d\tau \left(\frac{m_r \dot{x}^2}{2} + \frac{m_r \omega_m^2 x^2}{2} - E_J \sin(\phi_b)\xi x \varphi_+^2 \right) \right] \mathscr{D}\varphi_+ \mathscr{D}x, \end{aligned}$$

where Z is the partition function.The mechanical resonator can be viewed as a simple harmonic oscillator and the interaction with the SQUID cavity is parametrically driving the mechanical resonator as an external force. The integration results in the effective action in terms of the cavity modes [4]

$$\begin{aligned} S = & \int_0^{\hbar\beta} d\tau \left[\frac{m_\varphi \dot{\varphi}_+^2}{2} + \frac{m_\varphi \omega_c^2 \varphi_+^2}{2} - \frac{m_\varphi \omega_c^2 \varphi_+^4}{24} \right] \\ & - \frac{E_J^2 \sin(\phi_b)^2 \xi^2}{4 m_r \omega_m} \int_0^{\hbar\beta}\int_0^{\hbar\beta} \frac{\cosh(\omega_m|\tau - s| - \frac{\hbar\beta\omega_m}{2})}{\sinh\frac{\hbar\beta\omega_m}{2}} \varphi_+^2(\tau)\varphi_+^2(s) d\tau ds. \end{aligned} \tag{4.8}$$

Next we employ SCHA with the quadratic trial action

$$S_0 = \int_0^{\hbar\beta} d\tau \left[m_\varphi(\dot{\varphi}_+^2 + \omega_{\text{eff}}^2 \varphi_+^2)/2 \right], \tag{4.9}$$

where ω_{eff} is the effective frequency, which corresponds to the shift of the cavity frequency due to the optomechanical coupling and the Kerr nonlinearity. Considering typical experimental situation when the mechanical frequency is much lower than the cavity frequency ($\omega_m \ll \omega_c$) the difference between the full and trial action is free of the term proportional to $\dot{\varphi}_+$. The average of the actions difference can then be found by taking integral of the thermal correlation function $\langle\varphi_+(\tau)\varphi_+(\tau)\rangle$ [5] and using the fact that $\langle\varphi_+^4\rangle = 3\langle\varphi_+(\tau)\varphi_+(\tau)\rangle$. The constant in front of the double integral can be represented in terms of the radiation pressure coupling $m_\varphi^2\omega_c^2 g_0^2/2\hbar$. Evaluating the double integral of the mechanical correlation function together with the cavity correlation function $\langle\varphi_+(\tau)^2\varphi_+(s)^2\rangle = \langle\varphi_+(\tau)\varphi_+(\tau)\rangle + 2\langle\varphi_+(\tau)\varphi_+(s)\rangle$ leads to the final the expression for the action difference

$$\frac{1}{\hbar\beta}\langle S - S_0\rangle = a_{\omega_{\text{eff}}}^2 \frac{m_\varphi(\omega_c^2 - \omega_{\text{eff}}^2)}{2} - \frac{m_\varphi\omega_c^2}{8}a_{\omega_{\text{eff}}}^4 - 2\frac{m_\varphi^2\omega_c^2 g_0^2}{\hbar\omega_m}a_{\omega_{\text{eff}}}^4 + \frac{\hbar g_0^2\omega_c^2}{4\omega_{\text{eff}}^2\omega_m}$$
$$- \frac{m_\varphi\omega_c^2 g_0^2\coth(\hbar\beta\omega_m/2)}{2\omega_{\text{eff}}^2}a_{\omega_{\text{eff}}}^2 + \frac{m_\varphi^2\omega_c^2 g_0^2\omega_m}{4\omega_{\text{eff}}^2}a_{\omega_{\text{eff}}}^4 + \frac{\hbar\omega_c^2 g_0^2\omega_m}{16\omega_{\text{eff}}^4}. \tag{4.10}$$

For the high temperature ($\hbar\beta\omega_c \ll 1$) limit the integral value of the correlation function $\langle\varphi_+(\tau)\varphi_+(\tau)\rangle$ is given by $a_{\omega_{\text{eff}}}^2 = \hbar/(m_\varphi\omega_{\text{eff}})\left[\frac{1}{2} + \bar{n}\right]$ with the number of photons inside the cavity $\bar{n} = 1/(e^{\beta\hbar\omega_{\text{eff}}} - 1)$. In addition, the last four terms in eq. (4.10) can be disregarded as being small in comparison with other terms, however in the low temperature limit they are needed to be taken into account. Overall, it gives a simplified expression for the action difference

$$\frac{1}{\hbar\beta}\langle S - S_0\rangle_{S_0} \approx \frac{\hbar}{2\omega_{\text{eff}}}(\omega_c^2 - \omega_{\text{eff}}^2)(\frac{1}{2} + \bar{n}) - (\frac{1}{4} + \bar{n} + \bar{n}^2)\left(\frac{2\hbar\omega_c^2\Lambda}{\omega_{\text{eff}}^2} + \frac{2\hbar\omega_c^2 g_0^2}{\omega_m\omega_{\text{eff}}^2}\right). \tag{4.11}$$

The free energy of the trial action required for performing SCHA is the free energy of the quantum simple harmonic oscillator $F_0 = \ln\left[\sinh(\hbar\beta\omega_{\text{eff}}/2)\right]/\beta$. We introduce the dimensionless parameters: $\tilde{\Lambda} = \Lambda/\omega_c$, $\tilde{g} = g_0/\omega_c$, $\tilde{\omega}_m = \omega_m/\omega_c$, $\tilde{\omega}_{\text{eff}} = \omega_{\text{eff}}/\omega_c$, and $t_h = \hbar\beta\omega_c$. Then the effective frequency $\tilde{\omega}_{\text{eff}}$, which minimizes the free energy $F_0 + \frac{1}{\hbar\beta}\langle S - S_0\rangle_{S_0}$, is the solution of the following equation

$$\left(\frac{(1 + 4\bar{n} + 4\bar{n}^2)}{t_h e^{t_h\tilde{\omega}_{\text{eff}}}} + 2\left(2\bar{n}^3 + \bar{n}^2\right)\tilde{\omega}_{\text{eff}}\right)\left(\tilde{\Lambda} + \frac{\tilde{g}^2}{\omega_m}\right) + \bar{n}^2\frac{(\tilde{\omega}_{\text{eff}}^2 - 1)\tilde{\omega}_{\text{eff}}^2}{2} = 0. \tag{4.12}$$

The cavity frequency shift depends on the temperature, the nonlinearity and the radiation pressure coupling, see Fig.4.1. We plot the effective frequency using values of the mechanical frequency $\omega_m = 10$ MHz and the cavity frequency $\omega_c = 1$ GHz. The higher temperature increases the shift of the cavity frequency by increasing the influence of the nonlinearity and coupling.

Next, we look at zero temperature regime when $\hbar\beta\omega_m \to \infty$ with the derivative of free energy $\partial F_0/\partial\omega_{\text{eff}} = \hbar/2$. In this case the action difference has following expression

$$\frac{1}{\hbar\beta}\langle S - S_0\rangle_{S_0} = \frac{\hbar}{4\omega_{\text{eff}}}(\omega_c^2 - \omega_{\text{eff}}^2) - \frac{\hbar\omega_c^2\Lambda}{2\omega_{\text{eff}}^2} - \frac{\hbar\omega_c^2 g_0^2}{\omega_m\omega_{\text{eff}}^2}\left(\frac{1}{4} + \frac{\omega_m}{4\omega_{\text{eff}}} - \frac{\omega_m^2}{8\omega_{\text{eff}}^2}\right). \tag{4.13}$$

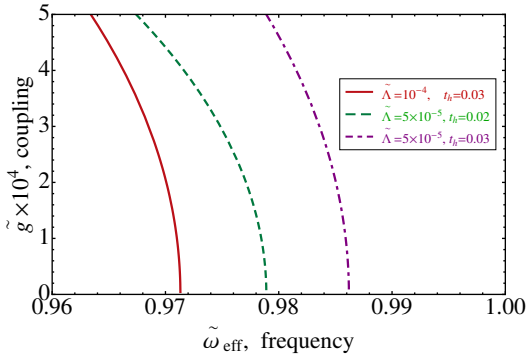

Figure 4.1: Radiation pressure coupling between mechanical oscillator and cavity vs. effective frequency of the cavity for different temperature t_h and non-linearity $\tilde{\Lambda}$.

This results in the effective frequency shift $\omega_{\rm eff} = \omega_c - 2\Lambda - g_0^2/\omega_m - g_0^2/\omega_c$. This shift is different from the one we obtain for the high temperature limit. The shift of the cavity frequency by $2\Lambda + g_0^2/\omega_m$ can be also found by applying *Lang-Firsov(polaron) canonical transformation* [3] to the optomechanical Hamiltonian in eq. (4.5) $\bar{H} = THT^\dagger$ with appropriate choice of transformation $T = \exp\left(-g/\omega_m(b^\dagger - b)a^\dagger a\right)$.

4.4. ACTION WITH DISSIPATION

In this section, we include a dissipation of the SQUID assuming the dissipation in the Josephson junctions is due to an Ohmic resistor. Then to the action derived in the previous section eq.(4.8) we add the dissipation action [6]

$$S_d(\gamma) = \frac{\gamma m_\varphi}{4\pi}\int_0^{\hbar\beta}\int_0^{\hbar\beta}\frac{(\varphi_+(\tau)-\varphi_+(s))^2}{(\tau-s)^2}d\tau\, ds, \tag{4.14}$$

with γ being a dissipation coefficient. It leads to the full action $S + S_d(\gamma)$. We again apply SCHA with the trial action $S_{tr} = S_0 + S_d(\gamma_{\rm eff})$. The correlation functions are described by the standard expression for the damped harmonic oscillator [7]

$$\langle\varphi_+(\tau)\varphi_+(s)\rangle = \frac{1}{m_\varphi\beta}\sum_{n=-\infty}^{+\infty}\frac{e^{i\nu_n|\tau-s|}}{\omega_{\rm eff}^2+\nu_n^2+\gamma_{\rm eff}|\nu_n|}, \tag{4.15}$$

where $\nu_n = 2\pi n/\hbar\beta$ are the Matsubara frequencies. Then, the correlation functions for the phase in the equilibrium state is

$$\langle\varphi_+^2(\tau)\rangle_{S_{tr}} = q^2 = \frac{1}{m_\varphi\beta}\sum_{n=-\infty}^{+\infty}\frac{1}{\omega_{\rm eff}^2+\nu_n^2+\gamma_{\rm eff}|\nu_n|}. \tag{4.16}$$

The next step in SCHA is to evaluate the average of the full and trial actions, which we separate to two parts

$$\langle S + S_d(\gamma) - S_{tr}\rangle_{S_{tr}} = \langle S - S_0\rangle_{S_{tr}} + \langle S_d(\gamma) - S_d(\gamma_{\rm eff})\rangle_{S_{tr}}. \tag{4.17}$$

The full expression for the first term on the r.h.s. is given by

$$\langle S-S_0\rangle_{S_{tr}} = \frac{\hbar\beta m_\varphi(\omega_c^2-\omega_{\rm eff}^2)q^2}{2} - \frac{\hbar\beta m_\varphi\omega_c^2 q^4}{8} - \frac{m_\varphi^2\omega_c^2 g_0^2}{2\hbar}\times$$
$$\int_0^{\hbar\beta}\int_0^{\hbar\beta} d\tau\, ds \frac{\cosh(\omega_m|\tau-s|-\frac{\hbar\beta\omega_m}{2})}{\sinh\frac{\hbar\beta\omega_m}{2}}\times\left(q^4+\frac{2}{\beta^2 m_\varphi^2\omega_{\rm eff}^4}+\right.$$
$$\left.+\frac{8}{\beta^2 m_\varphi^2\omega_{\rm eff}^2}\sum_{n=1}^{+\infty}\frac{\cos\nu_n|\tau-s|}{\omega_{\rm eff}^2+\nu_n^2+\gamma_{\rm eff}\nu_n}+\frac{4}{\beta^2 m_\varphi^2}\sum_{n,k=1}^{+\infty}\frac{(\cos(\nu_n+\nu_k)|\tau-s|+\cos(\nu_n-\nu_k)|\tau-s|)}{\left(\omega_{\rm eff}^2+\nu_n^2+\gamma_{\rm eff}\nu_n\right)\left(\omega_{\rm eff}^2+\nu_k^2+\gamma_{\rm eff}\nu_k\right)}\right).$$

After evaluating the double integral, the difference in actions excluding the action responsible for the dissipation can be written as

$$\frac{1}{\hbar\beta}\langle S-S_0\rangle_{S_{tr}} = \frac{m_\varphi(\omega_c^2-\omega_{\rm eff}^2)q^2}{2} - \frac{m_\varphi\omega_c^2 q^4}{8}$$
$$-\frac{m_\varphi^2\omega_c^2}{\hbar}\frac{g_0^2}{\omega_m}\times\left(q^4+\frac{2}{\beta^2 m_\varphi^2\omega_{\rm eff}^4}+\frac{8\omega_m^2}{\beta^2 m_\varphi^2\omega_{\rm eff}^2}\sum_{n=1}^{+\infty}\frac{\frac{1}{\omega_m^2+\nu_n^2}}{\omega_{\rm eff}^2+\nu_n^2+\gamma_{\rm eff}\nu_n}\right.$$
$$\left.+\frac{4\omega_m^2}{\beta^2 m_\varphi^2}\sum_{n,k=1}^{+\infty}\frac{\frac{1}{\omega_m^2+(\nu_k+\nu_n)^2}+\frac{1}{\omega_m^2+(\nu_k-\nu_n)^2}}{\left(\omega_{\rm eff}^2+\nu_n^2+\gamma_{\rm eff}\nu_n\right)\left(\omega_{\rm eff}^2+\nu_k^2+\gamma_{\rm eff}\nu_k\right)}\right). \tag{4.18}$$

The first sum can be written in terms of the digamma functions

$$\sum_{n=1}^{+\infty}\frac{\frac{1}{\omega_m^2+\nu_n^2}}{\omega_{\rm eff}^2+\nu_n^2+\gamma_{\rm eff}\nu_n} = \left(\frac{\hbar\beta}{2\pi}\right)^4\left(\frac{1}{2it_m}\left[\frac{\psi(1+it_m)}{(z_--it_m)(z_+-it_m)}-\frac{\psi(1-it_m)}{(z_-+it_m)(z_++it_m)}\right]\right.$$
$$\left.+\frac{1}{z_+-z_-}\left[\frac{\psi(1+z_+)}{(z_+^2+t_m^2)}-\frac{\psi(1+z_-)}{(z_-^2+t_m^2)}\right]\right). \tag{4.19}$$

with the arguments

$$z_\pm = \frac{\hbar\beta\omega_{\rm eff}}{2\pi}\left(\zeta\pm i\sqrt{1-\zeta^2}\right),\quad \zeta=\frac{\gamma_{\rm eff}}{2\omega_{\rm eff}},\quad t_m=\frac{\hbar\beta\omega_m}{2\pi}. \tag{4.20}$$

By expanding the digamma functions for the large argument in the low temperature limit, it is easy to see that this term for zero temperature is zero. However, for the temperature corrections this term is important.

To find the double sum, we represent the sum over n in terms of the digamma functions, so that we left only with the sum over k

$$B=\sum_{k=1}^{+\infty}\sum_{\pm}\frac{1}{2it_m(z_+-z_-)}\frac{1}{(k+z_-)(k+z_+)}\times$$
$$\left[\pm\psi(1+z_+)\left(\frac{1}{k-z_\pm-it_m}-\frac{1}{k-z_\pm+it_m}+\frac{1}{k+z_\pm-it_m}-\frac{1}{k+z_\pm+it_m}\right)\right.$$
$$\pm\psi(1+k\pm it_m)\left(\frac{1}{k-z_+\pm it_m}-\frac{1}{k-z_-\pm it_m}\right)$$
$$\left.\pm\psi(1-k\mp it_m)\left(\frac{1}{k+z_+\pm it_m}-\frac{1}{k+z_-\pm it_m}\right)\right]. \tag{4.21}$$

For all the following calculations, we assume the condition for the parameters $\gamma_{\text{eff}} \ll \omega_m \ll \omega_{\text{eff}}$, which are the most common in the experiment. At zero temperature $\hbar\beta\gamma_{\text{eff}} \gg 1$, we can asymptotically expand all the digamma functions to the logarithm. The denominators containing $z_\pm^2 + t_m^2$, $(z_+ - z_-)^2 + t_m^2$, and $(z_+ + z_-)^2 + t_m^2$ can be approximated by $z_\pm^2$, $(z_+ - z_-)^2$, and t_m^2, respectively. The logarithm $\ln(z_\pm \pm i\,t_m)$ we expand to the first order such as $\ln(z_\pm) \pm i\,t_m/z_\pm$. Then, by summing over k and using properties of the digamma function the double sum of eq. (4.20) is

$$B \approx \frac{4\omega_m^2}{\beta^2 m_\varphi^2}\left(\frac{\hbar\beta}{2\pi}\right)^6 \frac{1}{(z_+ - z_-)^2}\left[\frac{\left(\ln\frac{z_+}{z_-}\right)^2}{t_m^2} + \frac{\pi^2}{t_m^2} + \right.$$
$$\pi\left(-\frac{2\ln\frac{z_+}{z_-}}{(z_+ - z_-)\,t_m} + \frac{t_m(z_+^3 + z_-^3)}{4z_+^3 z_-^3} - \frac{t_m(z_+ + z_-)}{z_+ z_-(z_+ - z_-)^2}\right) +$$
$$\left.(z_- + z_+)\left(\frac{\ln\frac{z_-}{t_m}}{z_-^2(z_+ - z_-)} - \frac{\ln\frac{z_+}{t_m}}{z_+^2(z_+ - z_-)} - \frac{2\ln\frac{z_+}{t_m}}{z_+ t_m^2} - \frac{2\ln\frac{z_-}{t_m}}{z_- t_m^2}\right)\right]. \tag{4.22}$$

In order to take a derivative we rewrite B in terms of the original parameters using the relation $\ln z_+/z_- = i(\pi - 2\arcsin(\zeta)) \approx i(\pi - 2\zeta)$.

$$B \approx \frac{\hbar^2}{2\pi m_\varphi^2 \omega_{\text{eff}}^3}\left[\frac{\pi\omega_m}{2} + \frac{\gamma_{\text{eff}}\omega_m^2}{4\omega_{\text{eff}}^2} - \frac{\gamma_{\text{eff}}\omega_m}{2\omega_{\text{eff}}} + \frac{2\gamma_{\text{eff}}^2 \ln\frac{\omega_{\text{eff}}}{\omega_m}}{\pi\omega_{\text{eff}}} - \frac{\gamma_{\text{eff}}^2}{2\pi\omega_{\text{eff}}}\right]. \tag{4.23}$$

The expression for q^2 at zero temperature can be found in the same way by approximating the digamma functions

$$q_0^2 = \frac{\hbar}{2m_\varphi\omega_{\text{eff}}}\left(1 - \frac{1}{\pi}\frac{\gamma_{\text{eff}}}{\omega_{\text{eff}}}\right). \tag{4.24}$$

The second part of the action difference in eq. (4.17) has the double integral

$$\langle S_d(\gamma) - S_d(\gamma_{\text{eff}})\rangle_{S_{tr}} = \frac{(\gamma - \gamma_{\text{eff}})\,m_\varphi}{2\pi} \times \int_0^{\hbar\beta}\int_0^{\hbar\beta} \frac{\langle\varphi_+^2(\tau)\rangle - \langle\varphi_+(\tau)\varphi_+(s)\rangle}{(\tau - s)^2} d\tau\, ds. \tag{4.25}$$

The integral is logarithmically divergent at high frequencies as a consequence of treating Markovian model with the frequency-independent damping, which results in the unphysical assumption of a memoryless reservoir. In a physical system this problem is solved by employing the Drude regularization with a frequency-dependent damping $\gamma_{\text{eff}}(\omega_{\text{eff}}) = \gamma_{\text{eff}}\omega_D/(\omega_D - i\omega_{\text{eff}})$ and Drude frequency ω_D entering the correlation functions

$$\langle S_d(\gamma) - S_d(\gamma_{\text{eff}})\rangle_{S_{tr}} = \frac{2(\gamma - \gamma_{\text{eff}})}{\beta\pi} \times \int_0^{\hbar\beta} ds \sum_{n=1}^{\infty} \frac{\omega_D(1 - \cos\nu_n\zeta)(\hbar\beta - \zeta)}{\zeta^2(\omega_D + \nu_n)\left(\omega_{\text{eff}}^2 + \nu_n^2 + \frac{\gamma_{\text{eff}}\omega_D\nu_n}{\omega_D + \nu_n}\right)}$$
$$= \frac{2(\gamma - \gamma_{\text{eff}})}{\beta\pi} \sum_{n=1}^{\infty} \frac{\omega_D(\hbar\beta\nu_n Si(2\pi n) - \mathbb{C} - \ln(2\pi n) + Ci(2\pi n))}{(\omega_D + \nu_n)\left(\omega_{\text{eff}}^2 + \nu_n^2 + \frac{\gamma_{\text{eff}}\omega_D\nu_n}{\omega_D + \nu_n}\right)} \tag{4.26}$$

where $\mathbb{C}$ is the Euler-Mascheroni constant and we used the special functions [9]:

$$\int_0^z \frac{\sin(z)}{z} = Si(z), \tag{4.27}$$

$$\int_0^z \frac{1-\cos(z)}{z} = \ln(z) + \mathbb{C} - Ci(z). \tag{4.28}$$

The integral $Ci(2\pi) \approx -0.022$ for $n = 1$ is much smaller than the Euler-Mascheroni constant. With increasing n, $Ci(2\pi n)$ becomes even smaller and, hence, can be neglected. The integral $Si(2\pi n)$ with increasing n becomes close to $\pi/2$. Then the first term of the sum containing $Si(2\pi n)$ can be obtained following the method for obtaining the mean-square of the momentum with the Drude regularization [7]. One can show that the next two terms containing $\mathbb{C}$ and logarithm are well described by the purely Ohmic dissipation apart from the corrections of order $\omega_{\text{eff}}/\omega_D$, $\gamma_{\text{eff}}/\omega_D$ and γ/ω_D [8], which are being disregarded in the following evaluation. The term containing logarithm can be approximated by the integral so that we arrive at the following expression

$$\langle S_d(\gamma) - S_d(\gamma_{\text{eff}})\rangle_{S_{tr}} = (\gamma - \gamma_{\text{eff}}) \left(\frac{\hbar^2\beta}{2\pi} \left[2\psi\left(1 + \frac{(\omega_D - \gamma_{\text{eff}})\hbar\beta}{2\pi}\right) - \left(1 + \frac{\gamma_{\text{eff}}}{2i\omega_{\text{eff}}}\right)\psi(1+z_+) - \left(1 - \frac{\gamma_{\text{eff}}}{2i\omega_{\text{eff}}}\right)\psi(1+z_-)\right] - \frac{m_\varphi \mathbb{C}\left(q^2 - \frac{1}{m_\varphi \beta \omega_{\text{eff}}^2}\right)}{\pi} - \frac{\hbar \ln(\hbar\beta\omega_{\text{eff}}) \ln\left(\frac{z_+}{z_-}\right)}{4\pi^2\sqrt{\frac{\gamma_{\text{eff}}^2}{4} - \omega_{\text{eff}}^2}} \right).$$

Again for zero temperature, the last two terms are negligable after dividing difference by $\hbar\beta$. Then, the asymtotic expansion of the digamma functions results in the following dissipation actions difference

$$\frac{1}{\hbar\beta}\langle S_d(\gamma) - S_d(\gamma_{\text{eff}})\rangle_{S_{tr}} = \hbar(\gamma - \gamma_{\text{eff}}) \left[\frac{1}{2\pi} \ln\frac{\omega_D}{\omega_{\text{eff}}} - \frac{\gamma_{\text{eff}}}{8\omega_{\text{eff}}} + \frac{\gamma_{\text{eff}}^2}{8\pi\omega_{\text{eff}}^2} \right]. \tag{4.29}$$

The free energy expansion of the trial action at zero temperature is given by

$$F_0 = \frac{\hbar}{2} \left[\sqrt{\omega_{\text{eff}}^2 - \frac{\gamma_{\text{eff}}^2}{4}} \left(1 - \frac{\gamma_{\text{eff}}}{\pi\omega_{\text{eff}}}\right) + \frac{\gamma_{\text{eff}}}{\pi} + \frac{\gamma_{\text{eff}}}{\pi} \ln\frac{\omega_D}{\omega_{\text{eff}}} \right]. \tag{4.30}$$

Then, in order to minimize the free energy we take the derivative with respect to the effective dissipation and effective frequency

$$\frac{\partial}{\partial\gamma_{\text{eff}}} \frac{1}{\hbar} \left(F_0 + \frac{1}{\hbar\beta}\langle S_d(\gamma) - S_d(\gamma_{\text{eff}})\rangle_{S_{tr}} + \frac{1}{\hbar\beta}\langle S - S_0)\rangle_{S_{tr}} \right) = \frac{(\gamma - \gamma_{\text{eff}})(2\gamma_{\text{eff}} - \pi\omega_{\text{eff}})}{8\pi\omega_{\text{eff}}^2} - \frac{(\omega_c^2 - \omega_{\text{eff}}^2)}{4\pi\omega_{\text{eff}}^2} + \left(\Lambda + \frac{g_0^2}{2\omega_m}\right) \frac{\omega_c^2}{\pi\omega_{\text{eff}}^3} \left(1 - \frac{\gamma_{\text{eff}}}{\pi\omega_{\text{eff}}}\right) + \frac{g_0^2\omega_c^2}{2\pi\omega_m\omega_{\text{eff}}^3} \left[\frac{\omega_m^2}{4\omega_{\text{eff}}^2} - \frac{\omega_m}{2\omega_{\text{eff}}} + \frac{4\gamma_{\text{eff}} \ln\frac{\omega_{\text{eff}}}{\omega_m}}{\pi\omega_{\text{eff}}} - \frac{\gamma_{\text{eff}}}{\pi\omega_{\text{eff}}} \right] = 0, \tag{4.31}$$

$$\frac{\partial}{\partial\omega_{\rm eff}}\frac{1}{\hbar}\left(F_0+\frac{1}{\hbar\beta}\langle S_d(\gamma)-S_d(\gamma_{\rm eff})\rangle_{S_{tr}}+\frac{1}{\hbar\beta}\langle S-S_0)\rangle_{S_{tr}}\right)=$$
$$-\frac{(\gamma-\gamma_{\rm eff})}{2\pi\omega_{\rm eff}}+\left(\frac{\omega_c^2}{\omega_{\rm eff}^3}\left(1-\frac{\gamma_{\rm eff}}{\pi\omega_{\rm eff}}\right)\left(\Lambda+\frac{g_0^2}{2\omega_m}\right)-\frac{\omega_c^2-\omega_{\rm eff}^2}{4\omega_{\rm eff}^2}+\frac{(\gamma-\gamma_{\rm eff})\gamma_{\rm eff}}{8\omega_{\rm eff}^2}\right)\left(1-\frac{2\gamma_{\rm eff}}{\pi\omega_{\rm eff}}\right)$$
$$-\frac{g_0^2\omega_c^2}{2\pi\omega_m\omega_{\rm eff}^4}\left[\frac{3\pi\omega_m}{2}+\frac{5\gamma_{\rm eff}\omega_m^2}{4\omega_{\rm eff}^2}-\frac{2\gamma_{\rm eff}\omega_m}{\omega_{\rm eff}}+\frac{8\gamma_{\rm eff}^2\ln\frac{\omega_{\rm eff}}{\omega_m}}{\pi\omega_{\rm eff}}-\frac{2\gamma_{\rm eff}^2}{\pi\omega_{\rm eff}}\right]=0. \quad (4.32)$$

Solving this sytem of equations, we obtain the shifts of the dissipation and the cavity frequency

$$\gamma_{\rm eff}=\frac{1}{2\pi}\left[-\sqrt{\left(\frac{g_0^2}{\omega_m}(4\ln(\omega_{\rm eff}/\omega_m)-1)+\omega_{\rm eff}\left(\frac{\pi^2}{4}-1\right)+\gamma\pi\right)^2-4\pi\gamma\omega_{\rm eff}\left(\frac{\pi^2}{4}-1\right)+4g_0^2\pi^2}\right.$$
$$\left.-\frac{g_0^2}{\omega_m}(4\ln(\omega_{\rm eff}/\omega_m)-1)+\gamma\pi+\left(\frac{\pi^4}{4}-1\right)\omega_{\rm eff}\right]\approx\gamma-\frac{4\pi}{\pi^2-4}\frac{g_0^2}{\omega_{\rm eff}},$$
$$\omega_{\rm eff}\approx\omega_c-2\Lambda-\frac{g_0^2}{\omega_m}+\frac{4-3\pi^2}{8-2\pi^2}\frac{g_0^2}{\omega_c}.$$

Comparing the effective frequency shift to the dissipationless case, the result is approximately the same, since the coefficient in front of g_0^2/ω_c is approximately 2.18. The dissipation is shifted only by the radiation pressure and in comparison to the effective cavity frequency is free from the intrinsic nonlinearity Λ.

REFERENCES

[1] R. P. Feynman, Phys. Rev. **97**, 660 (1955).

[2] R. P. Feynman, *Statistical Mechanics: A Set of Lectures*, Reading Masachusetts: W.A. Benjamin (1972).

[3] Sec. 4.3 G. D. Mahan, *Many-Particle Physics*, (Kluwer Academic/Plenum Publishers, New York, 2010).

[4] R. P. Feynman and A. R. Hibbs, *Quantum Mechanics and Path integrals*, McGraw-Hills (1965).

[5] Sec. 3 H. Kleinert,*Path Integrals in Quantum Mechanics, Statistics, Polymer Physics, and Financial Markets* , World Scientific Publishing (2004).

[6] V. Ambegaokar, U. Eckern and G. Schön, Phys. Rev. Lett. **48**, 1745 (1982).

[7] H. Grabert, U. Weiss and P. Talkner, Z. Phys. B - Condensed Matter **55**, 87-94 (1984).

[8] U. Weiss, *Quantum Dissipative Systems* , World Scientific Publishing (2008).

[9] I. S. Gradshteyn and I. M. Ryzhik, *Table of Integrals, Series, and Products*, Elsevier Inc. (2014).

5

OPTOMECHANICAL RESPONSE OF A NONLINEAR MECHANICAL RESONATOR

O. Shevchuk, V. Singh, G. A. Steele, and Ya. M. Blanter

We investigate theoretically in detail the nonlinear effects in the response of an optical/ microwave cavity coupled to a Duffing mechanical resonator. The cavity is driven by a laser at a red or blue mechanical subband, and a probe laser measures the reflection close to the cavity resonance. Under these conditions, we find that the cavity exhibits optomechanically induced reflection (OMIR) or absorption (OMIA) and investigate the optomechanical response in the limit of nonlinear driving of the mechanics. Similar to linear mechanical drive, an overcoupled cavity the red-sideband drive may lead to both OMIA and OMIR depending on the strength of the drive, whereas the blue-sideband drive only leads to OMIR. The dynamics of the phase of the mechanical resonator leads to the difference between the shapes of the response of the cavity and the amplitude response of the driven Duffing oscillator, for example, at weak red-sideband drive the OMIA dip has no inflection point. We also verify that mechanical nonlinearities beyond Duffing model have little effect on the size of the OMIA dip though they affect the width of the dip.

This chapter has been published in Phys. Rev. B **92**, 195415 (2015).

5.1. INTRODUCTION

In optomechanics, light and mechanical motion are coupled together by the radiation pressure of photons trapped in an optical cavity. Optomechanics has the potential to provide access to the quantum limit of mechanical motion, and in recent years, has been a field that has been undergoing rapid development [1]. It already resulted in a number of ground-breaking experiments, including, for example, observation of radiation pressure shot noise [2] or optomechanical squeezing of light [3, 4]. Following the first observation of quantum nature of nanomechanical resonator [5], experiments in microwave [6] and cavity optomechanical [7, 8] architectures demonstrated that mechanical resonators can be brought to the quantum regime. The next step will be to achieve reliable quantum manipulation and to use mechanical resonators as quantum memory elements and quantum transducers.

An important tool in optomechanics is an optomechanically induced transparency (OMIT), an effect analogous to electromagnetically induced transparency in quantum optics [9, 10]. In an OMIT experiment, the cavity is strongly driven by a drive (pump) laser at the red sideband — the driving frequency is red-shifted from the cavity resonance by the frequency of the mechanical resonator — and the transmission through the cavity is measured by a probe laser close to the cavity resonance. Due to the interference, the transmission exhibits a narrow peak exactly at the cavity resonance. The width of the peak is determined by the mechanical relaxation rate, and the OMIT peak is typically much more narrow than the cavity resonance. The observation of the OMIT peak serves as the signature of optomechanical coupling and can be used to qualitatively determine the coupling in the experiment. OMIT was first observed in optomechanical experiments in Ref. [12]. It has been heavily used for characterization of optomechanical systems, in particular, for extraction of the value of optomechanical coupling, in both optical [7, 12, 13] and microwave [14, 15] realizations. In single-port cavities, like the one used in Ref. [15], one can only measure reflection. A peak/dip in the reflection coefficient is referred to as optomechanically induced reflection/absorption (OMIR/OMIA) [13].

In most optomechanical experiments, both cavity and mechanical resonator were linear. However, nonlinear effects are conceptually important. In the classical regime, a driven nonlinear oscillator exhibits bistable behavior, which may strongly affect the properties of the system. Moreover, in the quantum regime, nonlinear effects are essential for creation of non-classical states of a nonlinear resonator. There are three sources of nonlinear behavior in cavity and microwave optomechanics. First, the radiation pressure interaction is inherently nonlinear, but typically a cavity is strongly driven by a laser, and in this case the interaction can be linearized [1]. There were theoretical proposals to use the radiation pressure interaction for quantum manipulation of mechanical resonators [16], which require strong coupling regime of operation. Second, a cavity can be made nonlinear. Whereas it is difficult to achieve for optical cavities, microwave cavities can be made nonlinear by adding Josephson junctions. Self-sustained oscillations caused by nonlinear Lorentz force backaction [17] and cavity-induced Duffing behavior of a mechanical resonator [18] were demonstrated in Josephson-based devices the dc regime. Third, mechanical resonators are inherently nonlinear. This is best manifest in low-dimensional resonators such as carbon nanotubes and graphene flakes [19]. In this

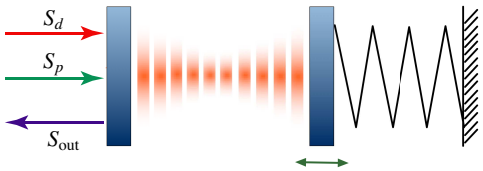

Figure 5.1: Schematic of an optomechanical cavity consisting of a static (left) and a movable (right) mirrors. The movable mirror acts as a mechanical resonator. It is coupled to the cavity through the radiation pressure.

chapter, we concentrate on nonlinear effects in mechanical system.

Nonlinear mechanical effects in optomechanical architecture were experimentally studied in Ref. [20] (see also Ref. [21]). These articles investigated OMIT in an undercoupled optical cavity and discovered that the OMIT feature is still in place, and the shape of the OMIT peak repeats the shape of the frequency response of the driven nonlinear (Duffing) oscillator and exhibits bistability resulting in a hysteretic behavior.

Recently, we performed experimental studies of nonlinear effects in OMIA [22] in the same overcoupled microwave cavity as Ref. [15]. The results we found have a qualitatively different lineshape from that of Ref. [20] — the shape of the OMIA dip in the reflection coefficient of the cavity was distorted by nonlinear effects, however, the shape is different from the response of a driven Duffing oscillator, in particular, it does not have an inflection point.

In this chapter, we provide a theoretical analysis of nonlinear effects on OMIR/OMIA feature and explain the difference between Refs. [20] and [22]. We demonstrate that whereas the OMIR/OMIA feature persists in all situations and exhibits the bistability at strong enough probe powers, its shape is different depending on how the cavity is coupled to an external circuit. We show that the non-Duffing shape of the OMIA response is due to the effect of the phase of the mechanical resonator imprinted on the microwave field. We also analyze the OMIR/OMIA for a blue-detuned drive.

The chapter is organized as follows. In Section 5.2, we develop a general theory of nonlinear effects in OMIR/OMIA based on input-output relations — a standard technique in quantum optics, and derive the OMIA for a red sideband driven overcoupled cavity. In Section 5.3 we generalize the results to the case when the drive is detuned from the red sideband, and in Sec. 5.4 we demonstrate what happens for an undercoupled cavity, connecting our results with Ref. [20], and for a blue sideband drive. In Section 5.5, we consider nonlinear effects beyond the Duffing approximation: The quadratic term in the force and the nonlinear dissipation. Section 5.6 presents the conclusions.

5.2. MODEL OF A DRIVEN NONLINEAR CAVITY

We consider a single-port cavity, which is coupled via the radiation pressure to a nonlinear resonator as shown in Fig. 5.1. The Hamiltonian of the system is

$$\hat{H} = \hbar\omega_c \hat{a}^\dagger \hat{a} + \frac{\hat{p}^2}{2m_r} + \frac{m_r \omega_m^2 \hat{x}^2}{2} + \alpha \frac{\hat{x}^4}{4} + \hbar G \hat{x} \hat{a}^\dagger \hat{a} + i\hbar\sqrt{\eta\kappa}\left[s_{in}(t)\hat{a}^\dagger - s_{in}^*(t)\hat{a}\right] . \quad (5.1)$$

Here $\hat{a}^\dagger(\hat{a})$ is the creation (annihilation) operator for the cavity mode with the cavity frequency ω_c. The resonator with the effective mass m_r and the resonance frequency ω_m is described by the operators of mechanical displacement $\hat{x}$ and momentum $\hat{p}$ operators. The mechanical nonlinearity is described by the Duffing term with the strength α. The radiation pressure term contains the optomechanical coupling constant $G = d\omega_c/dx$ between the mechanical and cavity modes, which corresponds to the shift of the cavity frequency due to the motion of the resonator. The last term describes the coupling of the input signal to the cavity. The cavity coupling parameter is given by $\eta = \kappa_e/(\kappa_0+\kappa_e) = \kappa_e/\kappa$, where κ_0, κ_e and κ denote the intrinsic, the external, and the total dissipation rates, respectively. The input signal $s_{in}(t) = S_d e^{-i\omega_d t} + S_p e^{-i\omega_p t}$ consists of the strong drive field with the normalized field amplitude S_d and drive frequency ω_d and weak probe field with the normalized amplitude S_p and probe frequency ω_p. The amplitudes S_d and S_p are square roots of the corresponding drive/probe power divided by $\hbar\omega_c$ and have dimensions of $s^{-1/2}$. S_p^2 and S_d^2 have the meaning of the incident photon flux measured in photons per second. In the remainder of the chapter we will refer to the amplitudes S_d and S_p simply as drive and probe fields.

5

Writing the Heisenberg equations of motion in the rotating-wave frame of the drive frequency[1, 12] and adding dissipation of the cavity and mechanical modes, we derive the quantum Langevin equations for our system as follows,

$$\frac{d}{dt}\hat{a}(t) = \left(i\Delta - \frac{\kappa}{2}\right)\hat{a}(t) - iG\hat{x}(t)\hat{a}(t) + \sqrt{\eta\kappa}s_{in}(t)e^{i\omega_d t}, \tag{5.2}$$

$$m_r\left(\frac{d^2}{dt^2}\hat{x}(t) + \Gamma_m\frac{d}{dt}\hat{x}(t) + \omega_m^2\hat{x}(t)\right) = -\hbar G\hat{a}^\dagger(t)\hat{a}(t) - \alpha\hat{x}^3(t), \tag{5.3}$$

where $\Delta = \omega_c - \omega_d$ is the detuning between the cavity field and drive field and Γ_m is the damping rate of the resonator.

In the steady-state, disregarding the probe field, the time derivatives vanish, and the static solutions for the intra-cavity field and mechanical displacement obey the following algebraic equations,

$$\overline{a} = \frac{\sqrt{\eta\kappa}}{-i\overline{\Delta} + \kappa/2}S_d, \tag{5.4}$$

$$m_r\omega_m^2\overline{x} + \alpha\overline{x}^3 + \hbar G\overline{a}^2 = 0, \tag{5.5}$$

where $\overline{\Delta} = \Delta - G\overline{x}$ is an effective cavity detuning including the frequency shift due the static mechanical displacement.

Since the probe field is much weaker than the drive field, following the standard methods of quantum optics, we can rewrite each Heisenberg operator as the sum of its steady-state mean value and a small fluctuation, which has zero mean value

$$\hat{a}(t) = \overline{a} + \delta\hat{a}(t) \;\text{ and }\; \delta\hat{x}(t) = \overline{x} + \delta\hat{x}(t). \tag{5.6}$$

In this case, the steady-state values are governed by the drive power and the small fluctuations by the probe power. Then, keeping only the linear terms of the fluctuation operators in the radiation pressure term (disregarding $\delta\hat{a}^\dagger(t)\delta\hat{a}(t)$ and $\delta\hat{a}(t)\delta\hat{x}(t)$), we obtain

the linearized quantum Langevin equations

$$\frac{d}{dt}\delta\hat{a}(t) = (i\overline{\Delta} - \frac{\kappa}{2})\delta\hat{a}(t) - iG\overline{a}\delta\hat{x}(t) + \sqrt{\eta\kappa}S_p e^{-i\Omega t}, \tag{5.7}$$

$$m_r\left(\frac{d^2}{dt^2}\delta\hat{x}(t) + \Gamma_m\frac{d}{dt}\delta\hat{x}(t) + \omega_m^2\delta\hat{x}(t)\right) = -\hbar G\overline{a}(\delta\hat{a}(t) + \delta\hat{a}^\dagger(t)) - \alpha(\delta\hat{x}^3(t) + 3\overline{x}^2\delta\hat{x}(t) + 3\overline{x}\delta\hat{x}^2(t)), \tag{5.8}$$

with $\Omega = \omega_p - \omega_d$ being the detuning of the probe field from the drive. In order to solve this system of equations we introduce the following Ansatz: $\delta\hat{a}(t) = Ae^{-i\Omega t} + A^+e^{+i\Omega t}$. We are interested here in the resolved sideband regime ($\kappa \ll \omega_m$) and close to the blue ($\overline{\Delta} = \omega_m$) or red ($\overline{\Delta} = -\omega_m$) sideband of the drive field, meaning the lower sideband A^+ is far off-resonance and can be neglected. Upon substituting this Ansatz into Eq. (5.7) we derive the amplitude A of the cavity field

$$A = \frac{-iG\overline{a}e^{i\Omega t}\delta\hat{x}}{-i(\overline{\Delta}+\Omega) + \frac{\kappa}{2}} + \frac{\sqrt{\eta\kappa}S_p}{-i(\overline{\Delta}+\Omega) + \frac{\kappa}{2}}. \tag{5.9}$$

Next, we substitute this into Eq. (5.8). This is a nonlinear equation which can be solved in the same way as one solves the forced Duffing oscillator [23]. We rewrite the equation in terms of the dimensionless time $\tau = \omega_m t$ and frequency $\omega = \Omega/\omega_m$

$$\frac{d^2}{d\tau^2}\delta\hat{x}(\tau) + \omega^2\delta\hat{x}(\tau) = -(\omega^2-1)\delta\hat{x}(\tau) - \frac{\Gamma_m}{\omega_m}\frac{d}{d\tau}\delta\hat{x}(\tau) - \frac{\hbar G\overline{a}}{m_r\omega_m^2}(Ae^{i\omega\tau} + A^*e^{-i\omega\tau}) - \frac{\alpha}{m_r\omega_m^2}(\delta\hat{x}^3(\tau) + 3\overline{x}^2\delta\hat{x}(\tau) + 3\overline{x}\delta\hat{x}^2(\tau)). \tag{5.10}$$

The term proportional to $\overline{x}\delta\hat{x}^2$ is dropped since it creates a very small static force. To facilitate analysis of this nonlinear equation, the small asymptotic parameter $\varepsilon \ll 1$ is introduced. Then, assuming weak nonlinearity, weak damping, weak forcing with frequency close to the natural frequency of the mechanical resonator, one can perform transformations: $\alpha/m_r\omega_m^2 \to \varepsilon\alpha/m_r\omega_m^2$, $\Gamma_m/\omega_m \to \varepsilon\Gamma_m/\omega_m$, $\hbar G\overline{a}A/m_r\omega_m^2 \to \varepsilon\hbar G\overline{a}A/m_r\omega_m^2$ and $(\omega^2-1) \to \varepsilon(\omega^2-1)$. This indicates that all parameters on the r.h.s. of eq. (5.10) are small, and we can construct the solution as a power series using the method of multiple scales

$$\delta\hat{x}(\tau) = x_0(t_0,t_1) + \varepsilon x_1(t_0,t_1) + \mathcal{O}(\varepsilon^2), \tag{5.11}$$

with the fast timescale $t_0 = \tau$ and the slow timescale $t_1 = \varepsilon\tau$. Applying two time scales leads to the transformation of the first and second time derivative with respect to time τ

$$\frac{d}{d\tau} = \frac{\partial}{\partial t_0} + \varepsilon\frac{\partial}{\partial t_1} = D_0 + \varepsilon D_1, \tag{5.12}$$

$$\frac{d^2}{d\tau^2} = D_0^2 + 2\varepsilon D_1 D_0 + \mathcal{O}(\varepsilon^2). \tag{5.13}$$

Using relations for the derivatives in the equation of motion for mechanical resonator and collecting orders $\mathcal{O}(1)$ and $\mathcal{O}(\varepsilon)$ yield the pair of differential equations

$$D_0^2 x_0 + \omega^2 x_0 = 0, \tag{5.14}$$

$$D_0^2 x_1 + \omega^2 x_1 = \left(\omega^2 - 1 + \frac{i\hbar G^2 \overline{a}^2 / m_r \omega_m^2}{-i(\overline{\Delta} + \Omega) + \frac{\kappa}{2}}\right) x_0$$
$$-2D_1 D_0 x_0 - \frac{\Gamma_m}{\omega_m} D_0 x_0 - \frac{\hbar G \overline{a} \sqrt{\eta\kappa} S_p e^{-i\omega t_0} / m_r \omega_m^2}{-i(\overline{\Delta} + \Omega) + \frac{\kappa}{2}}$$
$$- \frac{\alpha}{m_r \omega_m^2} (x_0^3 + 3\overline{x}^2 x_0). \tag{5.15}$$

The first equation is a simple harmonic oscillator with the general solution $x_0(t_0, t_1) = X(t_1)e^{-i\omega t_0} + X^*(t_1)e^{i\omega t_0}$. Substituting x_0 to the r.h.s. of eq. (5.15) and collecting terms proportional to the $e^{-i\omega t_0}$ we obtain the force that drives the l.h.s. at its resonance frequency. In order for the perturbation correction x_1 to not diverge, the sum of all collected terms must be zero. It gives rise to the condition for the slowly varying amplitude $X(t_1)$,

$$2i\omega \dot{X} + \left(\omega^2 - 1 + \frac{i\hbar G^2 \overline{a}^2 / m_r \omega_m^2}{-i(\overline{\Delta} + \Omega) + \frac{\kappa}{2}}\right) X$$
$$+ i\omega \frac{\Gamma_m}{\omega_m} X - \frac{\hbar G \overline{a} \sqrt{\eta\kappa} S_p / m_r \omega_m^2}{-i(\overline{\Delta} + \Omega) + \frac{\kappa}{2}} - 3\frac{\alpha}{m_r \omega_m^2} (XX^* + \overline{x}^2) X = 0. \tag{5.16}$$

This is our main result, which in the remainder of the chapter we will simplify looking specifically at the blue or the red sideband of the cavity field.

5.2.1. RED SIDEBAND

For the red sideband, the drive field is fixed close the lower motional sideband $\overline{\Delta} = -\omega_m + \delta$, where δ is a small shift (detuning) from the mechanical frequency. The probe field is slightly detuned from the cavity resonance frequency, $\Omega = \omega_m + \Delta' - \delta$, where Δ' is a small detuning. We also define $g^2 = \hbar G^2 \overline{a}^2 / 2 m_r \omega_m$ and $F = \hbar G \overline{a} \sqrt{\eta\kappa} S_p / m_r \omega_m$. Then Eq. (5.16) is approximated as follows

$$2i\dot{X} + 2\left(\Delta' - \delta + \frac{i\Gamma_m}{2} + \frac{ig^2}{-i\Delta' + \frac{\kappa}{2}}\right) X - \frac{F}{-i\Delta' + \frac{\kappa}{2}} - 3\frac{\alpha}{m_r \omega_m} (XX^* + \overline{x}^2) X = 0. \tag{5.17}$$

Introducing a polar form of the complex amplitude $X(t_1) = \frac{1}{2} b(t_1) e^{-i\phi(t_1)}$ and separating real and imaginary part ($2i\dot{X} = i\dot{b} + b\dot{\phi}$) gives a system of two first-order differential equations for the real amplitude b and phase ϕ. These equations describe a slow time evolution of the amplitude and phase. To find the equilibrium points of this slow flow we look at the solution with constant amplitude($\dot{b} = 0$) and phase($\dot{\phi} = 0$)

$$F\Delta' \sin(\phi) - \frac{\kappa}{2} F \cos(\phi) = g^2 b \Delta' + \left(\frac{\kappa^2}{4} + \Delta'^2\right)\left(\frac{3\alpha}{2 m_r \omega_m} (b^2/4 + \overline{x}^2) - \Delta' + \delta\right) b, \tag{5.18}$$

$$F\frac{\kappa}{2} \sin(\phi) + F\Delta' \cos(\phi) = \left[\left(\frac{\kappa^2}{4} + \Delta'^2\right)\frac{\Gamma_m}{2} + g^2 \frac{\kappa}{2}\right] b. \tag{5.19}$$

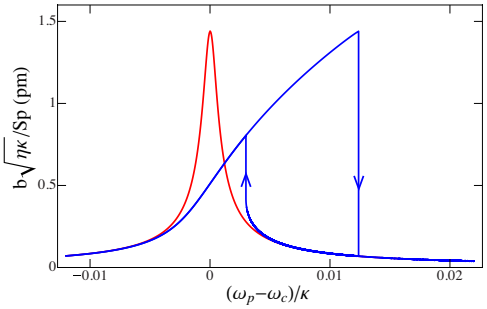

Figure 5.2: The amplitude of the mechanical resonator rescaled by the probe field $S_p = 10^4 s^{-1/2}$(red) and $S_p = 3\times10^6 s^{-1/2}$(blue) as a function of the frequency Δ'/κ driven exactly at the red sideband. For the nonlinear frequency response (blue) the hysteresis occurs. The blue arrow up shows the direction of the jump in the amplitude for decreasing frequency and the blue arrow down shows the direction of the jump for increasing frequency. Most parameters are taken from the experimental paper by Singh *et. al.*[15] with the cavity coupling parameter $\eta = 0.777$, except for the intra-cavity number of photons $\overline{a}^2 = 7.6\times10^6$, mechanical damping $\Gamma_m/2\pi = \ 200\ Hz$, and nonlinearity strength $\alpha = 2\times10^{14}\ \ kg\ m^{-2}s^{-2}$.

5

The results for the amplitude of the mechanical resonator are shown on Fig. 5.2 at zero detuning of the drive ($\delta = 0$) and $\alpha > 0$ as a function of the probe frequency for two probe powers. We see that the behavior is exactly the same as for the Duffing oscillator[23]. At low driving (low probe power) the response of the amplitude is the same as for a linear oscillator and results in a Lorentzian peak. If the probe power increases, the resonant curve becomes asymmetric and develops instability, shown as hysteresis.

The amplitude of the cavity field can now be found using real amplitude and phase of the mechanical oscillator,

$$A = \frac{-iG\overline{a}be^{-i\phi}/2}{-i(\overline{\Delta}+\Omega)+\frac{\kappa}{2}} + \frac{\sqrt{\eta\kappa}S_p}{-i(\overline{\Delta}+\Omega)+\frac{\kappa}{2}}. \tag{5.20}$$

5.2.2. BLUE SIDEBAND

For the blue sideband, we follow the same steps as for the red sideband by taking the frequencies $\Omega = \omega_p - \omega_d = -\omega_m + \Delta' - \delta$ and $\overline{\Delta} = \omega_d - \omega_c - G\overline{x} = \omega_m + \delta$. Consequently, the equations for the amplitude (5.18) and phase (5.19) can be adapted by changing sign in the term on the r.h.s. of Eq. (5.18) by $-\left(\frac{\kappa^2}{4}+\Delta'^2\right)b\Delta' \rightarrow +\left(\frac{\kappa^2}{4}+\Delta'^2\right)b\Delta'$ and in Eq. (5.19) by $\left(\frac{\kappa^2}{4}+\Delta'^2\right)\Gamma_m b/2 \rightarrow -\left(\frac{\kappa^2}{4}+\Delta'^2\right)\Gamma_m b/2$.

5.2.3. REFLECTION COEFFICIENT

In order to study OMIA or OMIR, we need to look at the cavity reflection of the probe field. It is defined by the ratio of the output and input field amplitudes at the probe frequency. The output field of a single port cavity can be found using the input-output relationship

$$s_{out}(t) = s_{in}(t) + \sqrt{\eta\kappa}a(t). \tag{5.21}$$

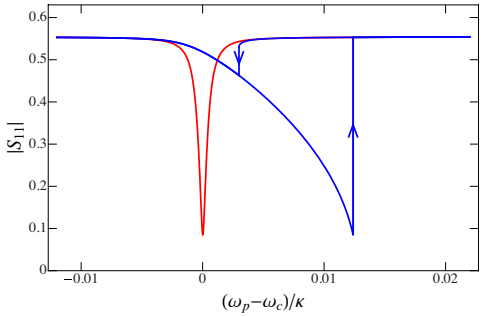

Figure 5.3: Optomechanically induced absorption window found from the cavity reflection coefficient $|S_{11}|$, which corresponds to the mechanical amplitude shown in Fig. 5.2.

Hence, the reflection coefficient of the probe field is given by

$$|S_{11}| = \left|1 - \frac{\sqrt{\eta\kappa}A}{S_p}\right|. \tag{5.22}$$

For a linear mechanical resonator, the amplitude A is linear with the probe field S_p, because the fluctuations of the mechanical resonator $\delta\hat{x}$ are linear with S_p. Hence, the reflection coefficient is independent of the probe field. For a nonlinear resonator the relation is more complex.

At zero detuning $\delta = 0$ and for a linear resonator, the shape of OMIT as the function of the detuning between drive and probe exactly repeats the shape of the response of the amplitude of the mechanical resonator. We see from Eqs. (5.18), (5.19) that this is not the case for a nonlinear resonator. The main reason is that OMIT is not only determined by the dynamics of the amplitude b, but also by the dynamics of the phase shift ϕ, which in turn depends on the frequency. This dependence is essentially an effect of back-action of the cavity on the resonator.

The non-trivial shape of reflection is illustrated in Fig. 5.3 for the same parameters as Fig. 5.2. Note that in the remainder of the chapter we will continue to use the same parameters to visualize the analysis unless mentioned otherwise. Only stable parts of the curve are shown; the bistability results in jumps between different branches of the reflection. It is seen that the reflection close to the cavity resonance is suppressed, indicating OMIA for a single-port cavity. The shape of the OMIA dip for stronger probe (Duffing oscillator) is bistable, however, it does not correspond to the shape of the resonator response (Fig. 5.2), for instance, it does not have an inflection point.

Fig. 5.4 illustrates the dependence of the OMIA dip on the probe field S_p for the same parameters as in Fig. 5.2. The red curve corresponds to the field $S_p = 10^4\, s^{-1/2}$, when the dynamics of the mechanical resonator is linear, and is the same as the red curve in Fig. 5.3. The blue curves, from left to right, correspond to increasing probe power, and the resonator shows nonlinear behavior. We see that upon increasing the probe frequency, the width of the OMIA dip increases and the depth slightly decreases with the probe power. It does not correspond to the Duffing oscillator feature, where the peak height stays unaffected by the drive power.

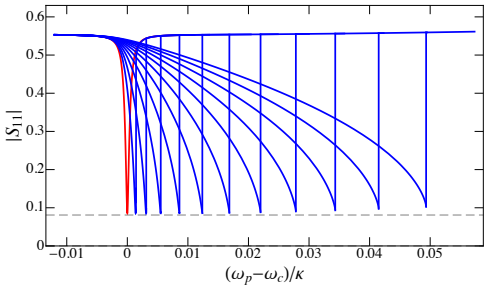

Figure 5.4: OMIA response for different probe fields. The first red curve shows linear response at the probe field $S_p = 10^4 s^{-1/2}$. The dashed grey line represents the peak height of the linear response, in order to compare it with other probe fields. The blue curves start on the left from the probe field $S_p = 1 \times 10^6 s^{-1/2}$ and equally increase the probe field by $S_p = 0.5 \times 10^6 s^{-1/2}$ step up to the last curve on the right, which corresponds to $S_p = 6 \times 10^6 s^{-1/2}$.

In the rest of the chapter, we investigate the effect of different parameters at the response of the cavity.

5.3. OMIA DETUNING

In this Section, we look at the effect of the detuning of the drive δ. The results are shown in Fig. 5.5 for the same parameters as Fig. 5.2 and various values of δ.

Fig. 5.5 (a) and (b) give the general picture of the cavity response in a broad frequency window for positive (a) and negative (b) detunings at weak probe field, $S_p = 10^4 s^{-1/2}$. The detuning breaks the symmetry of the response with respect to the center of the cavity resonance even in the linear case, shifting the OMIA dip. We see indeed that the drive detuning shifts the narrow OMIA dip away from the minimum of the broad cavity resonance. This can be also seen from Eq. (5.18): Indeed, δ enters there in the combination $\delta + 3\alpha b^2/(8 m_r \omega_m)$. We have seen already that increasing the probe power (increasing b) shifts the OMIA minimum to the right, therefore positive δ must shift it to the right as well, and the negative detuning must shift the peak to the left.

Fig. 5.5 (c) and (d) show the structure of the dip for the same parameters as (a) and (b), respectively. The shape is clearly asymmetric and is different from the Lorentzian shown in Fig. 5.3. The flank which is closer to the center of the cavity resonance (the right/left one for negative/positive detuning δ) is sharper than the opposite flank. The OMIA dip at the detuning δ is a mirror reflection of the OMIA dip at the opposite detuning $-\delta$.

Fig. 5.5 (e), (f) and (g), (h) show the cavity response at a stronger probe fields, $S_p = 3 \times 10^6 s^{-1/2}$ and $S_p = 5 \times 10^6 s^{-1/2}$, when the nonlinear nature of the response is well pronounced. First, OMIA dips at δ and $-\delta$ are no more mirror images of each other. For the forward sweep in (e) and (f), if the nonlinear term is positive, $\alpha > 0$, the OMIA dip at negative detuning $-\delta$ is less pronounced than the dip for positive detuning δ. On the contrary, for the backward sweep in (g) and (h), the increase in the probe power results in the decrease of the depth for both, positive and negative, detunings. For a linear sys-

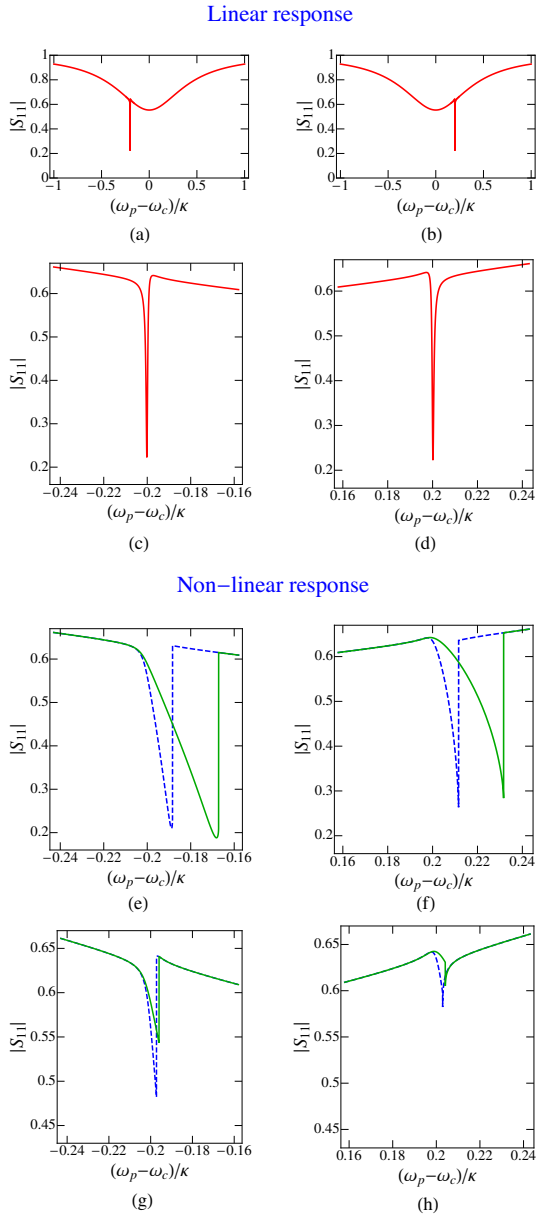

Figure 5.5: OMIA at non-zero detuning. All panels on the left show OMIA for the negative detuning $\delta = -0.2\kappa$; all panels on the right are for the same parameters but the positive detuning $\delta = 0.2\kappa$. (a), (b) The full cavity reflection coefficient in the broad frequency range for the low probe field $S_p = 10^4 s^{-1/2}$, when the cavity can be considered to be linear. (c), (d) Zoom of the linear OMIA peak. (e), (f) Nonlinear OMIA window of the forward frequency sweep for the two probe fields: $S_p = 3 \times 10^6 s^{-1/2}$ (dashed blue line) and $S_p = 5 \times 10^6 s^{-1/2}$ (solid green line). (g), (h) Nonlinear OMIA of the backward frequency sweep for the same probe fields as in (e) and (f).

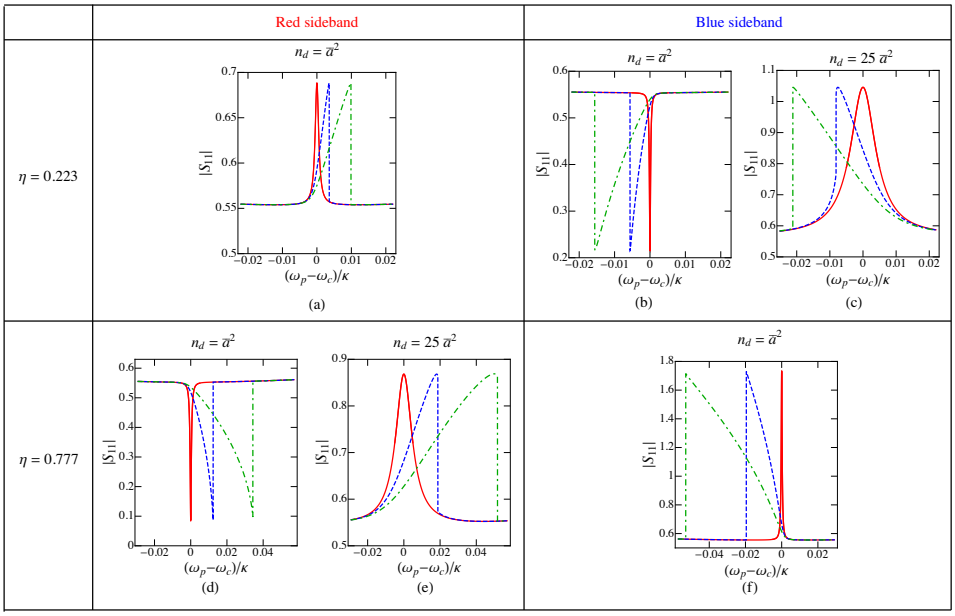

Figure 5.6: Nonlinear response map schematically shows the position and the shape of the OMIA/OMIR features for the undercoupled($\eta = 0.223$), in the first row, and overcoupled($\eta = 0.777$), in the second row, cavity. The two columns represent red and blue sideband. When the intra-cavity number of photons $n_d = \bar{a}^2$ (in the plots (a), (b), (d), and (f)) the reflection coefficient is shown for the probe field $S_p = 10^4 s^{-1/2}$ with the solid(red) line, $S_p = 3\times10^6 s^{-1/2}$ with the dashed(blue) line and $S_p = 5\times10^6 s^{-1/2}$ with the dash-dotted(green) line. For the larger intra-cavity number of photons $n_d = 25\bar{a}^2$ (in the plots (c) and (e)) there is a switch between OMIA and OMIR , then the reflection coefficient is plotted for the following probe fields $S_p = 10^4 s^{-1/2}$ with the solid(red) line, $S_p = 3\times10^7 s^{-1/2}$ with the dashed(blue) line and $S_p = 5\times10^7 s^{-1/2}$ with the dash-dotted(green) line. Each plot corresponds to the different value of the Duffing nonlinearity strength α = (a),(d)2 (b),(f)0.5 (c),(e)0.08 $\times 10^{14}$ $kg\ m^{-2} s^{-2}$.

tem, we would expect a symmetry of the signal $S_{11}(\omega_p - \omega_c; \delta) = S_{11}(-\omega_p + \omega_c; -\delta)$, which would make left and right panels of Fig. 5.5 mirror reflections of each other. In the presence of nonlinearity, the curves are pulled in the same direction. Thus, the symmetry is broken, and therefore the OMIA dip is pronounced for the negative detuning.

5.4. NONLINEAR RESPONSE MAP

So far, we concentrated on red sideband drive and overcoupled cavity, $\eta > 1/2$, and a moderate drive power. In this situation there is an OMIA dip which is again shown in the left curve of the left bottom cell of Fig. 5.6. If the drive power increases, the cavity response S_{11} instead of a minimum shows a maximum. This is an OMIR peak, as demonstrated in the right panel of the same cell of Fig. 5.6. Similarly for OMIA, at weak probe powers the OMIR peak is Lorentzian, and if we increase the probe power, the peak shifts to the right and broadens. Note that whereas the shape of the OMIA dip for weaker drive is different from the response of the mechanical resonator (no inflection point), the shape of the OMIR peak for stronger drive repeats the shape of the resonator response.

In the bottom right cell of Fig. 5.6 we show the results for the same overcoupled cavity driven at the blue sideband. We see that the OMIR peak develops at any drive power. For low probe powers the peak is Lorentzian, and for higher probe powers it shifts to the left and broadens. The shape of the peak is related to the shape of the response of the mechanical resonator, Fig. 5.2.

The qualitative difference between red and blue shifted drive for OMIR/OMIA has already been analyzed in Ref. [15] for the linear dynamics of the mechanical resonator. Indeed, the minimum value of the reflection coefficient is a non-monotonous function of the coupling parameter η: It decreases with η for an undercoupled cavity, reaches zero for an optimally coupled cavity $\eta = 1/2$, and increases with η for an overcoupled cavity. The red/blue sideband drive modifies the cavity linewidth κ_0 such that it becomes $\kappa_0 \pm 4g^2/\Gamma_m$, where the upper/lower sign corresponds to the red/blue detuned drive. Thus, for an overcoupled cavity increasing the drive intensity (proportional to the number of photons in the cavity) for the red sideband drive takes the cavity towards the undercoupled limit, and the behavior changes dramatically when the effective coupling crosses the point $\eta = 1/2$, crossing over from OMIA to OMIR. In contrast, the blue sideband drive only takes the cavity to even stronger overcoupled regime, and there are no qualitative changes. For an undercoupled cavity, the roles of red and blue sideband driving are swapped.

Now we turn to the nonlinear dynamics. From Eq. (5.18) we see that the signs of b^2 and Δ' are opposite for the red sideband drive and the same for the blue sideband drive. This means that since the OMIR peak shifts to the right from the cavity resonance for the red sideband, it shifts to the left for the blue sideband, in full accordance with Fig. 5.6.

The top row of Fig. 5.6 shows OMIA/OMIT for an undercoupled cavity, $\eta < 1/2$. The red sideband drive (top left corner) was previously studied in the experiments [20]. For any drive powers, there is an OMIR peak, and the shape of the peak corresponds to the shape of the Duffing resonator response. The top right corner shows the cavity response for the blue sideband drive. It is similar to what happens in an overcoupled cavity for the red sideband drive: At low probe powers, one has an OMIA dip with the line shape different from the Duffing response of the resonator (no inflection point), whereas for stronger driving, an OMIR peak develops with the Duffing-like shape. The position of the peak is shifted to the left of the cavity resonance with increasing the probe power.

5.5. BEYOND DUFFING

To complete our results, we consider two more nonlinear effects not included in the Duffing model (5.1) — the quadratic term in the displacement and the nonlinear damping. Both can be included in the treatment of Section 5.2.

One phenomenon is the additional term $\beta x^3/3$ in the energy of the mechanical resonator. It produces the force proportional to the coordinate x breaking the symmetry of the oscillator potential and shifting the equilibrium point. Here, we restrict ourselves to the case $\beta > 0$. Fig. 5.7 shows the results for the overcoupled cavity driven exactly at the red sideband, $\delta = 0$. The curve for $\beta = 0$ corresponds to the OMIA dip shown in Fig. 5.3. We see that the only effect of finite β is to shift the position of the OMIA dip to the left of the cavity resonance — in the direction opposite to the shift due to increasing probe power. The shape and the depth of the dip are almost unaffected.

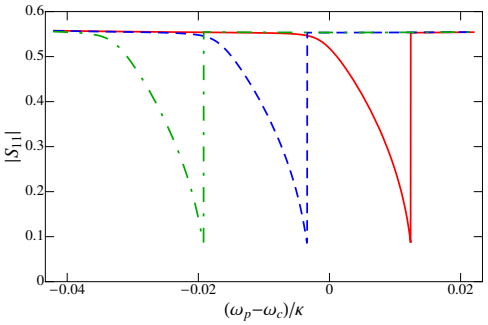

Figure 5.7: Evaluating the contribution of βx^2 to the energy of the mechanical resonator on the OMIA dip. The quadratic nonlinearity $\beta = 0$ is shown by solid(red) line, $\beta = 3\times10^{11}\ \ kg\ m^{-1}s^{-2}$ by dashed(blue) line, and $\beta = 6\times10^{11}\ \ kg\ m^{-1}s^{-2}$ by dash-dotted(green) line for the fixed probe field $S_p = 3\times10^6 s^{-1/2}$. The βx^2 term induces a force-dependent shift of the equilibrium frequency, but otherwise does not change the nonlinear dynamics or optomechanical response.

5

Next, we consider the effect of nonlinear damping, adding the term $-\mu x^2\dot{x}$ to the equations of motion for the resonator. Without the nonlinear term, $\alpha = 0$, this would be the van der Pol resonator [23], obeying the equation of motion

$$m_r\left(\frac{d^2}{dt^2}x + (\Gamma_m - \mu x^2)\frac{d}{dt}x + \omega_m^2 x\right) = F(t)\ ,$$

where F is an external force. For sufficiently large oscillation amplitudes the system would become unstable far from the equilibrium point ($\mu x^2 > \Gamma_m$), however, here we are interested in the situation when the nonlinear term in the damping is a small correction.

Fig. 5.8 shows the effect of the nonlinear damping on the OMIA dip in the same situation as Fig. 5.3. There is an enhancement of the dip for the increasing probe power and positive μ. Correspondingly, for negative μ the dip becomes deeper with increasing probe power.

In general, for specific parameters of the system one can find other nonlinearities, e.g. dissipative [24] or cross-Kerr [25] couplings, which go beyond the scope of our chapter.

5.6. CONCLUSIONS

In this chapter, we systematically investigated the effect of nonlinearities in a mechanical resonator on the OMIR/OMIA feature of a one-port optomechanical cavity. The main result is summarized in Fig. 5.6. We see that depending on whether the cavity is overcoupled or undercoupled, whether it is red or blue sideband driven, and whether the drive power is sufficiently strong, the nonlinear effects either result in OMIR with the shape repeating that of a driven Duffing oscillator (an analog of Ref. [20]), or OMIA with a different shape, as observed in Ref. [22]. The higher is the probe power, the wider is the feature and the more pronounced is the effect of nonlinearity, including the width of the hysteresis range. The depth of the OMIA feature is not significally affected. Furthermore, we investigated the effect of other factors on the OMIA feature and found that

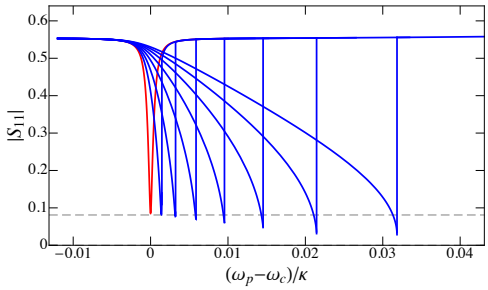

Figure 5.8: OMIA response including negative nonlinear damping for different probe field. The red curve shows the linear response with zero negative nonlinear damping ($-\mu x^2 \dot{x}$) for the probe field $S_p = 10^4 s^{-1/2}$. The dashed grey line represents the peak height of the linear response. The next blue curves include negative nonlinear damping $\mu = 3 \times 10^{19} m^{-2} s^{-1}$. They start with the probe field $S_p = 1 \times 10^6 s^{-1/2}$ and end with $S_p = 4 \times 10^6 s^{-1/2}$ having an equally spaced step in the probe field of $0.5 \times 10^6 s^{-1/2}$. The effect of the negative nonlinear damping term considered here is to increase the depth of the OMIA dip in the optomechanical response with increasing driving force on the mechanical resonator.

the detuning of the drive shifts the OMIA dip and makes it significantly asymmetric, the quadratic term in the oscillator force shifts the position of the dip without considerably affecting its shape, whereas the nonlinear dissipation enhances the dip. These conclusions will help to interpret the results of the cavity response in optomechanical cavities with a nonlinear mechanical component.

Let us now discuss the limitations of our theoretical model. First, our theory is valid in the weak coupling regime, $g \ll \kappa$. Whereas this seems to be sufficient for existing experiments with nonlinear resonators [20, 22], multi-photon strong coupling has already been achieved in the linear mechanical limit [14]. We linearize radiation-pressure interaction, and thus we can also describe multi-photon strong coupling regime using a similar framework. Generalization to the single-photon strong coupling regime is however difficult. Furthermore, we only considered the situation when the probe power is much weaker than the drive power. It would be relatively easy to consider a complementary situation when the probe is much stronger than the drive, however, we have used the method of scale separation, and it fails when the drive and the probe power are comparable. Equations still could be solved numerically in this case.

REFERENCES

[1] M. Aspelmeyer, T. J. Kippenberg, and F. Marquardt, Rev. Mod. Phys. **86**, 1391 (2014).

[2] T. P. Purdy, R. W. Peterson, and C. A. Regal, Science **339**, 801 (2013).

[3] A. H. Safavi-Naeini, S. Gröblacher, J. T. Hill, J. Chan, M. Aspelmeyer, and O. Painter, Nature **500**, 185 (2013).

[4] T. P. Purdy, P.-L. Yu, R. W. Peterson, N. S. Kampel, and C. A. Regal, Phys. Rev. X **3**, 031012 (2013).

[5] A. D. O'Connell, M. Hofheinz, M. Ansmann, R. C. Bialczak, M. Lenander, E. Lucero1,

M. Neeley, D. Sank, H. Wang, M. Weides, J. Wenner, J. M. Martinis, and A. N. Cleland, Nature **464**, 697 (2010).

[6] J. D. Teufel, T. Donner, D. Li, J. W. Harlow, M. S. Allman, K. Cicak, A. J. Sirois, J. D. Whittaker, K. W. Lehnert, and R. W. Simmonds, Nature **475**, 359 (2011).

[7] J. Chan, T. P. Mayer Alegre, A. H. Safavi-Naeini, J. T. Hill, A. Krause, S. Gröblacher, M. Aspelmeyer, and O. Painter, Nature **478**, 89 (2011).

[8] E. Verhagen, S. Deléglise, S. Weis, A. Schliesser, and T. J. Kippenberg, Nature **482**, 63 (2011).

[9] M. O. Scully and M. S. Zubairy, *Quantum Optics*, Campridge University Press (1997).

[10] G. S. Agarwal and S. Huang, Phys. Rev. A **81**, 041803 (2010).

[11] A. N. Cleland, *Foundations of Nanomechanics*, Springer-Verlag, New York (2003).

[12] S. Weis, R. Rivière, S. Deléglise, E. Gavartin, O. Arcizet, A. Schliesser, and T. J. Kippenberg, Science **330**, 1520 (2010).

[13] F. Hocke, X. Zhou, A. Schliesser, T. J. Kippenberg, H. Huebl, and R. Gross, New J. Phys. **14**, 123037 (2012).

[14] J. D. Teufel, D. Li, M. S. Allman, K. Cicak, A. J. Sirois, J. D. Whittaker, and R. W. Simmonds, Nature **471**, 204 (2011).

[15] V. Singh, S. J. Bosman, B. H. Schneider, Y. M. Blanter, A. Castellanos-Gomez, and G. A. Steele, Nature Nanotechnology **9**, 820 (2014).

[16] A. Nunnenkamp, K. Børkje, and S. M. Girvin, Phys. Rev. Lett. **107**, 063602 (2011).

[17] S. Etaki, F. Konschelle, Ya. M. Blanter, H. Yamaguchi, and H. S. J. van der Zant, Nature Communications **4**, 1803 (2013).

[18] L. Ella, D. Yuvaraj, O. Suchoi, O. Shtempluk, and E. Buks, J. Appl. Phys. **117**, 014309 (2015)

[19] A. Eichler, J. Moser, J. Chaste, M. Zdrojek, I. Wilson-Rae, and A. Bachtold, Nature Nanotechnology **6**, 339 (2011).

[20] X. Zhou, F. Hocke, A. Schliesser, A. Marx, H. Huebl, R. Gross, and T. J. Kippenberg, Nature Physics **9**, 179 (2013).

[21] F. Hocke, M. Pernpeintner, X. Zhou, A. Schliesser, T. J. Kippenberg, H. Huebl, and R. Gross, Appl. Phys. Lett. **105**, 133102 (2014).

[22] V. Singh, O. Shevchuk, Ya. M. Blanter, and G. A. Steele, arXiv:1508.04298.

[23] S. H. Strogatz. *Nonlinear dynamics and chaos*, ch. 7, Addison-Wesley, Reading MA (1994).

[24] T. Weiss, Ch. Bruder, and A. Nunnenkamp, New J. Phys. **15**, 045017, (2013).

[25] Raphaël Khan, F. Massel, and T. T. Heikkilä ,Phys. Rev. A **91**, 043822 (2015).

6

NEGATIVE NONLINEAR DAMPING IN THE GRAPHENE RESONATOR

V. Singh, O. Shevchuk, Ya. M. Blanter, and G. A. Steele

We investigate the nonlinear response of a multilayer graphene resonator coupled to a superconducting microwave cavity by theoretically fitting the experimental data. The radiation pressure force drives the mechanical resonator in an optomechanically induced transparency configuration. By varying the amplitudes of drive and probe tones, the mechanical resonator can be brought into a nonlinear limit. Using the calibration of the optomechanical coupling, we quantify the mechanical Duffing nonlinearity. By increasing the drive force, we observe a decrease in the mechanical dissipation rate at large amplitudes, suggesting a negative nonlinear damping mechanism in the graphene resonator. Increasing the optomechanical backaction further, we observe new instabilities in the mechanical response.

Part of this chapter has been published in Phys. Rev. B **93**, 245407 (2016).

6.1. INTRODUCTION

The unique properties of graphene such as atomic thickness, low mass density, and high modulus of rigidity make it very attractive material for nanoscale electromechanical systems (NEMS) for several technological applications. After the first demonstration of a few layers thick graphene NEMS [1], there have been extensive studies on graphene nanoelectromechanical systems ranging from electromechanical resonators [2, 3], oscillators [4] and optomechanical systems aiming to probe the quantum regime of graphene motion [5–8]. In this pursuit, large mechanical quality factors of the order of 10 22×10^4 in graphene based NEMS have been demonstrated as well [5, 9]. Due to its atomic thickness, graphene based NEMS also exhibit rich nonlinearity such as onset of Duffing nonlinearity and nonlinear damping at realativly small mechanical amplitudes [9, 10]. These properties further make graphene an attractive candidate for developing optomechanical systems to reach the quantum regime of graphene motion [11], to store microwave photons [12], and could possibly be useful to understand dissipation in graphene NEMS for improved device performance [13].

The coupling between mechanical resonator and optical/superconducting microwave cavities has enabled the detection of mechanical motion with excellent sensitivities [14–16], offering an attractive platform to characterize the nonlinear response of mechanical resonators. In this chapter, we study nonlinear dynamics of a multilayer graphene resonator, which is coupled to a superconducting microwave cavity. We use theoretical model from previous chapter to explain and fit the experimental results in [17]. The graphene resonator is driven by injecting two microwave tones in the cavity, which are detuned by the mechanical resonant frequency leading to an oscillating radiation pressure force which drives the mechanical resonator. By changing the amplitude of these tones, one can independently control the driving force and dissipation due to the optomechanical backaction forces. We investigate the case when the mechanical resonator can be brought into the Duffing regime and characterize the nonlinearity. With increase in the driving force, we observe a reduction in linear dissipation rate, large hysteresis with sweep direction, and an instability in the mechanical amplitude.

The chapter is structured as follows. In Section 6.2, we describe a device and parameters essential for the theoretical fitting. In Section 6.3 we compare the experimental results and theoreticallly obtained fits with linear dissipation rates and mechanical amplitudes for different probe and drive powers. We also discuss the origin of the extra arrised instabilities and show that such instabilities can not be due to the fifth order nonlinearity. With Section 6.4 we conclude this chapter.

6.2. DEVICE

The device consists of a graphene resonator coupled to a superconducting microwave cavity as studied previously in Ref. [5]. Fig. 6.1(a) shows a scanning electron microscope image of a suspended mechanical resonator coupled to a superconducting microwave cavity. The Hamiltonian of our device is given in eq. (5.1). The superconducting cavity has a resonance frequency of $\omega_c = 2\pi \times 5.90054$ GHz, with an internal dissipation rate $\kappa_i = 2\pi \times 54$ kHz and an external coupling rate $\kappa_e = 2\pi \times 188$ kHz (coupling fraction $\eta = \frac{\kappa_e}{\kappa(=\kappa_e+\kappa_i)} = 0.78$). The graphene resonator forms a mechanically compliant capac-

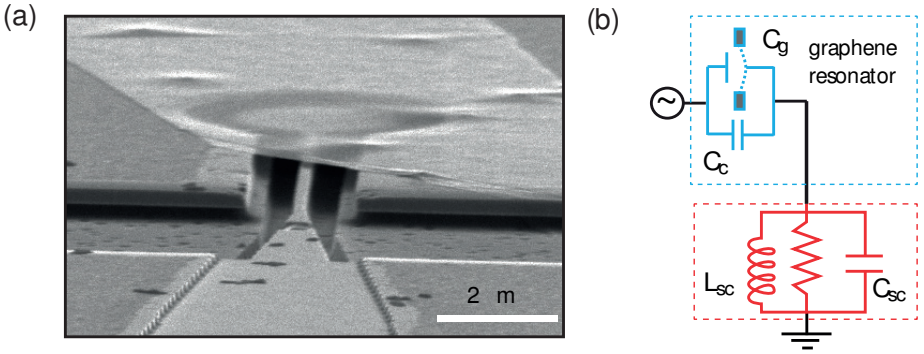

Figure 6.1: (a) A scanning electron micrograph of a multilayer graphene drum-shape resonator coupled to a superconducting microwave cavity (not shown here). Graphene resonator is suspended. (b) Schematic diagram of the device: graphene resonator couples external microwave radiation to the cavity by forming a coupling capacitor.

itor to the microwave feedline as shown schematically in Fig. 6.1(b). The motion of the graphene resonator modulates the capacitance and hence the cavity frequency. The graphene resonator has a resonance frequency of $\omega_m = 2\pi \times 36.233$ MHz. The optomechanical coupling is $2\pi \times 0.83$ Hz [5], defined as $g_0 = \frac{d\omega_c}{dx} x_{\mathrm{XPF}} = G x_{\mathrm{XPF}}$, where x_{XPF} are the quantum zero-point fluctuations of the mechanical resonator.

6.3. EXPERIMENT VS THEORY

In order to probe the mechanical response, we take advantage of the optomechanical coupling and sideband-resolved limit ($\omega_m \gg \kappa$) in an optomechanically induced transparency (OMIT) setup. In Fig. 6.2, we show experimental OMIA response in comparison with theoretical one. The nonlinear response can be primarily captured by including a Duffing term αx^3 in the restoring force of the mechanical resonator. We vary the number of intracavity probe photons n_p, hence the driving force, while keeping the number of drive photons fixed at $n_d = 2.5 \times 10^7$ ($C \sim 0.40$) and 1.0×10^8 ($C \sim 1.24$), respectively. At low number of probe photons, the OMIA feature is determined by the linear response of the mechanical resonator. As n_p is increased further, the nonlinearity in the OMIA response becomes evident with a stiffening of the mechanical resonator (positive shift in the resonance frequency) and the shark-fin like Duffing response accompanied by hysteresis with respect to frequency sweep-direction.

In addition to the clear Duffing response, with the exception of the bottom two curves, it can also be seen that the OMIA dip on the non-linear regime becomes deeper. Qualitatively, the observation of a deeper OMIA dip when n_p is increased can be understood from a reduction of the mechanical damping rate as the resonator is driven to larger amplitudes. Such a decreased mechanical damping rate would give a larger cooperativity and thus a deeper OMIA dip. In the last two curves, the cooperativity is continuing to increase, but the OMIA dip becomes less deep as the cavity has now crossed over to an effective undercoupled regime as also observed for linear mechanical resonator in Ref.[5]. Comparing figures 6.2(a),(b) and (c),(d), smaller and larger n_d respectively, the

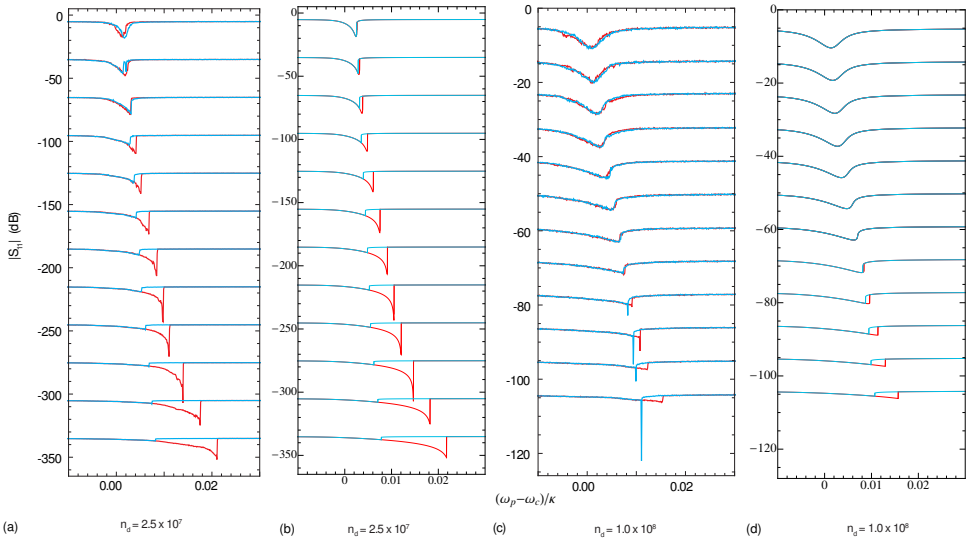

Figure 6.2: Forward (red) and reverse (cyan) frequency sweep (a),(c) measurement and (b),(d) theory of OMIA feature showing mechanical response at various probe and drive powers. The probe photons are swept from $n_p = 2.5 \times 10^5$ to 3.14×10^6 in 1 dB steps (top to bottom). Number of drive photons n_d is fixed at 2.5×10^7 ($C \sim 0.40$) for panels (a),(b) and 1.0×10^8 ($C \sim 1.24$) photons for panels (c),(d). The evolution of nonlinear response accompanied by the hysteresis can be clearly seen as probe power is increased (top to bottom). Panel (c) shows instability points as sharp dips appearing at large probe power. For clarity, measurements in (a),(b) and (c),(d) are plotted with offsets of -30 dB and -9 dB, respectively.

mechanical linewidth in Fig. 6.2(c),(d) is significantly larger. This is a consequence of increased optomechanical damping, which also explains the absence of hysteresis and shows only a transition to a Duffing response at higher powers [18]. Finally, in panels (c) and (d), at the highest drive forces, we also observe an instability in the response in the form of a spike in reverse frequency sweep.

To further show that the theory is comparible with the experiment one of the numerical fitted curve overlaid on top of the experimentally measured data in Fig. 6.3(a). Following theory from Chapter 5, the Duffing parameter is $\alpha = 2.3 \times 10^{15}$ kg m^{-2}s^{-2}, which is given by the gray curve. Using the analytical expression for the onset of the Duffing bifurcation point $\omega_{up} = \omega_m + 3\alpha X_{up}^2/(8 m_{eff}\omega_m)$, we get $\alpha = 2.5 \times 10^{15}$ kg m^{-2}s^{-2}, which is close to the results we get by performing numerical fits. Furthermore, in Fig. 6.3(b, c), we perform numerical fits of the experimental data to extract the linear mechanical dissipation rate (Γ_m), and mechanical amplitude (x_0). It should be noted that in the expression of the Duffing parameter for a given driving force, the mechanical quality factor enters through the amplitude of the resonator at the bifurcation point. At low amplitude, we observe mechanical damping rates Γ_m of $2\pi \times 700$ Hz ($Q_m = 51760$) for $n_d = 2.5 \times 10^7$, while for higher amplitude, the damping rate drops to $2\pi \times 410$ Hz ($Q_m = 88373$). At large number of probe photons, the nonlinear dynamics of the OMIA becomes far more complex. Apart from the nonlinear Duffing response accompanied by the hysteresis, in the experiment there is extra instabilities (sharp absorption features) in the reverse fre-

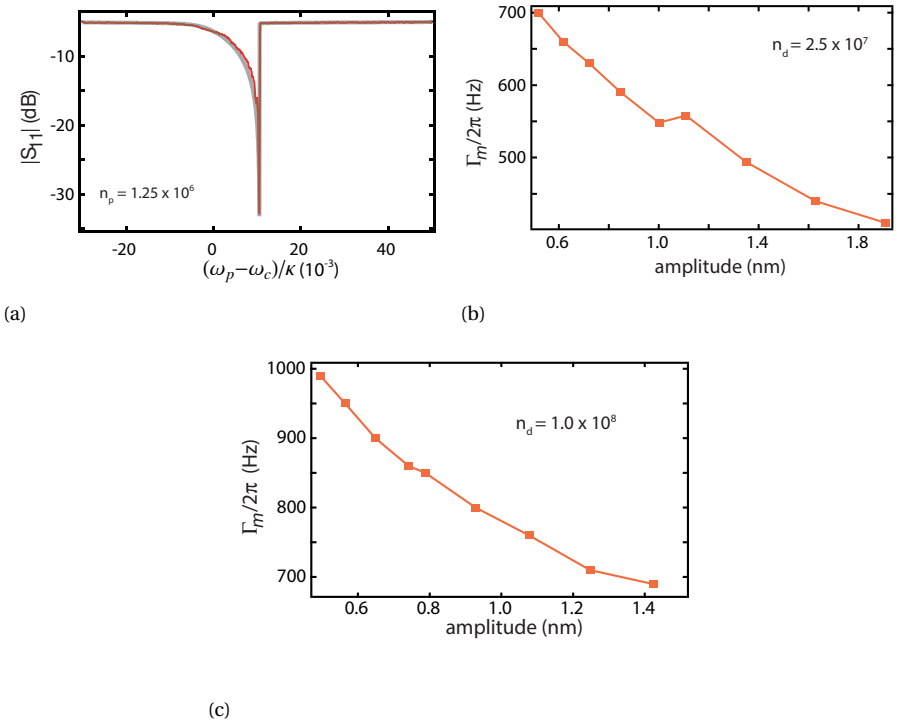

Figure 6.3: (a) Measurement of $|S_{11}|$ showing strong nonlinear response (red curve) together with numerically fitted curve (gray) for $n_d = = 2.5 \times 10^7$. (b), (c) Extracted linear dissipation rate Γ_m plotted against mechanical amplitude for $n_d = 2.5 \times 10^7$ and for 1.0×10^8, respectively.

quency sweep shown in Fig. 6.2 (c). Although, instabilities in mechanical response are known for blue-sideband driving, we do not expect them to arise from optomechanical interaction as we drive the system at red- sideband. The model with Duffing term in the restoring force still captures the response except these instabilities.

6.3.1. EXTRA INSTABILITIES

The decrease in observed damping rate at higher amplitudes suggests possible presence of nonlinear damping terms with negative coefficients (such as $\rho|x|\dot{x}$, $\mu\ x^2\dot{x}$) in the equation of motion of the mechanical resonator. It should be noted that the total damping however remains positive. The fact that the extracted effective driving linear damping shown in Fig. 6.2 does not follow a quadratic dependence on the driving amplitude as expected for a term proportional to $\mu x^2\dot{x}$ implies that a nonlinear damping of the form more similar to $\rho|x|\dot{x}$ applies in this range of driving amplitudes. As this negative nonlinear damping occurs also at low cooperativities, and as it is not seen in the theoretical calculations treating the optomechanical nonlinear response, we do not

believe that it is an optomechanical effect, but instead intrinsic to the mechanical resonator. The amplitude-dependent negative damping could further give rise to the observed instabilities seen in Fig. 6.2(c). There have been also observations of nonlinear damping in nanomechanical resonators [19] and carbon-based resonators [9]. One possible source of negative nonlinear damping is the saturation of two-level systems coupled to the mechanical resonator [20, 21]. At low drive powers, these two-level systems can absorb energy from the mechanical resonator, increasing the mechanical damping rate. At higher powers, the two-level systems (TLSs) become saturated, and the damping rate goes down. Such a process was suggested as an explanation of power-dependent attenuation losses in glasses [22–24], and also was used to describe power-dependent dielectric losses in superconducting electrical resonators [25]. For such a saturation result in nonlinear damping effects, the level spacing of the TLSs should be larger than the bath temperature. In order for TLSs to describe the negative nonlinear damping observed here, the coupling between the TLSs and the mechanical resonator would have to be nonresonant, mediated by strong higher order processes.

We also note that resonators driven in the bifurcated regime can be very sensitive to environment noise that can induce premature switching from the high- to the low-amplitude branch [26], something not captured by our theoretical model. We note, however, that in the experimental measurements, such switching would make the OMIA dips appear less shallow, and lead to an underestimation of the coefficient of the negative nonlinear damping rate, and therefore the measurements represent a lower bound on the magnitude of the negative nonlinear damping.

6.3.2. FIFTH ORDER NONLINEARITY

In what follows we argue that our observed behavior of negative nonlinear damping can not be explained by including higher order conservative nonlinearities in the equation of motion. By including a fifth order term, the equation of motion can be written as,

$$\ddot{x} + \Gamma'_m \dot{x} + \omega_m^2 x^2 + \alpha' x^3 + \zeta' x^5 = F' \cos(\omega t). \tag{6.1}$$

To solve this equation the same technique can be used as in the chapters 2 and 3 for the forced Duffing oscillator to give the following implicit relation between frequency and mechanical amplitude X:

$$F'^2 = \Gamma_m^2 \omega^2 X^2 + \left(\frac{3}{4}\alpha' X^2 + \frac{5}{8}\zeta' X^4 - (\omega^2 - \omega_m^2)\right)^2 X^2. \tag{6.2}$$

In order to understand the dependence of the amplitude on the force and frequency, the parameters are normalized by the mechanical resonance frequency : $F = F'/m_r\omega_m^2$, $\alpha = \alpha'/\omega_m^2$, $\zeta = \zeta'/\omega_m^2$, and $\Gamma_m = \Gamma'_m/\omega_m$. The numerical solutions of this equation are plotted in Fig. 6.4. For these plots, we have used the linear damping rate $\Gamma_m = 6 \times 10^{-3}$, Duffing parameter $\alpha = 2 \times 10^{-5}$, and fifth order conservative nonlinearity $\zeta = \pm 2.3 \times 10^{-9}$. The results with positive and negative fifth order term are shown in Fig. 6.4(a) and (b), respectively, while the normalized force is set to 0.08, 0.28 and 0.48. The curves in blue are solutions with Duffing term alone and are obtained by setting $\zeta = 0$.

It is clear from these plots that under the higher order conservative nonlinearity the on-resonance responsivity does not change. It only results in the force dependent fre-

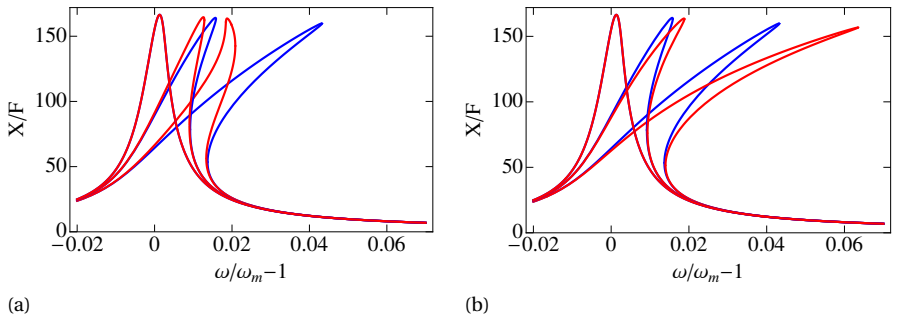

Figure 6.4: Plots of responsivity defined as the ratio of mechanical amplitude to the driving force.(a) Mechanical amplitude including positive fifth order conservative nonlinearity ($\zeta = 2.3 \times 10^{-9}$) in red and excluding fifth order term ($\zeta = 0$) in blue. (b) Mechanical amplitude including negative fifth order conservative nonlinearity ($\zeta = -2.3 \times 10^{-9}$) in red and excluding fifth order term ($\zeta = 0$) in blue. The sequence of curves from left to right denotes amplitude with increasing driving force: $F = 0.08,\ 0.028,\ 0.48$.

quency shift. For small frequency shifts, depth of the optomechanically induced absorption (OMIA) feature depends on the responsivity. Therefore, the observed behavior of the change in the OMIA feature depth can not be explained by including higher order conservative nonlinearity.

6.4. CONCLUSIONS

We examined the nonlinear dynamics of a graphene resonator coupled to a superconducting microwave cavity. In the linear response limit, optomechanically-induced transparency measurements easily allow us to extract the linear damping rate and peak amplitude. At moderate driving force when the response becomes nonlinear, we perform numerical fits by including a Duffing term in the mechanical restoring force and find $\alpha \approx 2.3 \times 10^{15}$ kg m^{-2}s^{-2}. Increasing the driving force further, the OMIA response becomes complex and it is no longer captured by the Duffing term. At these large amplitudes, the nonlinearities start becoming relevant and make the mechanical damping rate appear low at larger amplitudes, where we observe the phenomenon of negative nonlinear damping in a mechanical resonator.

REFERENCES

[1] J. S. Bunch, A. M. v. d. Zande, S. S. Verbridge, I. W. Frank, D. M. Tanenbaum, J. M. Parpia, H. G. Craighead, and P. L. McEuen, Science **315** , 490 (2007).

[2] C. Chen, S. Rosenblatt, K. I. Bolotin, W. Kalb, P. Kim, I. Kymissis, H. L. Stormer, T. F. Heinz, and J. Hone, Nat. Nano **4**, 861 (2009).

[3] V. Singh, S. Sengupta, H. S. Solanki, R. Dhall, A. Allain, S. Dhara, P. Pant, and M. M. Deshmukh, Nanotechnology **21**, 165204 (2010).

[4] C. Chen, S. Lee, V. V. Deshpande, G.-H. Lee, M. Lekas, K. Shepard, and J. Hone, Nat. Nanotechnol. **8**, 923 (2013).

[5] V. Singh, S. J. Bosman, B. H. Schneider, Y. M. Blanter, A. Castellanos-Gomez, and G. A. Steele, Nat. Nanotechnol. **9**, 820 (2014).

[6] P. Weber, J. Güttinger, I. Tsioutsios, D. E. Chang, and A. Bachtold, Nano Lett. **14**, 2854 (2014).

[7] X. Song, M. Oksanen, J. Li, P. J. Hakonen, and M. A. Sillanpaa, Phys. Rev. Lett. **113**, 027404 (2014).

[8] R. M. Cole, G. A. Brawley, V. P. Adiga, R. De Alba, J. M. Parpia, B. Ilic, H. G. Craighead, and W. P. Bowen, Phys. Rev. Appl. **3**, 024004 (2015).

[9] A. Eichler, J. Moser, J. Chaste, M. Zdrojek, I. Wilson-Rae, and A. Bachtold, Nat. Nanotechnol. 6, 339 (2011).

[10] X. Song, M. Oksanen, M. A. Sillanpaa, H. G. Craighead, J. M. Parpia, and P. J. Hakonen, Nano Lett. **12**, 198 (2012).

[11] A. Voje, J. M. Kinaret, and A. Isacsson, Phys. Rev. B **85**, 205415 (2012).

[12] X. Zhou, F. Hocke, A. Schliesser, A. Marx, H. Huebl, R. Gross, and T. J. Kippenberg, Nat. Phys. **9**, 179 (2013).

[13] M. Imboden and P. Mohanty, Phys. Rep. **534**, 89 (2014).

[14] J. D. Teufel, T. Donner, M. A. Castellanos-Beltran, J. W. Harlow, and K. W. Lehnert, Nat. Nanotechnol. **4**, 820 (2009).

[15] G. Anetsberger, E. Gavartin, O. Arcizet, Q. P. Unterreithmeier, E. M. Weig, M. L. Gorodetsky, J. P. Kotthaus, and T. J. Kippenberg, Phys. Rev. A **82**, 061804 (2010).

[16] D. J. Wilson, V. Sudhir, N. Piro, R. Schilling, A. Ghadimi, and T. J. Kippenberg, Nature (London) **524**, 325 (2015).

[17] V. Singh, O. Shevchuk, Ya. M. Blanter, and G. A. Steele, Phys. Rev. B **93**, 245407 (2016).

[18] R. Lifshitz and M. C. Cross. *In Reviews of Nonlinear Dynamics and Complexity*, Wiley-VCH Verlag GmbH & Co. KGaA, Weinheim, Germany, (2008), p. 1.

[19] S. Zaitsev, R. Almog, O. Shtempluck, and E. Buks. *In 2005 International Conference on MEMS, NANO, and Smart Systems*, IEEE Computer Society, (2005), p. 387.

[20] G. Zolfagharkhani, A. Gaidarzhy, S.-B. Shim, R. L. Badzey, and P. Mohanty, Phys. Rev. B **72**, 224101 (2005).

[21] F. Hoehne, Y. A. Pashkin, O. Astafiev, L. Faoro, L. B. Ioffe, Y. Nakamura, and J. S. Tsai, Phys. Rev. B **81**, 184112 (2010).

[22] V. Narayanamurthi and R. O. Pohl, Rev. Mod. Phys. **42**, 201 (1970).

[23] P. W. Anderson, B. I. Halperin, and C. M. Varma, Philos. Mag. **25**, 1 (1972).

[24] W. Arnold, S. Hunklinger, S. Stein, and K. Dransfeld, J. Non- Cryst. Solids **14**, 192 (1974).

[25] J. Gao, J. Zmuidzinas, B. A. Mazin, H. G. LeDuc, and P. K. Day, Appl. Phys. Lett. **90**, 102507 (2007).

[26] W. J. Venstra, H. J. R. Westra, and H. S. J. van der Zant, Nat. Commun. **4**, 2624 (2013).

SUMMARY

This thesis presents a study of nonlinear effects in microwave optomechanical systems. The nonlinearity is essential for creation of non-classical states of the cavity or mechanical resonator such as squeezed or cat states. A microwave cavity can be made nonlinear by, for instance, adding Josephson junctions. The mechanical resonator is inherently nonlinear. The radiation pressure interaction between cavity and mechanical resonator is also inherently nonlinear but typically under strong drive of the cavity interaction can be linearized. However, if the optomechanical system is in the strong coupling regime nonlinear quantum effects become observable. These three cases provide the motivation for our studies.

First, we start with analyzes of the classical regime of a dc SQUID with an embedded mechanical resonator. The SQUID is an intrinsically nonlinear cavity due to the presence of Josephson junctions. A driven mechanical resonator can via optomechanical coupling strongly affect the dynamics of the SQUID. In this way SQUID can be used as a detector of the mechanical motion. Also, there is a backaction mechanism when the detector itself affects the properties of the mechanical resonator. In the regime of the equal mechanical and cavity frequencies the displacement detector has bistable or multistable behavior depending on the backaction strength.

In Chapter 3, we perform quantum analysis of the SQUID coupled to the mechanical resonator. In most microwave optomechanical setups the radiation pressure coupling is obtained by capacitively coupling cavity to the mechanical resonator. In our work, the motion of the mechanical resonator is coupled through the Josephson inductance to the cavity. The main goal is to understand how the asymmetry of two Josephson junctions influences the coupling strength of optomechanical interactions and to achieve ultrastrong coupling regime for the radiation pressure. We investigated two regimes of the dispersive frequencies, when the mechanical frequency much smaller than cavity frequency, and when these two frequencies are resonant. In the first regime, the radiation pressure coupling and the cross-Kerr coupling arise. The asymmetry reduces both couplings and shifts the location of the coupling's maximum value as a function of flux. However, by increasing magnetic field the regime of ultrastrong coupling for the radiation pressure can be reached as well as high values of the cross-Kerr coupling. In the second regime, the main coupling is coming from the single-photon beam splitter interaction and only exists at finite asymmetry.

To investigate the effect of the Kerr-type nonlineairity due to Josephson junctions in this system, in Chapter 4, we study the shifts of the cavity frequency and dissipation. Using variational method and self-consistent harmonic approximation we estimate the influence of the optomechanical coupling and Kerr nonlinearity first for the cavity in the dissipationless situation and then for the more general case including dissipation.

The second part of this thesis focuses on the nonlinearity of the mechanical resonator coupled to the optical/microwave cavity. In Chapter 5, we study in details the

nonlinear optomechanical response. We find that for the Duffing mechanical resonator the OMIA dip has no inflection point and shark-fin like shape in contrast to the OMIR peak, which repeats the Duffing response. The detuning of the drive frequency from the red or blue sideband shifts the OMIA dip and makes it asymmetric. We draw the response map to summarize all results of the overcoupled and undercoupled cavity for the red and blue sidebands additionally to the weak and strong drive powers.

We confirm the developed theory by using it to numerically fit the experimental results of a multilayer graphene resonator coupled to a superconducting microwave cavity in Chapter 6. From the fit, we can extract Duffing nonlinearity parameter. The extracted mechanical dissipation rate at higher mechanical amplitudes suggests that the resonator has negative nonlinear damping.

Olga Shevchuk
February 2017

SAMENVATTING

Dit proefschrift presenteert een studie van niet-lineaire effecten in optomechanische microgolfsystemen. De niet-lineariteit is essentieel voor het maken van niet-klassieke toestanden van de holte of de mechanische resonator. Een microgolfholte kan niet-lineair gemaakt worden door bijvoorbeeld het toevoegen van Josephson juncties. De mechanische resonator is intrinsiek niet-lineair. Ook de stralingsdrukinteractie tussen de holte en de mechanische resonator is intrinsiek niet-lineair, maar kan lineair gemaakt worden door sterke aandrijving van de holte-interactie. Als het optomechanische systeem daarentegen in het sterke koppelingsregime is, kunnen niet-lineaire quantumeffecten zichtbaar worden. Deze drie gevallen vormen de motivatie voor onze studies.

Eerst beginnen we met de analyse van het klassieke regime van een dc SQUID met een ingebouwde mechanische resonator. De SQUID is een intrinsieke niet-lineaire holte door de aanwezigheid van Josephson juncties. Een aangedreven mechanische resonator kan, via optomechanische koppeling, de dynamica van de SQUID sterk beïnvloeden. Op deze manier kan de SQUID worden gebruikt als een detector van de mechanische beweging. Bovendien is er een terugkoppelingsmechanisme als de detector zelf de eigenschappen van de mechanische resonator beïnvloedt. In het regime van gelijke mechanische- en holtefrequencies vertoont de verplaatsingsdetector bi-stabiel of multistabiel gedrag, afhankelijk van de terugkoppelingssterkte.

In Hoofdstuk 3 voeren we een quantumanalyse uit op de SQUID gekoppeld aan de mechanische resonator. In de meeste optomechanische microgolfopstellingen wordt de stralingsdrukkoppeling gevonden door de holte capacitief te koppelen aan de mechanische resonator. In ons werk is de beweging van de mechanische resonator gekoppeld door de Josephson-inductie met de holte. Het hoofddoel is te begrijpen hoe de asymmetrie van de twee Josephson juncties de koppelingssterkte van de optomechanische interacties beïnvloedt, en het bereiken van het ultrasterke koppelingsregime voor de stralingsdruk. We onderzochten twee regimes van de dispersieve frequenties: wanneer de mechanische frequentie veel kleiner is dan de holtefrequentie, en wanneer deze twee frequenties in resonantie zijn. In het eerste regime ontstaan de stralingsdrukkoppeling en de kruis-Kerrkoppeling. De asymmetrie vermindert beide koppelingen en verschuift de locatie van de maximale waarde van de koppeling als een functie van de flux. Het regime van ultrasterke koppeling voor de stralingsdruk en grote waarden van de kruis-Kerrkoppeling kunnen echter ook bereikt worden door het magnetisch veld te verhogen. In het tweede regime ontstaat de hoofdkoppeling door de enkelfotonstraalsplitterinteractie en bestaat alleen voor eindige asymmetrie.

Om het effect te onderzoeken van de Kerr-type niet-lineariteit veroorzaakt door de Josephson juncties in dit systeem bestuderen we in Hoofdstuk 4 de verschuivingen van de holtefrequency en de dissipatie. Gebruikmakend van de variatonele methode en de zelf-consistente harmonische benadering schatten we eerst de invloed van de optomechanische koppeling en de Kerr niet-lineariteit voor de holte in de dissipatieloze situatie

en daarna voor het meer algemene geval waarbij dissipatie wordt inbegrepen.

Het tweede deel van dit proefschrift focust op de niet-lineariteit van de mechanische resonator gekoppeld aan de optische/microgolfholte. In Hoofdstuk 5 bestuderen we in detail de niet-lineaire optomechanische respons. Hier vinden we dat voor de Duffing mechanische resonator het OMIA-dal geen buigpunt heeft en een haaienvinachtige vorm, in tegenstelling tot de OMIR-piek die de Duffingrespons herhaalt. Het wegschuiven van de aandrijffrequentie van de rode of blauwe zijband verschuift het OMIA-dal en maakt het asymmetrisch. We schetsen een grafiek van de respons om alle resultaten samen te vatten van de overgekoppelde en ondergekoppelde holte voor de rode en blauwe zijbanden in toevoeging tot de zwakke en sterke aandrijfkrachten.

We bevestigen de ontwikkelde theorie door het te gebruiken om experimentele resultaten van een multilaags grafeenresonator gekoppeld aan een supergeleidende microgolfholte numeriek te fitten in Hoofdstuk 6. Uit deze fit kunnen we de Duffing niet-lineariteitsparameter afleiden. De afgeleide mechanische dissipatieverhouding voor grotere mechanische amplitudes suggereert dat de resonator een negatieve niet-lineaire demping heeft.

Olga Shevchuk
Februari 2017

CURRICULUM VITÆ

Olga SHEVCHUK

23-07-1989	Born in Kiev, Ukraine.

EDUCATION

2003–2006	Kiev High School of Natural Sciences №145 Ukraine
2006–2010	Bachelor of Science in Electrophysics National Chiao Tung University, Taiwan
2010–2012	Master of Science in Theoretical Physics University of Amsterdam, the Netherlands *Supervisor:* Prof. dr. J. S. Caux
2012–2016	Ph.D. research Delft University of Technology, the Netherlands *Promotor:* Prof. dr. Ya. M. Blanter

LIST OF PUBLICATIONS

5. O. Shevchuk, R. Fazio and Ya. M. Blanter, *Nonlinear analysis of the SQUID based electromechanical cavity*, in preparation.

4. O. Shevchuk, G. A. Steele, and Ya. M. Blanter, *Strong and tunable couplings in flux-mediated optomechanics*, submitted to Phys. Rev. B.

3. V. Singh, O. Shevchuk, Ya. M. Blanter, and G. A. Steele, *Negative nonlinear damping of a graphene mechanical resonator*, Phys. Rev. B **93**, 245407 (2016).

2. O. Shevchuk, V. Singh, G. A. Steele, and Ya. M. Blanter, *Optomechanical response of a nonlinear mechanical resonator*, Phys. Rev. B **92**, 195415 (2015).

1. O. Shevchuk, R. Fazio and Ya. M. Blanter, *Multistability of a Josephson parametric amplifier coupled to a mechanical resonator*, Phys. Rev. B **90**, 205411 (2014).